DEVELOPMENT OF A COMPREHENSIVE ENERGY MODEL TO SIMULATE THE ENERGY EFFICIENCY OF A BATTERY ELECTRIC VEHICLE TO ALLOW FOR PROTOTYPE DESIGN OPTIMISATION AND VALIDATION

Matthew Allan Ray Woods

Submitted in fulfilment of the academic requirements of

Master of Science in Mechanical Engineering.

December 2017

Supervisor: Dr Clinton Bemont

Co-supervisors: Dr Michael Brooks and Mr Jean Pitot

PREFACE

The research contained herein was completed by the candidate while based in the Discipline of Mechanical Engineering of the College of Agriculture, Engineering and Science at the University of KwaZulu-Natal, Howard College Campus, South Africa.

The contents of this work have not been submitted in any form to another university and, except where the work of others is acknowledged in the text, the results reported are due to investigations by the candidate.

DECLARATION - PLAGIARISM

I, Matthew Allan Ray Woods, declare that:

1. The research reported in this dissertation, except where otherwise indicated, is my original research.
2. This dissertation has not been submitted for any degree or examination at any other university.
3. This thesis does not contain other persons' data, pictures, graphs or other information, unless specifically acknowledged as being sourced from other persons.
4. This dissertation does not contain other persons' writing, unless specifically acknowledged as being sourced from other researchers. Where other written sources have been quoted, then:
    a) Their words have been re-written but the general information attributed to them has been referenced.
    b) Where their exact words have been used, then their writing has been placed in italics and inside quotation marks, and referenced.
5. This dissertation does not contain text, graphics or tables copied and pasted from the Internet, unless specifically acknowledged, and the source being detailed in the dissertation and in the References sections.

Signed _____ Date _____

Matthew Allan Ray Woods

ACKNOWLEDGEMENTS

I would like to first and foremost express my heartfelt gratitude to my supervisor, Dr Clinton Bemont and to my co-supervisors Dr Michael Brooks and Mr Jean Pitot for their continued support, guidance and wisdom throughout my research.

I would also like to thank all those who have assisted me with obtaining parameters of the various components used in the Mamba EV, including Mark Gelbien of Enertrac, Fany Chen of Kelly Controls and Axel Dittes for communicating with Continental AG in German on my behalf.

Thank you to my family, Michael, Lynette and David for their endless support and love and especially to my parents for providing me with the opportunity to study. Last, but by no means least, to Amber, for her patience, understanding and relentless support throughout the journey.

The financial assistance of the National Research Foundation (NRF) towards this research is hereby acknowledged. Opinions expressed and conclusions arrived at, are those of the author and are not necessarily to be attributed to the NRF.

ABSTRACT

This dissertation describes the development of an energy model of a battery electric vehicle (BEV) to assist designers in evaluating the impact of overall energy efficiency on vehicle performance. Energy efficiency is a crucial metric for BEVs as it defines the driving range of the vehicle and optimises the limited amount of energy available from the on-board battery pack, typically the most expensive component of the vehicle. Energy modelling also provides other useful information to the designer, such as the range of the vehicle according to legislative drive cycles and the maximum torque required from the motor. An accurate, fast and efficient model is therefore required to simulate BEVs in the early stages of design and for prototype validation.

An extensive investigation into BEV modelling and the mechanisms of energy losses within BEVs was conducted. Existing literature was studied to characterise the effect of operating conditions on the efficiency of each mechanism, as well as investigating existing modelling techniques used to simulate each energy loss. A complete vehicle model was built by considering multiple domain modelling methods and the flow of energy between components in both mechanical and electrical domains.

Simscape™, a MathWorks MATLAB™ tool, was used to build a physics based, forward facing model comprising a combination of custom coded blocks representing the flow of energy from the battery pack to the wheels. The acceleration and speed response of the vehicle was determined over a selected drive cycle, based on vehicle parameters. The model is applicable to normal driving conditions where the power of the motor does not exceed its continuous rating. The model relies on datasheet or non-proprietary parameters. These parameters can be changed depending on the architecture of the BEV and the exact components used, providing model flexibility.

The primary model input is a drive cycle and the primary model output is range as well as the dynamic response of other metrics such as battery voltage and motor torque. The energy loss mechanisms are then assessed qualitatively and quantitatively to allow vehicle designers to determine effective strategies to increase the overall energy efficiency of the vehicle.

The Mamba BEV, a small, high-power, commercially viable electric vehicle with a 21 kWh lithium-ion battery was simulated using the developed model. As the author was involved in the design and development of the vehicle, required vehicle parameters were easily obtained from manufacturers. The range of the vehicle was determined using the World-Harmonised Light Duty Vehicles Test Procedure and provided an estimated range of 285.3 km for the standard cycle and 420.8 km for the city cycle.

TABLE OF CONTENTS

NOMENCLATURE

Abbreviations:

ABS	Antilock Braking System
AC	Alternating current
BEMF	Back electromotive force
BEV	Battery electric vehicle
BLDC	Brushless DC motor
CAD	Computer aided design
CFD	Computational fluid dynamics
COG	Centre of gravity
CVJ	Continuous velocity joint
DAE	Differential algebraic equations
DC	Direct current
DC/DC	DC to DC converter
EIS	Electrochemical impedance spectroscopy
EPA	Environmental Protection Agency
EV	Electric Vehicle
FTP	Federal Test Procedure
GHG	Greenhouse gas
HIL	Hardware in the loop
HWFET	Highway Fuel Economy Test
IC	Internal combustion
ICM	Induction machine
IGBT	Insulated-gate bipolar transistor

IPM	Interior PMSM
ISO	International Standards Organisation
Li-ion	Lithium-ion
MERF	Mean equivalent rolling resistance force
MOSFET	Metal-oxide-semiconductor field effect transistor
MTPA	Maximum torque per ampere
NEDC	New European Drive Cycle
OCV	Open circuit voltage
ODE	Ordinary differential equation
PC	Physical conserving
PI	Proportional-integral
PID	Proportional-integral-derivative
PMSM	Permanent magnet synchronous machine
PS	Physical signal
PWM	Pulse width modulation
RC	Resistor-capacitor
SAE	Society of Automotive Engineers
SOC	State of charge
SOH	State of health
SPM	Surface PMSM
SRM	Switched reluctance machine
SVPWM	Space vector PWM
TCS	Traction Control System
UDDS	Urban Dynamometer Driving Schedule
WLTP	World-Harmonised Light Duty Vehicles Test Procedure

Symbols:

a_0, a_1, a_2, a_3	OCV versus SOC equation coefficients
A_f	Frontal area of the EV
B	Peak flux density
B_m	Viscous friction coefficient
$\boldsymbol{c}$	Initial value matrix
$C_{Capacity}$	Nominal capacity capacitance
C_d	Aerodynamic drag coefficient
C_{eq}	Equivalent capacitance
C_N	Nominal battery capacity
$C_{N_{eq}}$	Equivalent nominal battery capacity
C_p	Peukert capacity
C_{RR}	Coefficient of rolling resistance
$C_{Trans,S}, C_{Trans,L}$	Short and long-time effect capacitance
CSA_{batt}, CSA_{motor}	Battery and motor cable cross sectional area
$E_{sw,r}$	Rated switching loss energy
f	Horizontal distance between front wheel and the COG
$f_1\,(cycle), f_2(temp)$	Cycle and temperature correction factors
$f_3\,(current)$	Discharge rate correction factor
f_m	Motor frequency
F_{ad}, F_{rr}, F_{hc}	Aerodynamic drag, rolling resistance and hill climbing forces
F_d, F_{te}	Driving and tractive forces
F_R	Tyre friction force
F_z	Tyre load
F_{zf}, F_{zr}	Normal forces on the front and rear wheels

g	Acceleration due to gravity
$G_{total}, G_{gb}, G_{df}$	Total, gearbox and differential gear ratios
h	Vertical distance from the road to the COG
i_d, i_q	Stator current in the *dq* reference frame
i_{drain}	Drain current
i_{Drms}	RMS value of the semiconductor on-state current
I_{Batt}	Battery current
I_{Max}	Maximum continuous motor controller current
$J_{gb}, J_{df}, J_{as}, J_{wh}$	Gearbox, differential, axle shaft and wheel rotational inertia
J_m	Rotor rotational inertia
J_{total}	Total rotational inertia
k	Peukert coefficient
$k_{eddy}, k_{hyst}, k_{ex}$	Eddy current, hysteresis and excess loss coefficients
k_p, k_i, k_d	MTPA controller PI constants
K_p, K_i, K_d	Driver model PID constants
K_t, K_v	Torque and velocity constants
K_u	Ultimate gain
L_{batt}, L_{motor}	Total battery cable length and motor phase cable length
L_d, L_q	*dq* axes inductances
L_u, L_v, L_w	*uvw* axes inductances
$L_{line(uvw)}$	Line inductance in the uvw reference frame
LT	Battery runtime
m	Vehicle mass
m_{as}	Axle shaft mass
N	Number of pole pairs

N_P	Number of cells connected in parallel per module
N_S	Number of modules in series
OCV_{eq}	Equivalent OCV voltage
P	Tyre inflation pressure
P_{con}	Conduction power losses
P_{Core}	Core power losses
P_{LV}, P_{HV}	Low and high voltage auxiliary loads
P_{sw}	Switching power losses
r	Horizontal distance between rear wheel and the COG
R	Resistance of the conductor
R_{as}	Axle shaft radius
R_c	Core losses resistance
R_{on}	Drain-source on state resistance
R_{eq}	Equivalent resistance
R_s	Stator resistance
$R_{Self-discharge}$	Self-discharge resistance
R_{Series}	Instantaneous voltage drop resistance
$R_{Trans,S}, R_{Trans,L}$	Short and long-time effect resistance
R_{wh}	Effective radius of driven wheels
s	Dynamic voltage response asymptote
SOC	State of charge
SOC_{regen}	Maximum SOC at which regenerative braking is permitted
t	Time
t_{con}	Transistor conduction time
t_L, t_S	Long and short-time effect tangent lines

T_b	Mechanical braking torque
$T_{cl}, T_{gb}, T_{df}, T_{as}, T_{wh}$	Clutch, gearbox, differential, axle shaft and wheel output torque
T_{em}	Electromagnetic torque produced by the motor
$T_{g,max}$	Maximum generator torque
T_m	Motor output torque
T_p	Switching duration
$T_{m,max}$	Maximum motor torque
T_u	Oscillation period
$u_{q,}u_d$	Stator voltage in the *dq* reference frame
v_{wind}	Wind velocity
v_x	Linear vehicle velocity
V_{Batt}	Battery voltage
V_{min}	End-of-discharge voltage
$V_{min_{eq}}$	Equivalent end-of-discharge voltage
V_L, V_S	Long and short-time effect voltage drop
V_{OC}	Open circuit voltage
$V_{phase,max}$	Maximum motor phase voltage
V_r, I_r	Rated collector voltage and current
V_{SOC}	Voltage across the SOC capacitor
x	Time step duration
$\boldsymbol{y}$	Dependant variable matrix
α, β, a, b, c	SAE J2452 rolling resistance coefficients
ϵ	Angle of inclination or declination of the road
λ	Longitudinal tyre slip
λ_f	Flux linkage due to the rotor magnets

$\lambda_{qs}, \lambda_{ds}$	*dq* axes stator flux linkage components
η_{conv}	DC/DC efficiency
η_{cl} , η_{gb}, η_{df}, η_{as}	Clutch, gearbox, differential and axle shaft efficiencies
η_m	Motor efficiency
η_{total}	Total efficiency
ρ_{air}	Density of air
ρ_{cable}	Cable resistivity
τ	Time instant
τ_L, τ_S	Long and short-time effect time constants
μ	Tyre adhesion coefficient
$\omega_{m,}\omega_{gb,}\omega_{df,}\omega_{wh}$	Motor, gearbox, differential and wheel angular speed
ω_r	Rotor electrical angular speed

LIST OF FIGURES

LIST OF TABLES

CHAPTER 1: INTRODUCTION

1.1 Motivation and context

Electric vehicles (EVs) have only recently become a contender to the internal combustion (IC) vehicles that dominate the automotive sector. EVs were in fact the first powered vehicles available to the public. In the 1830s electric vehicles using non-rechargeable batteries dominated the market until re-chargeable lead acid batteries were developed towards the end of the century (Larminie & Lowry, 2013). By the early 1900's, most privately owned cars, although rare, where in fact electric (Larminie & Lowry, 2013). They were more reliable than their IC counterparts, produced no road-side emissions and started instantly without the need to be hand-cranked. Later, as the price of oil declined and with the invention of the starter motor in 1911, IC vehicles soon began to dominate the market (Larminie & Lowry, 2013).

The main advantage of IC vehicles is that the specific energy of petroleum is far superior to batteries, even taking into consideration the relative inefficiency of an IC engine. IC vehicles can also be refuelled quickly as opposed to batteries which must be charged over longer periods. However, with the commercialisation of lithium-ion (li-ion) batteries with specific energies far greater than lead acid batteries as well as a global drive for reduction in greenhouse gas (GHG) emissions to mitigate the effects of global warming, electric vehicles are again seeing popularisation.

Although EVs produce zero roadside emissions, they can be indirectly responsible for GHG emissions through the generation of electricity used to charge their on-board batteries. However, IC vehicles still produce more CO_2 per kilometre than EVs (even when charged from a coal-dominated grid) and EVs do not produce toxic PM_{10} and NO_2 emissions released from an IC engine (Donateo et al., 2015). Also, it is easier to mitigate harmful emissions and GHGs emitted from a power station on a macro level than it is from a multitude of vehicle engines each operating at different efficiencies (Larminie & Lowry, 2013). EVs offer greater energy efficiency, have the potential to recover braking energy through regenerative braking and most crucially, have the ability to be re-charged from renewable energy sources (Fiori, Ahn, & Rakha, 2016; Juul & Meibom, 2012). They are also cheaper to run, it terms of both re-fuelling and maintenance costs owing to their inherent simplicity.

The global transport sector accounts for 14 % of all GHG emissions (United States Environmental Protection Agency, 2014). The landmark Paris Agreement, effective from 4 November 2016 saw, for the first time since climate change entered onto our radar, a global consensus on reducing our

impact on the environment (UN Framework Convention on Climate Change, 2016). With 196 countries signing the agreement under the auspices of the United Nations Framework Convention on Climate Change, they agreed to decrease their GHG emissions with the aim of keeping global warming to an average temperature which is lower than 1.5°C above pre-industrial levels (UN Framework Convention on Climate Change, 2016). To achieve these goals, an analysis by Global Climate Tracker (2016) revealed that in two decades, 100 % of all new vehicles sold should be electric (Climateactiontracker.org, 2016). Thus the importance of electric vehicle design and development should not be under-estimated.

Modelling and simulation are two of the most important tools for electric vehicle designers. They have many uses for designers from the vehicle concept evaluation stage all the way through to prototype analysis and diagnosing issues of the final production vehicle (Gao, Mi, & Emadi, 2007). EV models allow for numerous design combinations to be tested relatively quickly and with little expense (Gao et al., 2007). This allows designers to make informed decisions to improve the energy efficiency of the vehicle and enhance its safety and dynamic performance by comparing the gain in system performance against the cost of implementing the design (Gao et al., 2007). The designer must then weigh up the simulated benefit of a particular decision against how it will affect the cost of the finished vehicle.

The range of an electric vehicle is a crucial metric in determining the success of the vehicle. Increasing the size of the battery pack, typically the most expensive component of an EV, increases the cost and weight of the vehicle. Therefore it is important for electric vehicle designers to optimise the energy efficiency of the vehicle such that the size of the battery pack can be reduced without reducing the range of the vehicle. However it is also important to assess the cost of energy reduction strategies such that these strategies do not escalate the cost of the vehicle excessively in themselves.

1.2 Mamba EV

TR Tec, in association with the University of KwaZulu-Natal, has developed a small, high performance, two-seater electric vehicle with a true carbon fibre monocoque chassis named the Mamba (Figure 1.1). The vehicle is a prototype that aims to spur interest in EVs in South Africa as well as stimulate local EV manufacture. This work aims to assist in the design and analysis of the vehicle and the Mamba will be used as a means of validating the model presented in this work. Although the model is used to simulate the Mamba's performance, it can also be used to simulate other pure battery electric vehicles with different designs and architectures. The exact specifications of the vehicle are presented later in this work.

Figure 1.1. The Mamba EV.

1.3 Aims and objectives

A complete EV energy model is developed in this work to serve as a tool that can be used by EV designers during the design and evaluation of prototype development. The primary aim of this energy model is to fully characterise and quantify the mechanisms of energy losses within the vehicle and thereby attempt to mitigate these losses through energy reduction strategies and component selection and integration. The effectiveness of these strategies can then also be quantified using the model. The model is also be able to provide the designer with other important metrics such as the range of the vehicle according to standardised drive cycles and the power and energy requirement for the motor and battery pack. The energy model thus developed is intended to be:

1. Simple, accurate and efficient
2. Fast enough to ensure vehicle design can be iteratively optimised
3. Flexible in that various battery electric vehicle (BEV) architectures and combinations of components can be analysed
4. Based on non-proprietary parameters available from manufacturers or from component datasheets

The objectives of the work are:

1. To assess the various mechanisms of energy losses within BEVs and how these losses vary over the full operational envelope of the vehicle under typical driving conditions
2. To assess methods and techniques used for predicting the energy loss in components via readily available input parameters
3. To build a complete and accurate energy model of the vehicle which can be used to computationally simulate the range of the vehicle according to specific vehicle parameters, driving conditions and drive cycles
4. To implement the model using suitable computer software capable of simulating the developed model and maintaining adaptability.
5. To use the complete energy model to analyse the energy losses of the Mamba EV and to characterise these losses over different drive cycles which represent typical driving conditions
6. To predict the range of the Mamba EV according to international electric vehicle testing standards and legislation

1.4 Overview of chapters

This chapter provides the background and motivation for this work as well as outlining its aims and objectives. A literature survey follows in Chapter 2. The survey aims to familiarise the reader with electric vehicle modelling as well as the various energy losses within EVs. Modelling of each sub-system and energy loss mechanism of an EV is analysed. Relevant drive cycles used for range estimation are also explored.

The design and construction of a complete energy model using Simscape™ is detailed in Chapter 3. The parameters required to simulate the Mamba are then presented followed by a brief description of the simulation settings used. In Chapter 4, the results of the Mamba energy simulations are presented. The energy model is used to characterise the energy losses of the vehicle over highway, city and hybrid drive cycles. Chapter 5 discusses the results obtained, the limitations of the work and offers recommendations for future research. The dissertation is concluded in Chapter 6.

CHAPTER 2: LITERATURE SURVEY

2.1 Electric vehicle architecture

Figure 2.1 shows the flow of energy within a BEV while the vehicle is being driven. The battery can be considered as the centre of the system as it provides the energy needed to power the vehicle. Green arrows indicate a flow of energy that acts to charge the battery and red arrows indicate a flow of energy that acts to discharge the battery. Blue arrows indicate a flow of liquid or air used to extract excess heat from a component. The battery powers a brushless motor through the motor controller which converts a direct current (DC) voltage from the battery pack to a three phase alternating current (AC), which causes motor rotation and torque. This torque is transferred to one or more wheels through a mechanical transmission system known as a drivetrain. Power can also flow backwards from the wheels to the battery during regenerative braking when the motor acts as a generator (Larminie & Lowry, 2013).

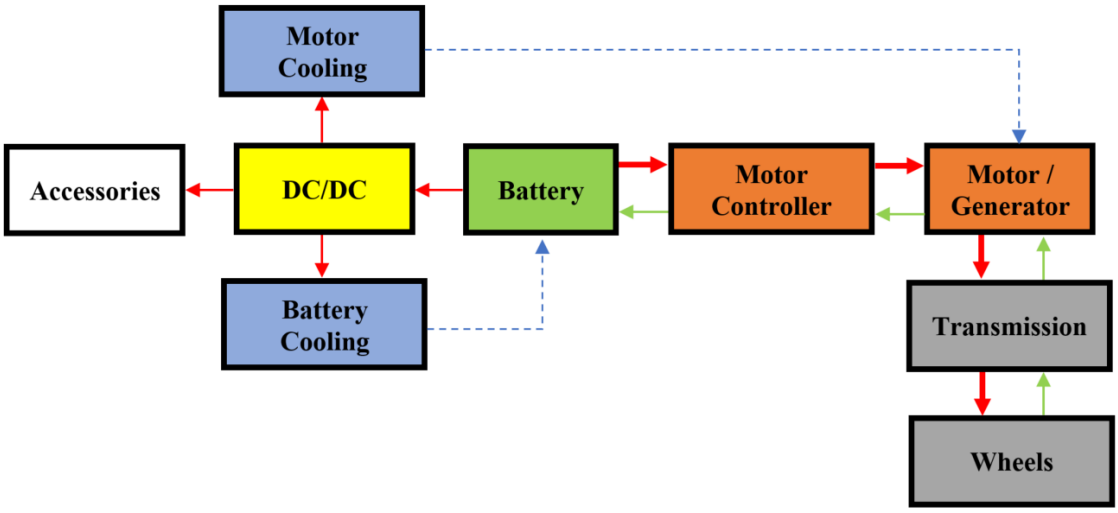

Figure 2.1. Typical BEV architecture showing the flow of energy between components.

The battery also powers a DC to DC convertor (DC/DC) which steps down the high voltage of the battery to a lower voltage (typically 12 V). This lower voltage is used to power auxiliary systems such as the motor cooling system and a battery cooling system to control the temperature of these components. A power supply such as an AC grid supply and an AC to DC converter (charger) is not shown in Figure 2.1 but would result in a charging current directed into the battery while the vehicle is stationary.

Multiple EV architectures, other than the BEV architecture shown in Figure 2.1 exist, such as hybrid electric vehicles, plug in hybrid electric vehicles and range extended battery electric

vehicles. Hybrid electric vehicles use a small battery pack to power an electric motor to drive the vehicle at low speeds where an IC engine is inefficient. The electric drivetrain can also be used to realise regenerative breaking which further increases vehicle efficiency. The plug in version has a larger battery pack that is charged through AC mains. A range extended EV has the same architecture as the BEV with the addition of a small IC engine coupled to a generator to charge the battery pack and extend driving range. This research focuses on BEV architectures and therefore where the general term EV is used, it refers to BEVs.

2.1.1 Drivetrain topologies

The drivetrain of the vehicle can be defined as the group of components that generate power and deliver it to the road (Eriksson & Nielson, 2014). The drivetrain block shown in Figure 2.1 can take on many different architectures to implement front-wheel drive, rear-wheel drive or all-wheel drive using a variety of different drivetrain topologies. Mechanical constituents of the powertrain may include one or more of the following; motors, gearboxes (fixed or variable ratio), differentials, axle shafts, constant velocity joints (CVJs) and wheels (Park, Lee, Jin, & Kwak, 2014).

In the case of front or rear-drive vehicles, six different configurations can be identified, as shown in Figure 2.2 (Park et al., 2014). If one motor is used (Figure 2.2 (a), (b) or (c)), a differential is required such that the wheels can rotate at different speeds when cornering (Park et al., 2014). If one motor is used with a fixed gear ratio, it can be rear mounted, as shown in Figure 2.2 (b), or front mounted, as shown in Figure 2.2 (c). Figure 2.2 (a) resembles the drivetrain of most conventional IC engine vehicles (Park et al., 2014).

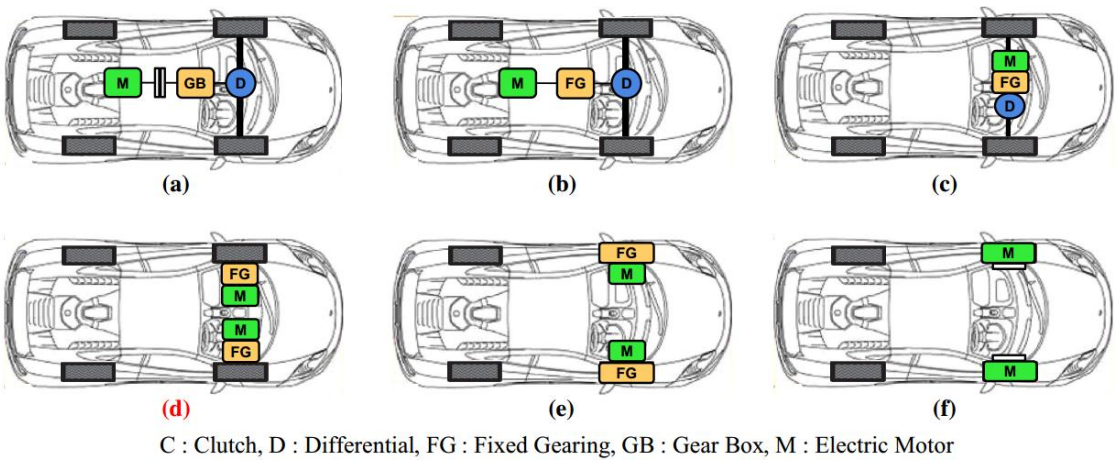

Figure 2.2. Front-wheel drive EV configurations (a) Conventional (b) No transmission, rear mounted motor (c) No transmission, front mounted motor (d) No differntial (e) In-wheel drive with FG (f) In-wheel without FG (Park et al., 2014).

Many different types of gearboxes are available which are classified into two broad categories, either fixed ratio or variable ratio. If a variable gearbox is used without an automatic transmission, a clutch is required to disengage the drive to change gears. Configurations employing one motor are sometimes preferred as they can be used with components readily available for the IC engine market, however in the case of EVs, the drivetrain can be greatly simplified by using two motors which are either centrally mounted or in-wheel mounted using hub motors (Park et al., 2014). The use of two motors eliminates the need for a differential as motor speed can be independently controlled (Park et al., 2014).

In some cases, an electric motor can be used with no gearbox if the top speed of the motor is greater than the desired top speed of the vehicle and if the torque output of the motor is sufficient for vehicle traction and gradeability. The elimination of a gearbox can greatly simplify the drivetrain and consequently increase its efficiency.

All configurations shown in Figure 2.2 can be also be implemented as rear-wheel drive vehicles. All-wheel drive topologies should also be considered, which can use any combination of the six configurations, although they are typically achieved using four in-wheel hub motors in order to simplify the drivetrain.

2.1.1.1 Constant velocity joints

In all configurations, except where an in-wheel (hub) motor is used (Figure 2.2(e) and (f)), an inboard and outboard CVJ with a half shaft is required for the final connection to the wheel to allow for suspension movements, steering movements (in the case of front wheel drive vehicles) and alignment offsets (Hildebrandt, Horst, & Rickell, 2006). Most modern vehicles achieve this with the use of two Rzeppa joints that use balls and tracks to allow for the transmission of torque up to angles of 50° (Hildebrandt et al., 2006). Energy losses in these joins are a result of contact friction between the tracks and balls, and depend on the angle of the joint (Fujio, 2013). Fujio (2013) reported a linear increase in energy loss rate from approximately 0.25 % at a joint angle of 4° to 1.25 % for a joint angle of 12° for standard Rzeppa joints.

2.2 Energy modelling and simulation of EVs

It can be seen from Figure 2.1 that to model and simulate the flow of energy in an EV requires the characterisation of both electrical and mechanical components and the flow of energy between them. Each component has an associated efficiency which refers to the amount of energy that is lost in transferring or converting an energy input to an energy output. This efficiency varies on a large number of variables which change constantly as the vehicle's operating conditions change.

Before considering how to simulate and model an EV, it is important to consider the primary motive for developing the model. Models developed in literature can be used for various purposes such as (Gao et al., 2007):

1. Analysing the vibration, handling and noise response of the vehicle
2. Predicting, evaluating and optimising vehicle fuel economy or energy efficiency
3. Analysing the safety, stability and crash worthiness of the vehicle
4. Modelling vehicle controls
5. Analysing structural integrity of the chassis
6. Component testing and validation
7. Preliminary concept design and evaluation

An energy model with the primary aim of predicting, evaluating and optimising energy efficiency will be discussed in this work.

2.2.1 Definitions

A system can be defined as an object or group of objects of interest, for example an EV (Gao et al., 2007). A model is a surrogate for a real system which can be used to conduct "experiments" of interest and these experiments are called simulations (Gao et al., 2007). Because a particular model has a limited number of simulations which can be carried out on it, more than one model may be required for a single system (Gao et al., 2007). Models require a simulator or tool capable of preforming the simulation typically a computer program capable of solving ordinary differential equations (ODEs), such as MATLAB™ (Gao et al., 2007).

2.2.2 Model fidelity and computation time

Modelling is often a trade-off between the accuracy of the model, known as fidelity and the time required to simulate the system, known as computation time or complexity. It is important to assess the importance of each of these metrics depending on the uses and aims of a particular model. For example, in models used for efficient routing prediction that rely on running multiple iterations over a short space of time to compare energy consumption, fidelity is not critical, but computation time is (Genikomsakis & Mitrentsis, 2017; Fiori et al., 2016).

2.2.3 Modelling approaches

Models can fall into one of three categories; the model can be steady sate, quasi-steady or dynamic (Guzzella & Sciarretta, 2013). Steady-state models employ an average operating point approach, where the variation in vehicle energy efficiency is captured as single average value (Guzzella & Sciarretta, 2013). Such an approach is considered a high level model which does not contain

separate component models (Gao et al., 2007). This approach also requires that the mean mechanical energy consumed per distance travelled for the chosen drive cycle is known (Guzzella & Sciarretta, 2013). The energy used per distance travelled can then be calculated to yield an approximation of the vehicle's range (Guzzella & Sciarretta, 2013).

In order to improve the accuracy of the solution, a model which implements sub-second transient simulations might be employed (Gao et al., 2007). Such models can use a quasi-steady or a dynamic modelling approach. The quasi-steady approach is similar to the average operating point approach, except the time domain is discretised into time steps and the drivetrain efficiency and mechanical energy required is computed at each time step (Guzzella & Sciarretta, 2013). The efficiency of drivetrain components is simulated by interpolating data in look-up tables or maps that contain empirical data of efficiency across the operational envelope of the component (Gao et al., 2007). The vehicle is assumed to run for a short time period at this constant speed, acceleration and gradient and the energy losses are calculated for the short time period based on efficiency at the given operating conditions (Guzzella & Sciarretta, 2013).

The second transient approach, dynamic modelling, describes the system as a set of differential equations based on the physical principals governing the conversion of energy within each component (Gao et al., 2007). This approach is known as a physical modelling approach as it respects the physical causality of the system and therefore the inputs and outputs of the system are the same as those present in the real system (Guzzella & Sciarretta, 2013). The full system is represented as a set of ODEs which can be represented in a state space form (Guzzella & Sciarretta, 2013). Dynamic models require computational tools which implement numerical integration in order to solve the set of equations.

Steady-state modelling offers a simple approach to modelling the efficiency of EVs and simulation can be carried out quickly, however this approach offers the lowest model fidelity. This approach is therefore particularly well suited to preliminary estimations however it does not offer the potential to optimise the energy consumption of EVs through the assessment energy management strategies (Guzzella & Sciarretta, 2013).

Quasi-steady models can be used to optimise the energy efficiency of EVs however they may not capture losses that occur at higher frequencies (Guzzella & Sciarretta, 2013). They offer higher fidelity than steady-state models however computation time is increased. As the time period is reduced, model fidelity is increased at the expense of computation time. A constant or time varying time period may be used, for example a longer time period may be used during periods of idling or slow speeds (Guzzella & Sciarretta, 2013).

Whilst dynamic models have the highest model fidelity, they have slower execution times than steady and quasi-steady models which run more quickly but are less accurate (Fiori et al., 2016). They are capable of capturing losses at all time frequencies, although most of the effects related to energy efficiency change relatively slowly with time (Guzzella & Sciarretta, 2013).

2.2.4 Direction of calculation

Transient models can be simulated using three different approaches to the direction of calculation; forward looking modelling, backward facing modelling or a combination (Fiori et al., 2016; Gao et al., 2007). Forward looking models begin at the motor and require a driver model to determine the torque requested by the driver from the motor to match a target duty cycle (Gao et al., 2007). A simple driver model can be implemented as a PID control loop where a reference torque is generated using the difference between requested and actual vehicle speed (Eriksson & Nielson, 2014). This torque is then transferred to the wheels where a tractive force is generated and the speed and acceleration of the vehicle can be determined.

A backward facing model begins rather at the wheels, where a required tractive force is calculated which is then translated to a required motor torque (Gao et al., 2007). Backward facing models typically have a speed versus time profile as an input and the tractive effort required to follow this cycle is computed. Hybrid forward-backward models employ a backward model architecture where a torque or current is requested based on a backward calculation and then is compared to the maximum available value, for example to ensure the torque requested does not exceed the maximum possible torque output of the motor.

Forward facing models are preferred for hardware in the loop (HIL) setups or controls development as they better represent the true physical causality of the system, however they have slower simulation times than backward facing models (Gao et al., 2007; Guzzella & Sciarretta, 2013). Backward models have quicker execution times while still accurately capturing vehicle energy consumption (Gao et al., 2007). They can also be implemented easily into simulation environments such as Simulink™ and higher level models (Fiori et al., 2016).

2.2.5 Simulation-based optimisation methods

EV energy models can be used to achieve specific targets, such as vehicle range, by optimising system parameters (Nguyen, Reiter, & Rigo, 2014). Due to the complexity of models, it is often difficult to generate a target function that can be optimised. This has led to the development of iterative computational methods to solve optimisation problems. The simplest method is the parametric method, where all parameters are kept constant except one which is varied in a trial and error approach to assess the effect on a design objective (Nguyen et al., 2014). This approach

is time-consuming and therefore algorithms have been developed to automatically iterate towards an optimum solution by building infinite sequences of progressively better approximations of the solution (Nguyen et al., 2014). Optimisation methods commonly used for EV optimisation are (Gao et al., 2007):

1. Divided RECTangle
2. Simulated annealing
3. Genetic Algorithm
4. Particle Swarm Optimisation

2.3 Modelling tools

Numerical computer tools provide a reliable and efficient approach to building models and running dynamic simulations (Guzzella & Sciarretta, 2013). Various modelling tools are available however the program available to the author was MATLAB™ and therefore an overview of the program is discussed in the subsequent section. MATLAB™ is a numerical computing environment designed by MathWorks which allows for easy manipulation of matrices using a proprietary coding language. A toolbox within MATLAB™, Simscape™ will be used to build the model developed in this work and therefore an overview of this toolbox is also provided, in particular the ability for the user to build custom blocks.

2.3.1 Numerical methods for solving ODEs

Physical systems are typically described by a set ODEs which can be defined as equations containing one or more derivatives of some dependant variable, y with respect to a single independent variable, which in the case of physical systems is time, t (MathWorks™, 2017c). ODE's used to model physical systems are initial value problems in the time domain where time is the independent variable (Houcque, n.d.). A general form of an initial value ODE is given in Equation 2.1 and Equation 2.2 where the initial value is given by c (Lei & Hongzhou, 2012). A system of equations containing ODEs as well as equations containing dependant variables without their derivatives (algebraic equations) falls into a special class of systems known as differential algebraic equations (DAEs) (MathWorks™, 2017c).

$$\boldsymbol{y}' = f(t, \boldsymbol{y}) \qquad \text{Equation 2.1}$$

$$\boldsymbol{y}(0) = \boldsymbol{c} \qquad \text{Equation 2.2}$$

Most first order, initial value problems cannot be solved analytically and therefore an approximate solution must be obtained using numerical methods which can be easily implemented computationally (Houcque, n.d.). The first method introduced to this end was Euler's method, introduced in 1978 (Houcque, n.d.). Three types of Euler's method exist; forward, modified (makes use of the trapezoidal rule) and backward methods (Houcque, n.d.). Euler's method discretizes the differential function into multiple time steps with a duration of x and the value computed at each time step is given by Equation 2.3 and Equation 2.4 (Davis, 1984).

$$y_{n+1} = y_n + x \cdot f(t_n, y_n) \qquad \text{Equation 2.3}$$

where,

$$t_n = t_0 + n \cdot x \qquad \text{Equation 2.4}$$

2.3.2 MATLAB™ ODE solvers

MathWorks™ has an array of solvers and careful selection is required to meet the accuracy, stability and computational efficiency requirements of simulations. These solvers can be split into a variety of categories as shown by the flowchart in Figure 2.3. They can be classified as either continuous or discrete. A continuous solver can solve both continuous and discrete elements however a discrete solver can only solve discrete elements (MathWorks™, 2017b). Therefore a discrete solver should only be used where the system is purely discrete.

MATLAB™ can implement both fixed step and variable step solvers. For fixed step solvers, the time period is specified by the user and does not change throughout the simulation. Variable step solvers are used to decrease computational time by continuously varying the step size throughout the simulation. In regions where the solution changes rapidly, a smaller time step is used and in regions of slow change, a longer time step is used. In order to compute the time step an embedded Runga-Kutta solver is used and the accuracy of the solution is kept within error tolerances set by the user (MathWorks™, 2017b).

The various solvers available within MATLAB™ are shown in Figure 2.3. The number after the "ode" term indicates the order of the solver. A single digit indicates a fixed step solver and two digits indicates a variable step solver. Variable step solvers compute the value of the ODE according to two different RK approaches of different orders. For example ode45 indicates a fourth and fifth order approximation is computed in order to determine the size of the time step.

Variable step, continuous solvers designed to solve stiff systems are also available. A stiff system is a system where the desired solution varies slowly but there are closer solutions that vary rapidly (MathWorks™, 2017b). Implicit solvers are designed specifically to simulate stiff systems and are denoted by an "s" in MATLAB™ solvers, such as the ode23s (MathWorks™, 2017b). Whilst implicit solvers are more accurate and particularly well suited to stiff systems, they are difficult to implement and are computationally expensive (MathWorks™, 2017b). MathWorks suggest trying the ode45 solver first and if this solver does not work, a stiff solver should be tried. If a desired solution is achieved with ode45, lower order solvers such as ode23 can be tested (MathWorks™, 2017b). Higher order solvers are more accurate however they are more complex and therefore computation time is higher (Moler, 2011). Although such models require more work per step, less steps may be required to reach a solution and therefore simulation time can be quicker (Moler, 2011).

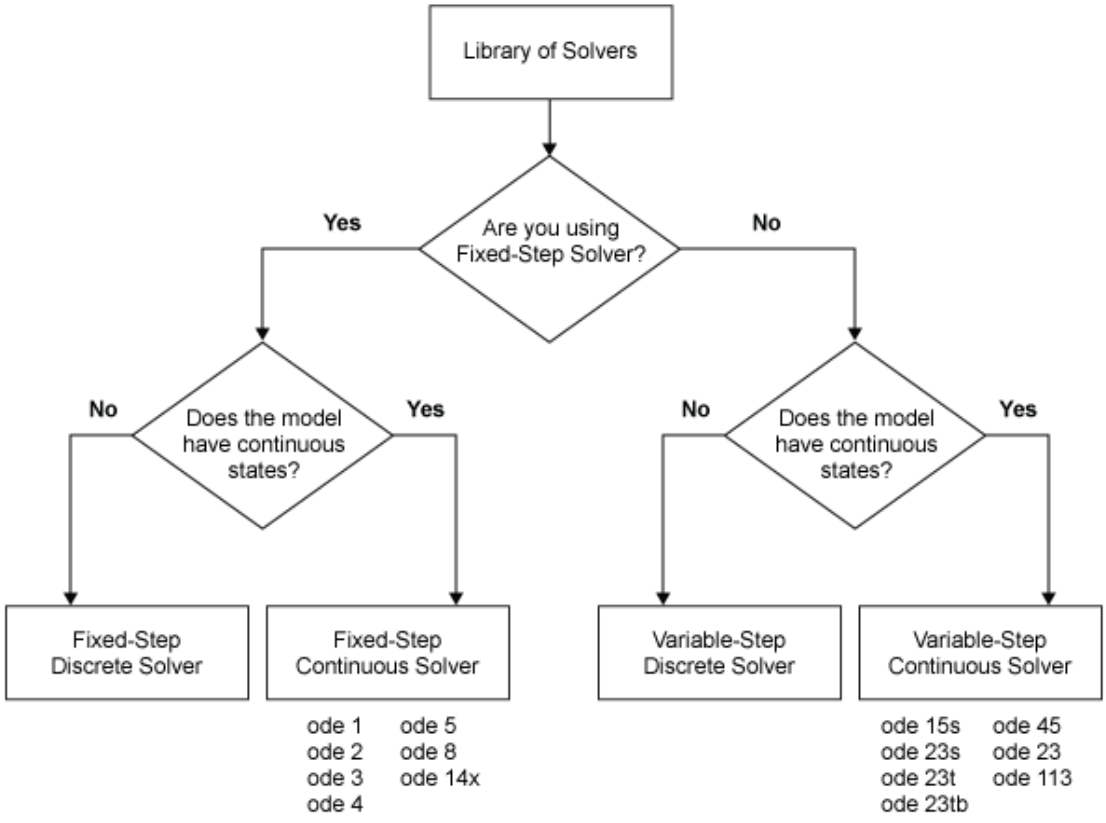

Figure 2.3. MATLAB™ solver selection flowchart (MathWorks™, 2017b).

2.3.3 Simscape™

MATLAB™ has various toolboxes which can be used for specific tasks. One such toolbox is Simulink™ which is a graphical, block based environment that support multi-domain simulations and includes various libraries of common components with the ability for user-defined blocks

(MathWorks, n.d.). Simulink is tightly integrated into the MATLAB™ environment and establishes a set of equations and matrices which can be used to solve dynamic systems. Integration with the MATLAB™ environment allows model variables to be manipulated within the MATLAB™ environment using various toolboxes available within the native MATLAB™ environment.

Table 2.1 shows a comparison of two EV modelling tools built using MATLAB™/Simulink™ which provide a graphical interface as well as a library of component parameters. More detail on each tool appears in Table 2.1. Other vehicle modelling tools also exist such as Virtual Test Bed, FASTSim (an Excel based tool) and Simplorer (Gao et al., 2007).

Table 2.1. Comparison of Autonomie and ADVISOR (Gao et al., 2007).

	Autonomie	**Advanced VehIcle SimultOR (ADVISOR)**
Developer	Argonne National Laboratory.	U.S. National Energy Laboratory.
Open source	No.	Yes.
Types of vehicles	IC, electric, hybrid and fuel cell.	IC, electric, hybrid and fuel cell.
Uses/outputs	Analysis of performance, fuel economy, optimisation routines and HIL.	Analysis of performance, fuel economy and emissions. Linear scaling of components.
Model type	Forward looking.	Backward-forward approach.
Modelling approach	Quasi-steady.	Steady-state.
Flexibility	Yes – look-up table or dynamic model. Models must maintain same number of input and output parameters.	Users may alter each sub-model as long as inputs/outputs kept the same.
Other Notes	Previously called Powertrain System Analysis Toolkit (PSAT) which was phased out in 2010.	Allows links to other software - Saber and Simplorer.

Simulink™ itself also has various toolboxes that offer various benefits over the native Simulink environment. One such example is Simscape™ that allows users to model physical systems by connecting blocks together as they would be connected in a real system. A Simscape™ language

is also available which enables text based authoring of physical components. Simscape™ also allows for more solver settings which are useful in physical simulation and allows for the implementation of HIL testing and real-time simulation. Simscape™ is well suited to multi-domain modelling with ten different domains available as standard as well as the option for user generated domains.

Simscape™ has the following advantages (MathWorks™, 2014):

1. Simscape™ language simplifies the construction of components making use of predefined domains such as the electrical and mechanical domain
2. Components are connected as actual components are connected making the model easy to reconfigure and easier to build on for future iterations
3. Real-time simulation can be implemented which allows for hardware in the loop (HIL) implementation
4. All physical units and conversions are easily handled by the software
5. Physical causality of the system is respected
6. The system is bi-directional which allows for implementation of regenerative braking
7. Custom components can be generated using the Simscape™ language
8. Simscape™ can log all variables throughout the simulation and graphically display all results

Simscape™ employs a physical network approach in order to simplify the construction of the set of ODEs defining a physical system (MathWorks™, 2017a). This simplification is achieved using computational tools to build the model as a set of blocks which represent mathematical models of sub-systems. Sub-systems typically represent a single component of the system, although they may also represent a combination of components or parts of components. Blocks are able to exchange energy with other blocks in the same physical domain through non-directional ports (MathWorks™, 2017a). When blocks are correctly connected together, the resultant model is equivalent to a mathematical model of the complete system (MathWorks™, 2017a). Because the connection between blocks mimics physical connections, blocks are connected as they would be in the physical system (MathWorks™, 2017a).

Energy flow between blocks is characterised by an across and through variable which are unique to each physical domain. Simscape™ considers the transfer of energy using across and through variables, which are unique to each domain (MathWorks, 2017e). The product of through and across variables is usually power (MathWorks, 2017a). Through variables are defined as variables which are measured with a gauge connected in series with an element and across variables with a

gauge connected in parallel (MathWorks, 2017a). In the case of electrical components, the effort (across) variable is voltage and the flow (through) variable is current and for mechanical systems the effort (across) variable is torque and the flow (through) variable is speed (Gao et al., 2007).

2.3.4 Simscape™ solvers

Simscape™ allows for the use of a local solver to simulate physical networks in conjunction with the global Simulink solvers discussed earlier. Local Simscape™ solvers provide solvers best suited to solving physical systems and provide further functionality such as real-time fixed cost simulation and the ability to use different solvers for each physical network (MathWorks™, 2014). Two local solvers are available to simulate physical systems, a backward Euler approach or a trapezoidal rule approach. Although the backward Euler approach is more stable, it can damp oscillations in systems where high frequency oscillation is expected (MathWorks™, 2014).

A local solver also allows the model designer to select between the use of sparse or full linear algebra which refers to the manipulation of the matrices used to implement the numerical modelling approach. Sparse linear algebra is recommended for large systems, with a large number of states, as it increases the efficiency of the simulation (MathWorks™, 2014).

The local solver also allows for a fixed-cost runtime simulation approach, where time step and number of per-step iterations is fixed (MathWorks™, 2014). This enables real-time simulation for HIL testing and comparison of simulation time across different platforms (MathWorks™, 2014). It must be ensured that the local and global solvers are harmonised. If a local fixed-cost solver is selected, a fixed-step global solver is required (MathWorks™, 2014).

2.3.5 Simscape™ language

The Simscape™ language allows users to create new component blocks using a programming language based on the MATLAB™ programming language. The language is adapted to physical modelling to make programming custom blocks easier and more intuitive (MathWorks™, 2017e). Models can be created across various physical domains, which define how energy and data is transmitted. Component blocks are coded as text files and represent the physical component to be modelled (MathWorks™, 2017e). The text file consists of various sections which define the component, as shown in Table 2.2, which also presents a brief description of each section.

Table 2.2. Simscape™ language members (MathWorks™, 2017e).

Section	Description
Parameters	Constants which define the physical components. Appear in the block dialog box.
Nodes	Physical conserving ports associated with a particular domain. Carries through and across variables and writes a conserving equation for through variables. Only nodes of the same domain are connected together.
Inputs and Outputs	Directional physical signal ports carrying physical signals and their associated units.
Variables	Domain or component variables.
Branches	Establish relationship with through variables and nodes. Also establishes the direction of positive flow.
Setup	Executed once at start of simulation. Used for error checking and to set the priority of initial values of variables.
Equations	First equation defines the relationship between component across variables and nodes. Other equations define the relationship between component across and through variables. Uses double equal signs to represent a symmetrical mathematical relationship rather than an assignment.

Simscape™ blocks interact with other blocks in the system through two types of ports, physical conserving (PC) ports and physical signal (PS) ports (MathWorks™, 2017a). PC ports represent actual physical connections. They are non-directional and are connected using physical connection lines which exchange energy between blocks by carrying through and across variables (MathWorks™, 2017a). Physical connection lines can be branched and any lines connected to the same branch point will carry the same across variable but through variables are split among the branches (MathWorks™, 2017a). The vector sum of all through variables at any branch point must always be zero (MathWorks™, 2017a). PS ports are unidirectional ports which carry physical signals which may or may not have units associated to them (MathWorks™, 2017a).

2.4 Vehicle dynamics and motion

In order to drive a vehicle forward, a prime mover (the electric motor in EVs) must apply a torque to the vehicle's wheels through a mechanical drivetrain which may consist of a combination of one or more of the following; a clutch, a gearbox, axles and a differential (Park et al., 2014). This applied torque is then transmitted to the road through the tyre contact patch, generating a force which must overcome external resistive forces acting on the vehicle. It is important to consider the influence of the moment of inertia of rotating parts and the inertia of the vehicle's mass on the dynamics of the vehicle (Park et al., 2014). Figure 2.4 shows a two-wheel based vehicle model with the various forces and moments acting on it as it accelerates up a hill for a front-wheel-drive vehicle.

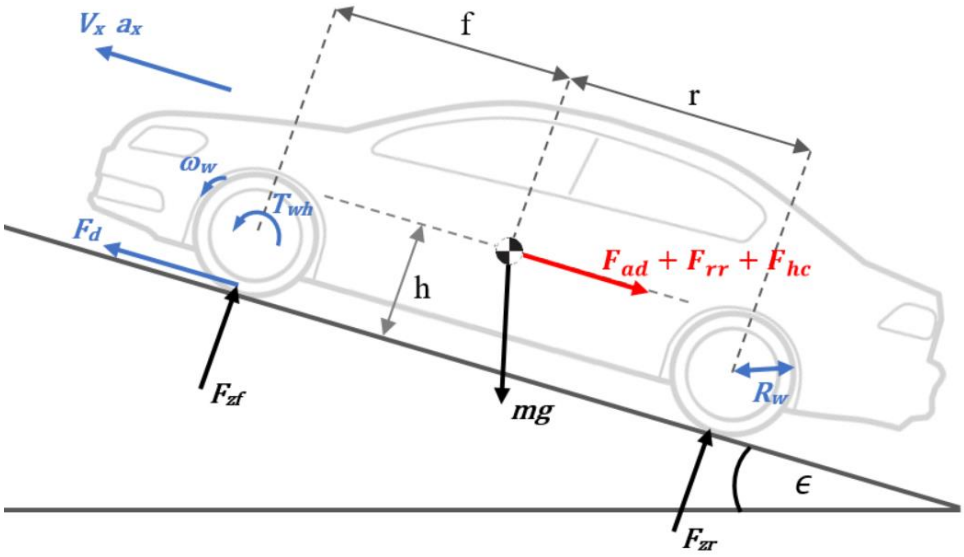

Figure 2.4. Two-wheel based vehicle model.

The first consideration should be the relationship with the torque applied at the wheel, T_{wh} in terms of the torque output of the motor, T_m. It is therefore critical to consider the flow of mechanical power from the motor to the wheels which is summarised in Figure 2.5. The transfer of power from motor to wheels is through rotational energy and therefore the equivalent rotational inertia, J should be considered as well as the energy efficiency, η of each component. The energy efficiency represents energy lost due to damping and friction and can be represented as a constant value (Park et al., 2014). The gearbox and differential have an associated gear ratio, G which increases output torque, T and decreases angular speed, ω.

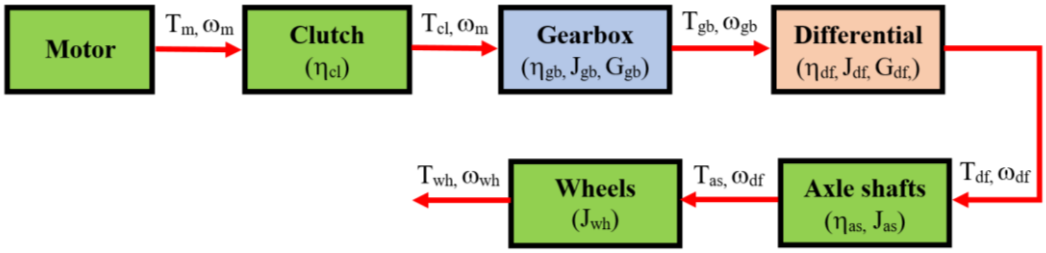

Figure 2.5. Flowchart showing the transmission of mechanical power from motor to wheels.

The torque and power output of each component can be calculated as a function of the torque and angular speed inputs from the previous component, an example is shown for the output torque and speed of the gearbox in Equation 2.5 and Equation 2.6 (Park et al., 2014).

$$T_{gb} = \left(T_{cl} - J_{gb}\frac{\dot{\omega}_m}{G_{gb}}\right) \cdot \eta_{gb} G_{gb} \qquad \text{Equation 2.5}$$

$$\omega_{gb} = \frac{\omega_m}{G_{gb}} \qquad \text{Equation 2.6}$$

By taking a similar approach for each component and substituting the output torque of one component as the input of the subsequent component, Equation 2.7, Equation 2.8, Equation 2.9 and Equation 2.10 can be derived for the entire drivetrain (Park et al., 2014). An additional term, T_b has been included in Equation 2.7 in order to account for the braking torque applied due to the mechanical braking system. An axle shaft efficiency has also been included in Equation 2.9 to consider the efficiency of the CVJs.

$$T_{wh} = G_{total}\eta_{total}T_m - J_{total}\dot{\omega}_m + T_b \qquad \text{Equation 2.7}$$

where,

$$J_{total} = J_{gb}G_{total}\eta_{gb}\eta_{df} + J_{df}\eta_{df} + \frac{J_{as} + J_{wh}}{G_{total}} \qquad \text{Equation 2.8}$$

$$\eta_{total} = \eta_{cl}\eta_{gb}\eta_{df}\eta_{as} \qquad \text{Equation 2.9}$$

$$G_{total} = G_{gb}G_{df} \qquad \text{Equation 2.10}$$

The driving force applied to the road, F_d is therefore given by Equation 2.11.

$$F_d = \frac{T_{wh}}{R_{wh}} \qquad \text{Equation 2.11}$$

In the above, R_{wh} is the effective radius of the driven wheels.

Newton's second law can then be used to determine the linear acceleration of the vehicle, $\dot{v_x}$ as shown in Equation 2.12 and Equation 2.13.

$$m\dot{v_x} = F_d - F_{te} \qquad \text{Equation 2.12}$$

where,

$$F_{te} = F_{ad} + F_{rr} + F_{hc} \qquad \text{Equation 2.13}$$

In the above, m is vehicle mass, F_{te} is the tractive effort required to overcome resistive forces, F_{ad} is the force due to aerodynamic drag, F_{rr} is the force due to rolling resistance and F_{hc} is the hill-climbing force given by Equation 2.14. Resistive forces due to rolling resistance and aerodynamic drag are discussed in greater detail in subsequent subsections.

$$F_{hc} = mg \cdot sin(\epsilon) \qquad \text{Equation 2.14}$$

In the above, g is the gravitational constant and ϵ is the angle of inclination or declination of the road.

The weight of the vehicle acts vertically down through its centre of gravity (COG). By considering the horizontal distance between the front and rear wheels and the COG, f and r respectively and the vertical distance from the road to the COG, h, a sum of moments can be computed about the COG. This gives the normal forces on the front and rear wheels, F_{zf} and F_{zr} respectively and the results are shown in Equation 2.15 and Equation 2.16 (Jazar, 2014).

$$F_{zf} = \frac{mg}{f+r}\left(r \cdot cos(\in) - h \cdot sin(\in)\right) - \frac{ma \cdot h}{f+r} \qquad \text{Equation 2.15}$$

$$F_{zr} = \frac{mg}{f+r}\left(f \cdot cos(\in) + h \cdot sin(\in)\right) + \frac{ma \cdot h}{f+r} \qquad \text{Equation 2.16}$$

2.4.1 Longitudinal tyre dynamics

Acceleration and braking forces applied to a vehicle's wheels must interact with the ground through the tyre contact patch. Vehicle longitudinal forces are imparted to the road through tyre deformation which can cause the rubber parts to partially slide even when the wheel is not locked

(Miller, Youngberg, Millie, Schweizer, & Gerdes, 2001; Reif, 2014). This phenomenon is known as longitudinal tyre slip, λ and is defined by Equation 2.17 (Gao et al., 2007).

$$\lambda = \frac{\omega_{wh} \cdot R_{wh} - v_x}{max\{v_x,\ \omega_{wh} \cdot R_{wh}\}} \qquad \text{Equation 2.17}$$

Under normal driving conditions λ is greater than zero which causes a friction force in the direction of forward motion (Gao et al., 2007). During breaking $\lambda < 0$ which causes a friction force opposite to the direction of forward motion (Gao et al., 2007).

Tyre slip is an important property as literature shows a correlation between the tyre adhesion coefficient, μ and tyre slip (Gao et al., 2007). Tyre adhesion allows the torque applied to driven wheels to impart a force to the road through a friction force, F_R which is related to the adhesion coefficient as shown in Equation 2.18. The relationship between the adhesion coefficient and tyre slip for different road conditions is shown in Figure 2.6. As slip increases, μ increases rapidly to a maximum value representing the maximum friction force.

$$F_R = \mu(\lambda)mg \qquad \text{Equation 2.18}$$

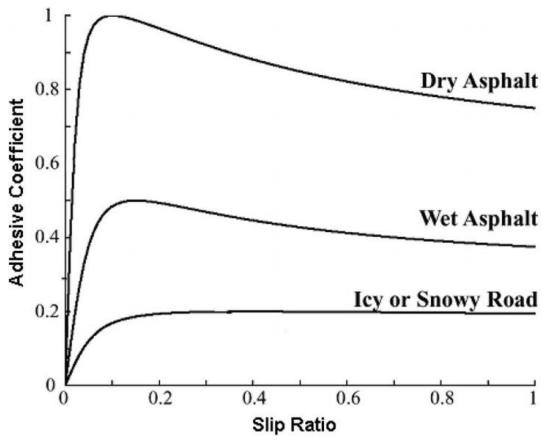

Figure 2.6. Adhesive coefficient versus slip ratio for various road conditions (Gao et al., 2007).

The friction force is a measure of the tyre's ability to transmit a force through the contact patch to the surface it is travelling on (Reif, 2014). It is therefore a critical metric when considering braking and is a critical variable for the implementation of systems such as an Antilock Braking System (ABS) and a Traction Control System (TCS) which maximise vehicle grip (Reif, 2014).

Tyre slip must be considered for dynamic vehicle simulations as the wheel will accelerate faster than the vehicle (Gao et al., 2007). If there is no slip, the linear acceleration of the vehicle can be related to the angular acceleration of the wheel according to Equation 2.19.

$$\dot{v}_x = R_{wh} \frac{\dot{\omega}_m}{G_{total}} \qquad \text{Equation 2.19}$$

However, under slip conditions, Equation 2.19 is no longer valid and Equation 2.17 must be differentiated to solve for the relationship between $\dot{v}_x$ and $\dot{\omega}_m$ which becomes a function of tyre slip (Fujii & Fujimoto, 2007).

2.5 Rolling resistance

Tyres are an important part of any vehicle as they are responsible for a vehicle's traction to the road during driving and steering, its handling characteristics and ride comfort (Michelin, 2003). Tyres are typically constructed from vulcanized, reinforced polymers which are visco-elastic materials. The flexible nature of this type of material is important as it allows the development of a contact patch with the road, as opposed to making contact at a single point which enables the tyre to grip better and absorb asperities in the road surface (Michelin, 2003).

Visco-elastic materials exhibit the property of hysteresis which means that when the material is deformed it takes longer to return to its initial position, as some energy is dissipated as heat (Michelin, 2003). Hysteresis has two important side effects in tyres: rolling resistance and grip (Michelin, 2003). Rolling resistance is defined in the ISO 8767 standard as "energy consumed by a tyre per unit of distance covered" (Evans et al., 2009). This loss in energy means more energy must be applied to the tyre as increased torque, to keep the tyre rotating at the same speed. Rolling resistance losses do not include spindle or bearing losses as these losses are not a result of the tyre (Evans et al., 2009).

Rolling resistance on hard surfaces is caused by three main phenomena; deformation of the tyre as it is deformed in the area of the contact patch, aerodynamic drag and rotational drag and slippage between the tyre and the road or between the tyre and the rim (Michelin, 2003). Deformation of the tyre is the primary cause and accounts for 80 to 95 % of rolling resistance (Michelin, 2003). When a tyre is moving over a surface covered with water or snow additional tyre deflection is induced as the tyre moves or compresses the water or snow (Sandberg, 2011). A car tyre does not make contact with the road at a single point but rather in the area of a contact

patch caused by flattening of the tyre, as shown in Figure 2.7. Therefore the reaction force of the tyre due to the weight of the vehicle acts across this patch.

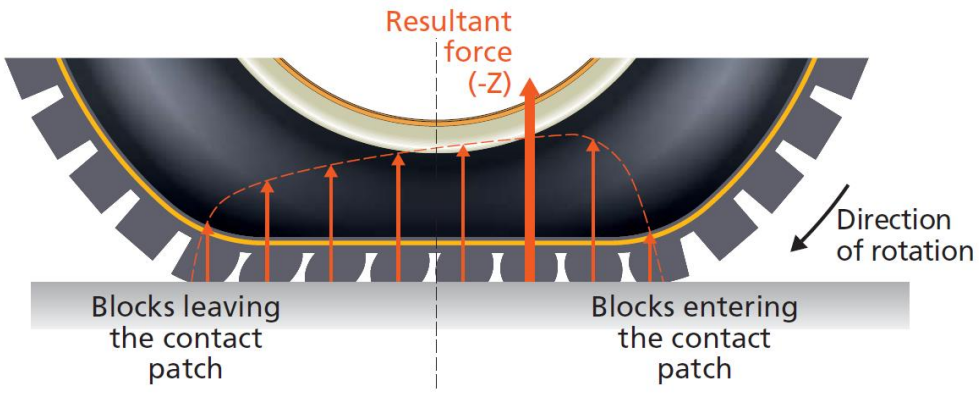

Figure 2.7. Reaction forces at the contact patch (Michelin, 2003).

It has been found that the reaction forces are larger in the front of the tyre as compared to the rear (Michelin, 2003). Hysteresis means that the tyre does not recover in the same time it took to deform which means the reaction forces are smaller toward the rear of the contact patch (Michelin, 2003). The resultant pressure force therefore acts some distance in front of the centreline of the wheel as seen in Figure 2.8. This causes a moment to act about the axle of the wheel which opposes the direction of the torque applied to the wheel to drive it forward (Michelin, 2003).

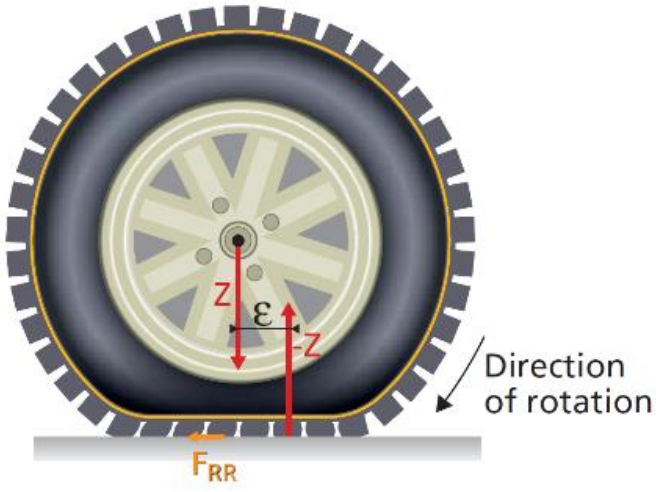

Figure 2.8. Resultant pressure and weight vectors acting on a tyre during rotation (Michelin, 2003).

Following the definition of rolling resistance as energy lost per unit distance, it can be expressed as J/m or N·m/m, as 1 N·m is equivalent to 1 J, or as a force in Newtons. However, Schuring and

Futamura (1990) emphasise that although dimensionally equivalent to a force, rolling resistance is a scalar value and therefore it is not a force but rather an energy lost per distance travelled.

It has been found that there is a very close linear relationship between the load on the tyre and rolling resistance (Evans et al., 2009). Therefore rolling resistance is often expressed in terms of the rolling resistance coefficient, C_{RR} as given in Equation 2.20.

$$F_{rr} = C_{RR} \cdot F_Z \qquad \text{Equation 2.20}$$

The rolling resistance force, F_{rr} and the load on the tyre, F_Z are both expressed in Newtons and the rolling resistance coefficient, C_{RR}, is a dimensionless number. This equation is useful for comparing tyres to be used for the same application and under the same operating conditions such as tyre pressure and speed. This is because rolling resistance is not only dependent on the load on the tyre but also on its operating conditions; speed, temperature, rolling time and inflation pressure (Hall & Moreland, 2001; Michelin, 2003).

2.5.1 Effect of speed

Rolling resistance is typically tested according to International Standard Organisation (ISO) standards at a speed of 80 km/h (Evans et al., 2009). Aerodynamic drag is usually included in rolling resistance tests and because aerodynamic drag increases with the square of speed, the effect of speed will be greater at higher speeds (Hall & Moreland, 2001). Centrifugal forces within the tyre also increase as tyre speed increases and therefore more energy is consumed. Standing waves within the structure of the tyres can also develop at higher speeds which causes rolling resistance to increase exponentially (Hall & Moreland, 2001).

It should be noted that there are also phenomena which act to reduce rolling resistance at higher speeds. At higher speeds the frequency of deformation increases, which reduces rolling resistance as the phase lag of all vulcanised polymers drops with increased frequencies (Hall & Moreland, 2001). Also, as the frequency of deformation increases, so does tyre temperature which lowers rolling resistance. However these effects are not significant enough to counteract the mechanisms acting to increase rolling resistance at higher speeds (Hall & Moreland, 2001). Figure 2.9 shows the values of rolling resistance force versus speed on a 1.2 tonne car with 4 wheels with a C_{RR} of 0.0085. It can be seen that speed has little effect up to 100 to 120 km/h (Michelin, 2003).

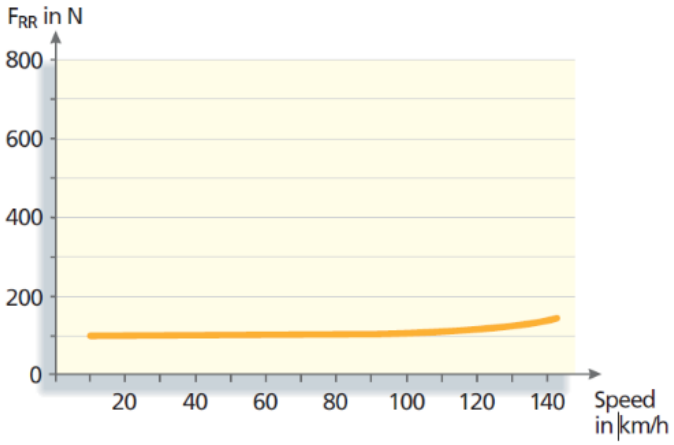

Figure 2.9. Relationship between rolling resistance and vehicle speed (Michelin, 2003).

2.5.2 Effect of temperature

The temperature of a vehicle's tyre does not remain constant throughout its journey. The heat lost from the hysteresis of the tyre deformation causes heat build-up and ultimately a rise in tyre temperature. This causes its rolling resistance force to decrease as the tyre material becomes less visco-elastic at higher temperatures (Janssen & Hall, 1980). The increased temperature will also increase tyre pressure which will in turn decrease the rolling resistance force further. Janssen and Hall (1980) conducted rolling resistance tests at different ambient temperatures and measured the rolling resistance at the start of the test until tyre shoulder temperature reached equilibrium. The results are displayed in Figure 2.10 and show that the final rolling resistance can be significantly lower, especially at lower ambient temperatures.

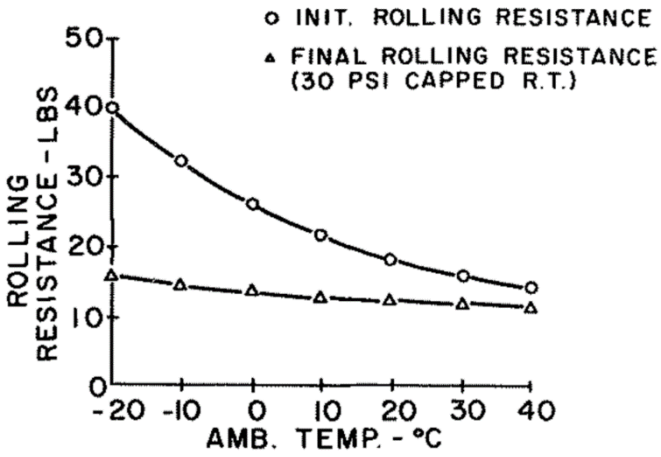

Figure 2.10. Effect of ambient temperature on initial and final rolling resistance (Janssen & Hall, 1980).

Clark and Dodge (1979) report that for passenger car tyres, a temperature equilibrium is reached after 20 to 30 minutes under steady-state conditions such as highway driving. For urban drive cycles however, tyres do not reach an equilibrium point but rather fluctuate around an average temperature (Clark & Dodge, 1979).

2.5.3 Effect of tyre inflation pressure

It can be shown that a decrease in tyre inflation pressure (at 80 km/h, 80 % maximum load and at 25°C) by 1 bar from the ISO standardised 2.1 bar used in rolling resistance tests, causes a 30 % increase in rolling resistance (Michelin, 2003). As inflation pressure decreases, a tyre will deform more which increases tread bending a shear forces (Michelin, 2003).

2.5.4 Effect of tyre load

A very close relationship exists between tyre load and rolling resistance. As load is increased rolling resistance increases due to more bending and shearing in the contact patch (Evans et al., 2009). It has however been shown by other authors that the rolling resistance coefficient decreases as load increases as a result of an increase in tyre temperature as load is increased (Michelin, 2003).

2.5.5 Effect of tyre material

The reinforced vulcanised elastomers used in modern tyres contain over 200 raw materials and are made up of polymers combined with reinforcing fillers and sulphur (Michelin, 2003). The hysteretic energy loss within tyres is only due to the properties of the polymers they are constructed from (Michelin, 2003). Because hysteresis in a tyre leads to both grip and rolling resistance, polymers with low hysteresis cannot be chosen as safety will be compromised (Michelin, 2003). The challenge is for manufactures to decrease rolling resistance without compromising tyre grip.

Although hysteresis leads to grip and rolling resistance, the frequency is different for each mechanism (Michelin, 2003). Michelin (2003) found they could decrease hysteresis in the domain of rolling resistance (lower frequencies) and increase hysteresis in the domain of grip (higher frequencies) by altering the layout of reinforcing aggregates within the tyre.

Reinforcing fillers such as carbon black or silica increase tyre rigidity and decrease tyre wear, thereby extending the life of tyres, however these compounds also amplify energy dissipation, especially carbon black (Michelin, 2003). By using silica and increasing the distance between filler aggregates by ensuring the they are equally spaced, this effect can be reduced (Michelin, 2003). Tyre manufacturers have reduced rolling resistance significantly in recent years as shown

by Figure 2.11, which depicts the rolling resistance index of the lowest tyre produced in a year from 1980 to 2000.

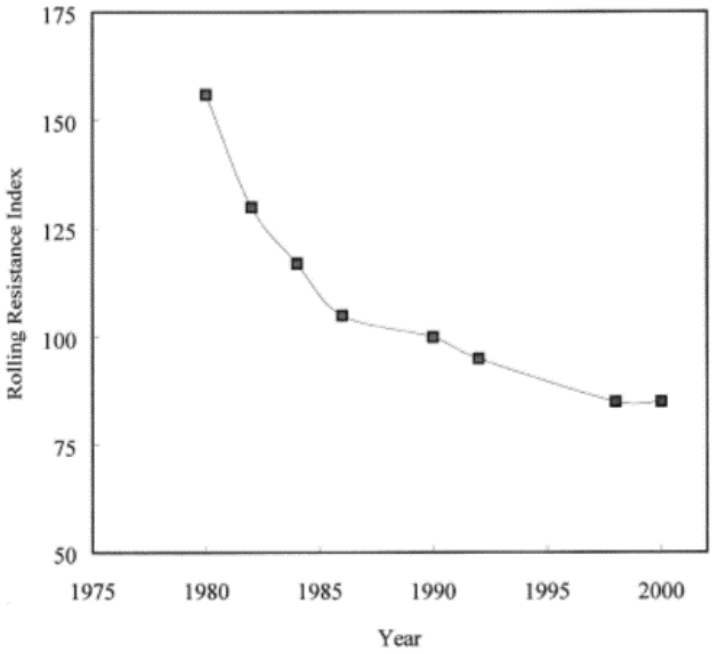

Figure 2.11. Reduction of rolling resistance of Michelin tyres since 1979 (Hall & Moreland, 2001).

2.5.6 Effect of tyre dimensions

Michelin (2003) report that an increase in rim diameter of 10 mm results in approximately 1 % reduction in rolling resistance. The primary cause of rolling resistance is the result of tyre bending in the region of the contact patch and therefore as tyre diameter increases, less deflection is required to create the contact patch as the curvature of the tyre will be less than that of a smaller diameter tyre (Michelin, 2003). A multivariate statistical analysis of 170 tyres, presented in a report by the National Research Council Transportation Research Board (2006), concluded that increasing rim diameter by 1 inch would cause a 5 to 8 % loss in rolling resistance which is on average 2.3 times greater than the loss predicted by Michelin (2003).

2.5.7 Effect of speed category

The analysis of 170 tyres by the National Research Council Transportation Research Board (2006) also found that tyres with a lower speed rating showed a lower rolling resistance coefficient. Tyres with the highest speed ratings (W, Y, Z) were found to have 10 to 22 % higher rolling resistance coefficients as compared to tyres with the smallest speed rating (S, T).

2.5.8 Tyre labelling

Regulation EC 1222/2009 requires that all new tyres sold from 1 November 2012 be labelled with the tyre's noise level, wet skid resistance and fuel efficiency (Sandberg, 2011). The fuel efficiency of the tyre is determined directly from the rolling resistance coefficient measured according to ISO 28580 (Sandberg, 2011). The energy efficiency is reported as an efficiency class which corresponds to a rolling resistance coefficient as shown in Table 2.3.

Table 2.3. EC 1222/2009 energy efficiency classes and corresponding rolling resistance coefficients (Sandberg et al., 2011).

C_{RR} [kg/t]	Energy efficiency class
$C_{RR} \leq 4.0$	A
$4.1 \leq C_{RR} \leq 5.0$	B
$5.1 \leq C_{RR} \leq 6.0$	C
$6.1 \leq C_{RR} \leq 7.0$	D
$7.1 \leq C_{RR} \leq 8.0$	E
$C_{RR} \geq 8.1$	F

2.5.9 Measurement methods

Tyre rolling resistance can be grouped into two main categories; testing of tyres on a laboratory drum or testing of tyres on actual road surfaces. In the drum method, a large drum, typically 1.7 m in diameter, with a smooth or textured surface is rotated by an electric motor (Sandberg, 2011). The tyre to be tested is allowed to spin freely on an axle and is held against the rotating drum with a specific force corresponding to the tyre load. The rolling resistance of the tyre causes a breaking effect on the drum which can be used to quantify rolling resistance by measuring a spindle force or a torque required to maintain constant drum speed and subtracting parasitic losses (Sandberg, 2011). Figure 2.12 is an example of a laboratory drum testing apparatus used at a testing facility in Poland.

Figure 2.12. Rolling resistance testing apparatus used in a Polish testing facility (Sandberg, 2011).

Both the Society of Automotive Engineers (SAE) and ISO have defined standardised laboratory testing methods to measure rolling resistance using drums. The testing standards cover both passenger car and truck tyres however only passenger car tyres will be discussed as truck tyres are not pertinent to the aim of this research.

2.5.10 Testing standards

2.5.10.1 SAE standards

SAE standard J1269, introduced in 1979, is a multi-point test where the rolling resistance of a tyre is measured at combinations of three tyre pressures and two loads at 80 km/h (Evans et al., 2009). This results in four discreet measurement points at specific pressure/load combinations and skim loads must be subtracted from the data at each testing point (Evans et al., 2009). The data can then be fitted to a least squares regression model to predict the rolling resistance at any tyre pressure and load combination (Evans et al., 2009).

In 1999 a new testing standard, SAE J2452, was introduced which measures rolling resistance under coast down conditions where the speed is reduced from 115 km/h to 15 km/h in a step-wise fashion (Grover, 1998). The speed of the tyre must be reduced according to a defined coastdown curve, shown in Figure 2.13. A 1.7 m drum with a medium surface texture (80 grit) is used. The data is then fitted to an empirical model, as shown in Equation 2.21 (Grover, 1998).

$$F_{rr} = P^{\alpha} {F_Z}^{\beta} (a + b v_x + c {v_x}^2) \qquad \text{Equation 2.21}$$

In the above, P is tyre inflation pressure in kPa, F_Z is applied vertical load in N, v_x is speed in km/h, α, β, a, b and c are coefficients.

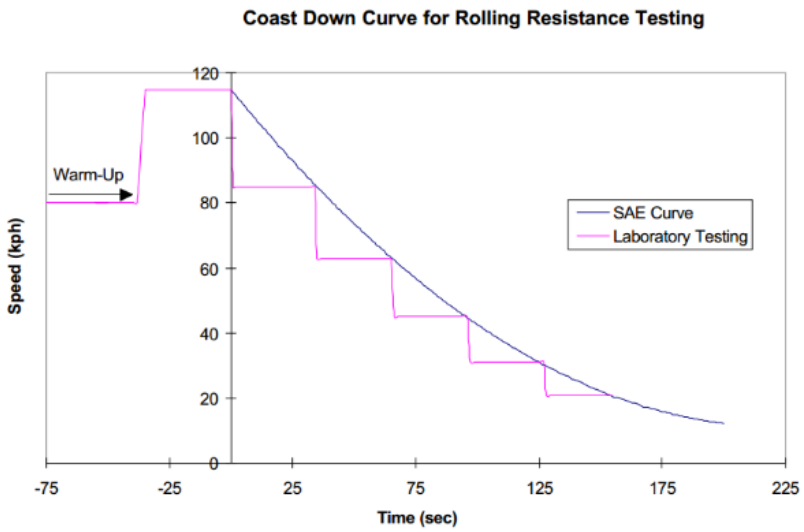

Figure 2.13. Curve for coastdown rolling resistance testing (Grover, 1998).

Equation 2.21 can be used to predict the rolling resistance force at any tyre inflation pressure, load and speed combination. Grover (1998) compared the measured rolling resistance of tyres at a wide range of load/pressure conditions with values calculated using Equation 2.21. The results showed a correlation of greater than 0.99 between measured and calculated values which indicates that this model should be preferred for modelling rolling resistance test data. The range of α for modern radial construction pneumatic tyres is 0.3 to 0.5 and β is 0.8 to 1.1 but is mostly less than 1 (Hall & Moreland, 2001).

The standard also defines a mean equivalent rolling force (MERF) which computes an average rolling resistance of a particular tyre at a certain inflation pressure and load over the duration of a particular drive cycle, from time t_0 to time t_f. MERF can be computed using Equation 2.22 (Hall & Moreland, 2001).

$$MERF = \frac{\int_{t_0}^{t_f} P^{\alpha} F_Z^{\beta} (a + bv_x + cv_x{}^2) dt}{\int_{t_0}^{t_f} dt} \qquad \text{Equation 2.22}$$

2.5.10.2 ISO standards

In 2005, the ISO 18164 standard was published for measuring rolling resistance which is very similar to SAE J1269 except this standard only uses a multi-point test. ISO 28580 was then released in 2009 which tests rolling resistance at a single test point at a standard load, pressure and speed on a 2.0 m smooth drum. The advantage of this standard is that results are standardised across all laboratories by a Round Robin Test where two test tyres are tested on a reference

machine and then sent to a candidate laboratory for calibration. This standard is used extensively to compare the rolling resistance of tyres as the values are standardised and easier to compare as it is a single value (Sandberg, 2011).

2.6 Suspension losses

A vehicle's suspension system is one of the most critical parts of any vehicle. It is responsible for absorbing road asperities as well as proper vehicle handling and ride comfort. The energy absorbed by the suspension system, in the form of vibrational energy, is ultimately dissipated to the environment in the form of heat (Zhang, Guo, Wang, Chen, & Li, 2017). Although this energy loss is caused by road roughness, the original energy source is the vehicle's powertrain (Zhang et al., 2017). Therefore in vechicles, suspension energy losses ultimately result in the reduction of overall vehicle energy efficiency. Vibrational loads are absorbed by three mechanisms in passenger vehicles; the tyre, the spring and the damper. Most of the energy is absorbed by the damper through the conversion of linear motion to thermal energy by dampening oil (Zhang et al., 2017).

Tests conducted by Audi AG, revealed that cars travelling on typical German roads have an average recovery power potential of 150 W, ranging from 3 W on newly paved roads to 613 W on uneven country roads (Zhang et al., 2017). Energy recovery is directly proportional to the speed of the vehicle and is strongly dependant on the roughness of the road (Zhang et al., 2017). Figure 2.14 shows the potential energy to be recovered from suspension energy losses based on vehicle speed and road roughness class for light passenger vehicles (Zhang et al., 2017). The analyses focused only on the vertical motion of the vehicle and does not consider vehicle pitch and roll. Also, energy dissipated by the tyre and spring and the efficiency of the conversion process is ignored as these losses are small compared to damper losses (Zhang et al., 2017).

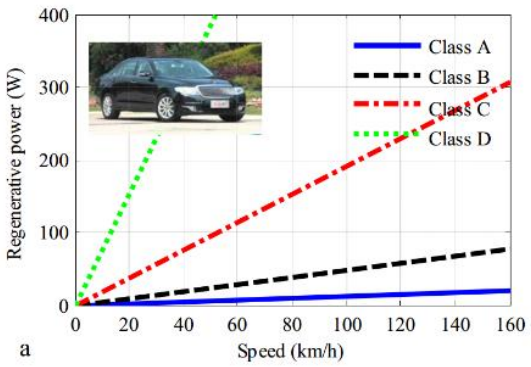

Figure 2.14. Average regenerative power of light vehicle suspension systems (Zhang et al., 2017).

Proper interpretation of Figure 2.14 requires an understanding of the road types represented by the various classes. Class A is classified according to the ISO Power Spectral Density as a very good road surface, class C as an average road surface and class D as a poor road surface (Ngwangwa, Heyns, Breytenbach, & Els, 2014). These can be further interpreted by the International Roughness Index where class A roads are considered as new road surfaces and class B as maintained but damaged or unpaved road surfaces (Ngwangwa et al., 2014).

2.6.1 Implementing suspension regeneration

Various technologies are being explored to recover damping losses from vehicles. One such technology is an electromagnetic damper, where a traditional damper is replaced with a magnet which is allowed to move within a coil (Wei & Taghavifar, 2017). Movement of the magnet within the coil generates an electrical potential according to Faraday's Law and can charge the battery pack (Wei & Taghavifar, 2017). Another technology being investigated is the use of piezoelectric materials in place of a damper. Piezoelectric materials allow for the conversion of mechanical stress into electrical energy and therefore also show promise for harvesting energy losses from tyre vibrations (Wei & Taghavifar, 2017).

2.7 Aerodynamic drag

The final resistance force to consider is aerodynamic drag. As any vehicle moves forward, it must overcome the resistive forces imparted by the surrounding air as the vehicle moves through it. These resistive forces, known collectively as aerodynamic drag, comprises three parts for vehicles (Guzzella & Sciarretta, 2013; Vodovozov, Raud, Lehtla, Rassolkin, & Lillo, 2014):

1. Viscous skin friction in the boundary layer of the vehicle surface
2. Induced drag due to vortices generated behind the vehicle
3. Pressure drag due to pressure differences at the front and rear of the vehicle caused by air separation

Pressure drag dominates aerodynamic losses and therefore the first two components are typically neglected (Vodovozov et al., 2014). In standard passenger vehicles 65 % of the aerodynamic losses are a result of the car body bulk geometry and the remaining comprises 20 % due to wheel housings, exterior mirrors, antennae, window housings, etc. and engine ventilation accounts for the remaining 5 % (Guzzella & Sciarretta, 2013). For EVs, the proportion of engine ventilation will decrease as electric motors require less heat removal than IC engines (Larminie & Lowry, 2013).

Computational fluid dynamics (CFD) can be used to determine the aerodynamic losses at particular flow conditions however this is a computationally expensive process and it is therefore impractical to calculate the force at multiple loading points such as wind speed and direction (Guzzella & Sciarretta, 2013). Typically, the vehicle is represented as a simplified prismatic body with frontal area, A_f and the aerodynamic force opposing this body is estimated by multiplying the pressure drag by an aerodynamic drag coefficient C_d, which accounts for actual flow conditions (Guzzella & Sciarretta, 2013). The resulting approximation of the force due to aerodynamic drag, F_{ad} can be computed using Equation 2.23 (Guzzella & Sciarretta, 2013).

$$F_{ad} = \frac{\rho_{air} C_d A_f}{2} \cdot (v_x \pm v_{wind})^2 \qquad \text{Equation 2.23}$$

In the above, ρ_{air} is the density of the ambient air and v_{wind} is headwind speed.

C_d is computed using CFD and can be assumed as constant across vehicle drive cycles (Guzzella & Sciarretta, 2013). It typically ranges from 0.3 to 0.5 for passenger vehicles (Vodovozov et al., 2014). EVs can have typically lower values, as low as 0.19, due to reduced under-vehicle piping, flexibility in the placement of components and the reduced need for engine cooling (Larminie & Lowry, 2013). C_d can also be expressed as a function of the apparent wind angle in relation to the direction of travel, known as yaw angel (Altinisik, Yemenici, & Umur, 2015; United Nations, 2015). The effect of yaw angle on C_d can be determined empirically and fitted to a four term polynomial, with a typical characteristic shown in Figure 2.15 (Altinisik et al., 2015).

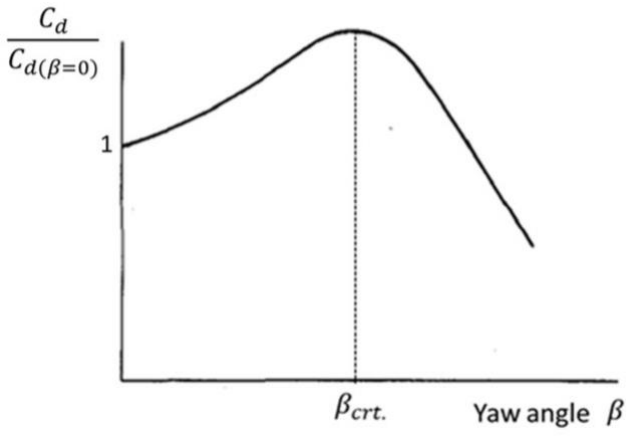

Figure 2.15. Typical effect of yaw angle on aerodynamic drag coefficient (Altinisik et al., 2015).

If a constant aerodynamic force is assumed, as yaw angle increases, C_d is expected to increase according to Equation 2.23 as the free stream velocity decreases with an increase in yaw angle (Altinisik et al., 2015). However experimental data has shown a decrease in F_{ad} as the yaw angle increases and therefore C_d begins to decrease after a critical yaw angle, usually 20° to 35° (Altinisik et al., 2015).

The density of air can vary with altitude, humidity and temperature but is typically assumed as a constant value of 1.25 $kg \cdot m^{-3}$ which is a reasonable approximation for vehicle modelling (Larminie & Lowry, 2013).

2.8 Traction motor

Electric motors have historically been involved in a vast array of stationary applications, particularly in the industrial sector. Induction motors are commonly used as they can be operated directly off a three phase AC grid supply and they are robust and relatively inexpensive as they have no permanent magnets (Guzzella & Sciarretta, 2013). This has led to the design and development of a wide range of induction motors suitable for the industrial sector. The requirements of electric motors for EVs are however different to stationary applications. The design objectives of motors for EVs are (Vodovozov et al., 2014):

1. To have high energy efficiency over typical EV drive cycles to reduce the demand on the battery pack and increase vehicle range
2. To operate efficiently at a large range of operating points over a wide operational envelope
3. To provide a peak torque output of at least four times the continuous rating for hill climbing or short periods of high acceleration
4. To operate within a speed range suitable for both city driving and high speed highway driving (up to four times rated speed)
5. To offer high specific power to optimise vehicle mass
6. To withstand the harsh operating environment of automobiles
7. To offer high controllability during both dynamic and steady-state operation
8. Allow for multiple starts and stops during city and high traffic driving
9. Allow for the recovery of energy during braking (operate as a generator)

The most commonly used electric drives to fulfil the above requirements are (Nanda & Kar, 2006; Vodovozov et al., 2014):

1. Permanent magnet synchronous machines (PMSM)
2. Asynchronous induction machines (ICM)
3. Switched reluctance machines (SRM).
4. Brushed DC motors.

All electric motors require a rotating magnetic field which can be achieved through either electrical or mechanical commutation. In the case of brushed DC motors, mechanical commutation is implemented through brushes and collectors and for PMSM, SRM and ICM motors, electrical commutation is achieved through a multi-phase AC supply. Friction between the brushes and collectors in DC motors causes a drop in motor efficiency and service life due to wear on the brushes (Guzzella & Sciarretta, 2013). A comprehensive comparison of all motor properties for each type of motor is considered in Table 2.4, where a higher score is considered more desirable.

Table 2.4. Comparison of EV motor technologies (Nanda & Kar, 2006; Yildirim, Polat, & Kürüm, 2014).

	Efficiency	**Reliability**	**Cost**	**Availability**	**Power density**	**Controllability**
PMSM	5	4	3	4	5	4
ICM	4	5	5	5	4	5
SRM	4	5	4	3	4	3
DC	2	2	4	5	3	5

Brushed DC motors are seldom selected for EV applications due to the low energy efficiency of the motors. This leaves EV designers with the choice of PMSM, ICM and SRM motors. SRM motors have been identified as a promising technology for EVs however they are not readily available and suffer from high noise and torque ripple (Yildirim et al., 2014). Therefore PMSM and ICM are the most common drives used for EV applications. Induction motors are relatively inexpensive due to a high utilization factor in stationary grid applications and have high efficiencies (Vodovozov et al., 2014). However PMSM motors have the highest efficiency and have increased power density but are typically more expensive than induction drives due to the utilisation of rare-earth permanent magnets (Goss, Mellor, Wrobel, Staton, & Popescu, 2012).

Although ICM motors are readily available, most commercially available designs are high speed and low torque designs and therefore a gearbox is required to step up the torque. The addition of

a gearbox reduces the total drivetrain efficiency and increase cost and complexity of the drivetrain. Therefore when considering the full EV drivetrain, PMSM motors are often the best choice and are commonly used for EVs (Park et al., 2014). Therefore only PMSM motors are considered further.

It should be noted that another class of motors exists, brushless DC (BLDC) motors, which are similar in construction to a PMSM motor and require a similar three phase AC current source to PMSM motors despite what their name implies. The difference between PMSM and BLDC is the type of winding used, for PMSM motors, the stator windings are distributed and for BLDC the windings concentrated, which causes a sinusoidal and trapezoidal back electromotive force (BEMF) response respectively (Guzzella & Sciarretta, 2013). PMSM motors are a preferred choice over BLDC motors as they have a higher power density, less torque ripple and higher peak efficiencies (Torres, 2009).

2.8.1 PMSM structure

Three phase PMSM motors consist of a stator with one or more sets of three phase windings, which produce a rotating magnetic field when a three phase sinusoidal AC source is applied. The rotor consists of pairs of permanent magnets which generate a stationary magnetic field which interacts with the rotating stator field to cause rotation of the rotor. The number of sets of windings and pairs of rotor poles is called the number of motor poles (Guzzella & Sciarretta, 2013). This structure is shown in Figure 2.16, as well as the difference in structure between interior and exterior rotor topologies. Exterior-rotor motors can be used as hub motors where the rotor is connected directly to the wheel.

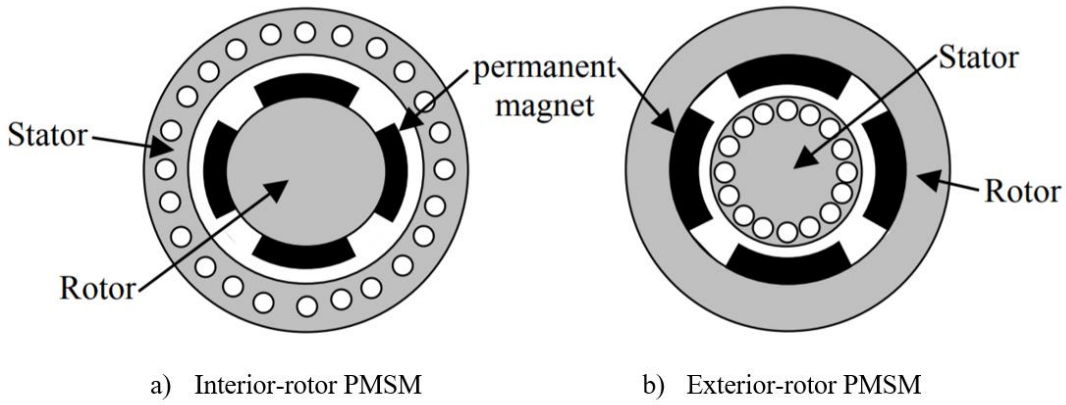

Figure 2.16. PMSM structure (Meier, 2001).

There are two main types of PMSM motors, surface PMSM (SPM) and interior PMSM (IPM) (Kulkarni & Thosar, 2013). In SPM, magnets are mounted on the surface of the rotor whilst for IPM motors magnets are buried within the rotor as depicted in Figure 2.17. Buried magnets are more robust and therefore suited to high speed operation and result in a more uniform air gap however they increase the cost and complexity of the design (Kulkarni & Thosar, 2013).

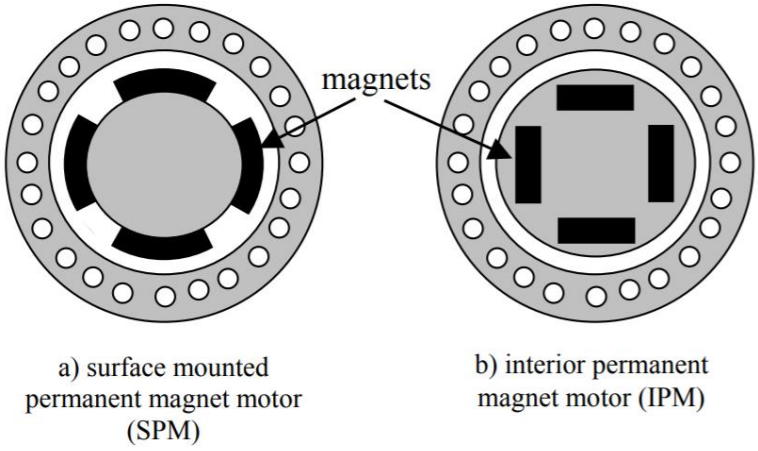

Figure 2.17. Cross sections of PMSM motor types (Meier, 2001).

2.8.1 PMSM operating regions

The three operating regions of a PMSM motor are shown in Figure 2.18. The first mode, Mode I is a constant torque region where the motor operates at rated flux. As the speed of the motor is increased, BEMF opposes the applied stator voltage. When the BEMF reaches the maximum voltage of the inverter, the speed of the motor can no longer be increased. The speed at this point is defined as the base speed of the motor (Goss, Mellor, Wrobel, Staton, & Popescu, 2012).

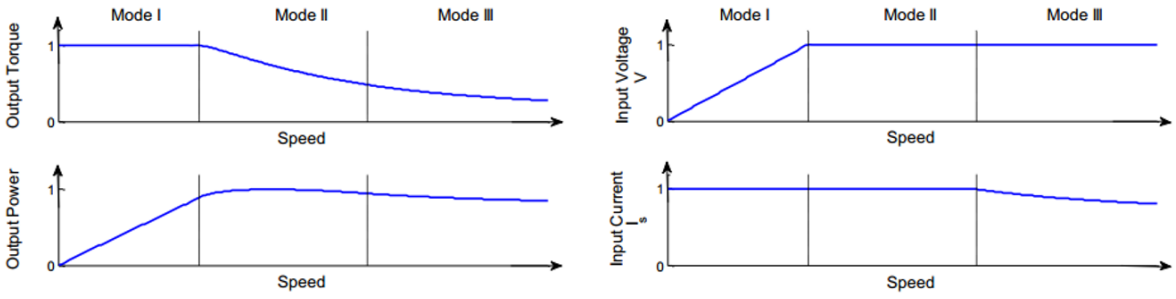

Figure 2.18. Operation regions of a BLAC PM motor (Goss et al., 2012).

In order to increase speed beyond the base speed, a strategy known as field weakening can be employed where a demagnetising current is used to decrease the permanent magnet flux which in turn decreases the BEMF and torque output of the motor (Goss et al., 2012). When field weakening is employed, the motor enters its second stage of operation, Mode II. Any increase in speed in this region will cause a decrease in motor torque.

As the speed of the motor is increased, a higher demagnetising current is required. At some point the total current vector will exceed the maximum current output of the motor drive and therefore the demagnetising current will be at a maximum value and the motor will enter the final operational mode, Mode III. To increase the speed of the motor beyond this point the demagnetising current is kept at maximum and the torque producing current component is decreased, thereby reducing the total current vector (Goss et al., 2012).

2.8.1 PMSM energy loss characterisation

Energy losses in PMSM motors can be considered in terms of losses that increase with the speed of the motor, losses that increase with the torque of the motor and losses that increase with both torque and speed at extremes of motor operation (Petro, 2011). Losses that increase with the speed of the motor are iron or core losses comprising eddy and hysteresis losses and frictional bearing and windage losses (Groschopp, 2015). Windage losses are associated with air turbulence acting against the motion of the rotor. Mechanical losses due to windage and bearing friction are typically ignored as they negligible compared to the magnitude of eddy and hysteresis losses. It is difficult to find an accurate analytical expression for core power losses, P_{Core} and it is therefore typically estimated using the empirical approximation shown by Equation 2.24 (Rabiei, Thiringer, & Lindberg, 2012).

$$P_{Core} = k_{eddy} {f_m}^2 B^2 + k_{hyst} f_m B^2 + k_{ex} {f_m}^{1.5} B^{1.5} \qquad \text{Equation 2.24}$$

In the above, f_m and B are the motor frequency and peak flux density and k_{eddy}, k_{hyst} and k_{ex} are coefficients relating to eddy current, hysteresis and excess losses.

The coefficients in Equation 2.24 must be experimentally determined, calculated according to a magnetostatic finite element field or determined using an analytical solution (Mellor, Wrobel, & Holliday, 2009). A commonly used experimental technique is a no-load loss approximation where it is assumed that losses at no-load are dominated by core losses and power loss is measured at discrete points across the speed range of the motor (Rabiei et al., 2012). In the case of finite

element or analytical approaches, the exact motor geometry and design must be known (Mellor et al., 2009). A typical iron loss versus motor frequency curve is shown in Figure 2.19.

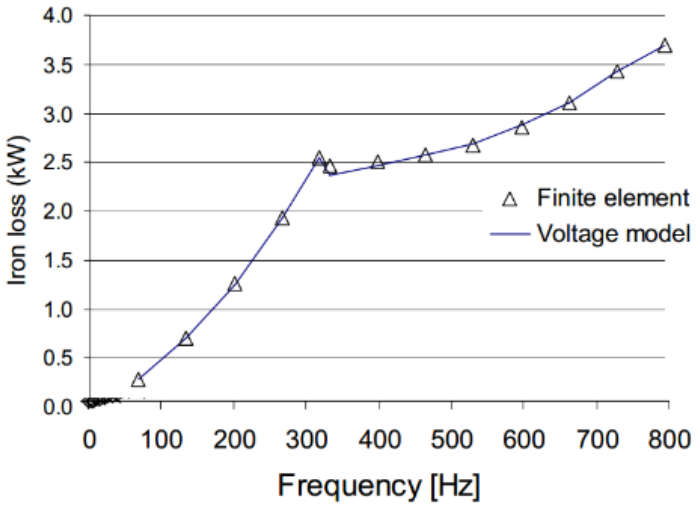

Figure 2.19. Iron losses compared to PMSM motor speed (Amjad, Rudramoorthy, Neelakrishnan, Sri Raja Varman, & Arjunan, 2011; Mellor et al., 2009).

Winding or copper losses relate to the ohmic resistance of the stator windings. As ohmic power losses are directly proportional to the square of current, which increases proportionally with torque, these losses are dependent on motor torque (Rabiei et al., 2012).

In Mode I, losses are dominated by copper losses as core losses only become significant in Mode II, as the speed of the motor is increased (Mellor et al., 2009). In Mode II, where field weakening is employed, magnetic excitation is decreased which causes a decrease in iron losses (Mellor et al., 2009). The shift in dominant losses from low to high speed operation is evident in the experimental data obtained from an IPM motor operating at rated torque shown in Table 2.5.

Table 2.5. Comparison of performance at 1500 rpm and 6000 rpm of a PMSM motor (Dorrell, Knight, Popescu, Evans, & Staton, 2010).

Speed = 1500 rpm				
Torque [Nm]	Current [Arms]	Iron loss [W]	Copper loss [W]	Eff. [%]
303	141.1	198	4328	91.3
Speed = 6000 rpm				
Torque [Nm]	Current [Arms]	Iron loss [W]	Copper loss [W]	Eff. [%]
45.6	31.8	953	219	96.1

2.8.2 Quasistatic PMSM modelling

The motor is one of the most complicated components of an EV to model and simulate (Gao et al., 2007). The primary concern of motor modelling is to compute the efficiency of the motor at each operating point (shaft torque and angular speed combinations) of the motor. Efficiency contour maps, for example that of Figure 2.20, are often used as means of populating a look-up table of efficiency values. These maps define motor efficiency at a particular torque and speed value based on a particular control strategy (Stipetic & Goss, 2016). Whilst these maps allow for quick and accurate estimation of motor efficiency, they are not often provided by manufactures and they do not allow for the simulation of dynamic motor properties (Gao et al., 2007).

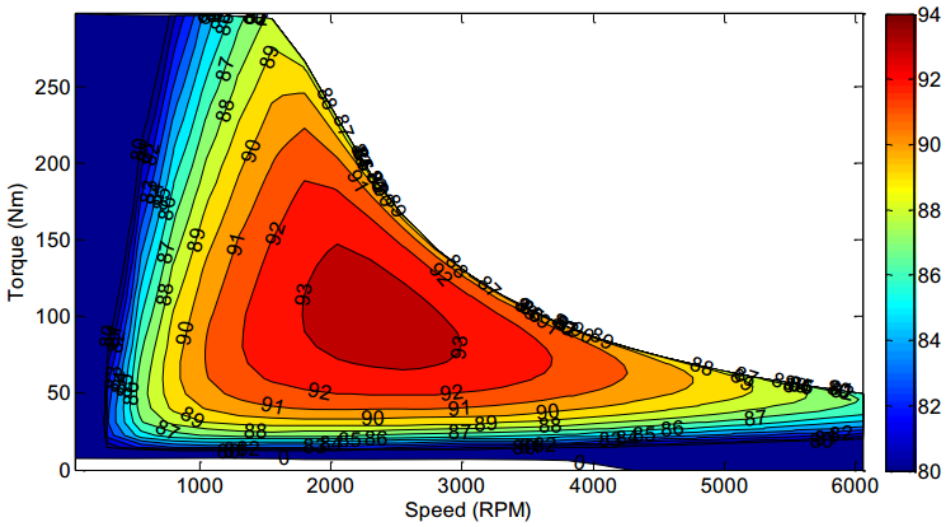

Figure 2.20. Generated contour efficiency map for a 2004 Toyota Prius motor (Goss, Mellor, Wrobel, Staton, & Popescu, 2012).

Another challenge presented by using efficiency contour maps is that the efficiency values are only true for operation in the positive torque region and not during regenerative braking when torque is negative (Guzzella & Sciarretta, 2013). Therefore the efficiency map for positive torque values cannot be mirrored to the negative torque region. This can be seen from Figure 2.21 which shows measured efficiency values of a typical EV traction motor. A more suitable approach is to mirror the power losses at each operating point, which yields Equation 2.25 (Guzzella & Sciarretta, 2013).

$$\eta_m(\omega_m, -|T_m|) = 2 - \frac{1}{\eta_m(\omega_m, |T_m|)} \qquad \text{Equation 2.25}$$

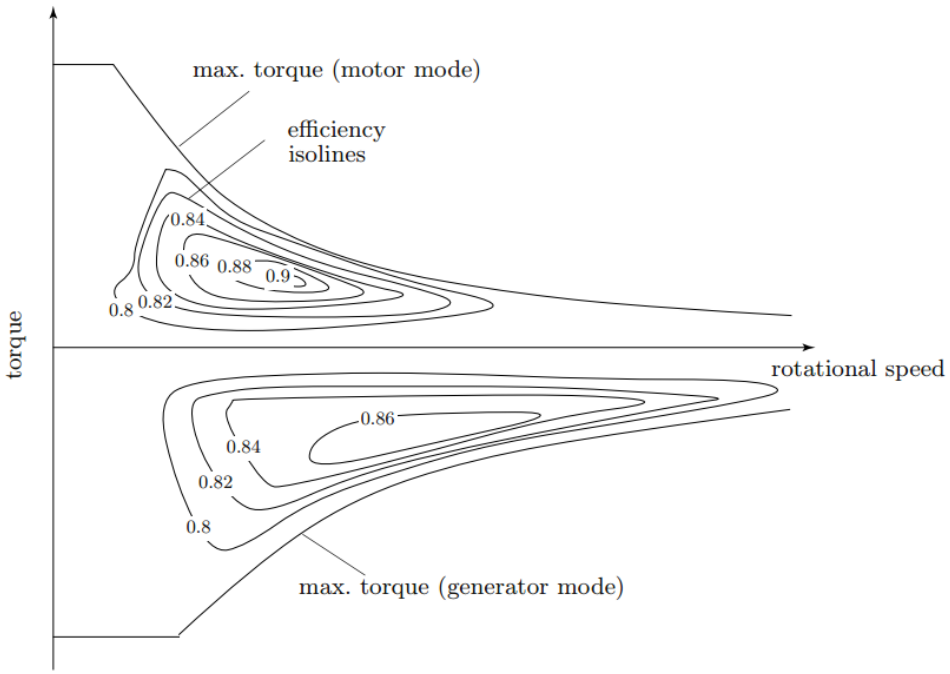

Figure 2.21. Efficiency map of a typical traction motor for both positive and negative torque values (Guzzella & Sciarretta, 2013).

2.8.3 PMSM dynamic modelling

A second approach to modelling PMSM motors is through dynamic modelling which models the speed and torque capabilities more accurately than the quasi-steady approach (Gao et al., 2007). Figure 2.22 shows two common reference frames used in the analysis of PMSM motors. The stationary stator reference frame, where *u*, *v* and *w* represent the direction of positive flux produced by each stator winding (Dajaku & Gerling, 2007). The rotating *dq* reference frame can also be used where the *d* axis is an axis of symmetry which intersects a rotor pole and the *q* axis is an axis of symmetry between poles, as shown in Figure 2.22 (Dajaku & Gerling, 2007).

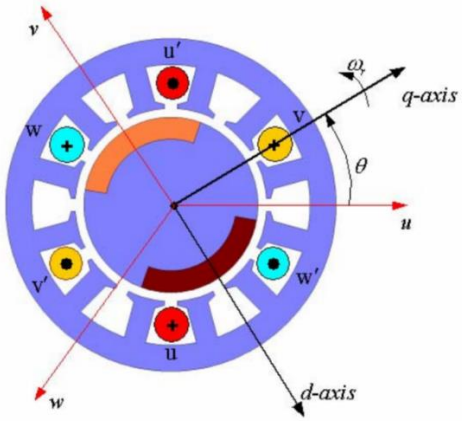

Figure 2.22. Schematic of a PMSM (Dajaku & Gerling, 2007).

Dynamic motor models are typically modelled in the rotating *dq* reference frame to simplify dynamic relationships and to simplify the control of motor torque. The *dq* axes voltage components, $u_d(t)$ and $u_q(t)$ for a three phase PMSM motor can be solved by applying Kirshoff's law to the equivalent circuit shown in Figure 2.23 to give Equation 2.26, Equation 2.27 and Equation 2.28 (Park et al., 2014).

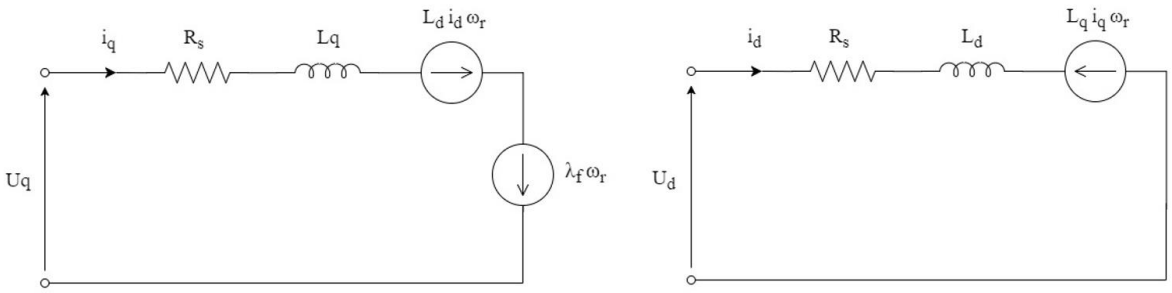

Figure 2.23. Equivalent PMSM circuit.

$$u_q(t) = R_s i_q(t) + \frac{d\lambda_{qs}}{dt} + \omega_r \lambda_{ds} \qquad \text{Equation 2.26}$$

$$u_d(t) = R_s i_d(t) + \frac{d\lambda_{ds}}{dt} - \omega_r \lambda_{qs} \qquad \text{Equation 2.27}$$

$$\lambda_{ds} = L_d i_d + \lambda_f, \lambda_{qs} = L_q i_q \qquad \text{Equation 2.28}$$

In the above, $i_d(t)$ and $i_q(t)$ are the *dq* axes components of the stator current, R_s is the stator resistance, L_d and L_q are the *dq* axes inductances, ω_r is the electrical angular speed of the rotor, λ_{qs} and λ_{ds} are the *dq* axes stator flux linkage components, λ_f is the flux linkage due to the rotor magnets and *N* is the number of pole pairs.

If the motor is operated in the field weakening region or under high current conditions, the linear approximations given by Equation 2.28 become inaccurate due the effects of cross coupling and saturation (Qi et al., 2008). An example is shown in Figure 2.24. Also the stator resistance increases with an increase in temperature and the permanent magnet flux decreases (Goss et al., 2012).

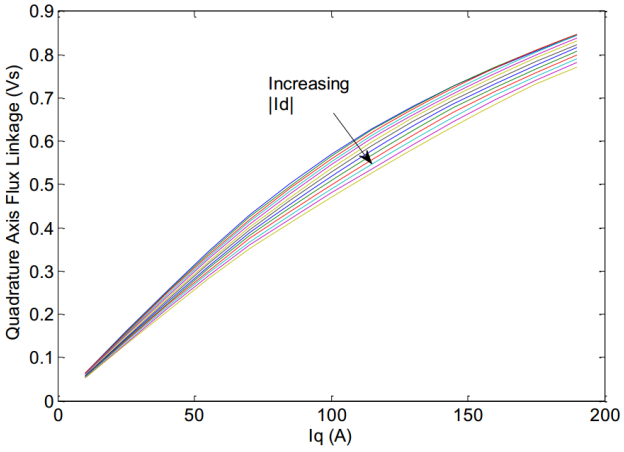

Figure 2.24. Variation of λ_{qs} with i_q and i_d (Goss et al., 2012).

By expanding Equation 2.26 using Equation 2.28, it can be seen that a term, $\omega_r \cdot \lambda_f$, will oppose the applied q axis voltage resulting in the phenomenon known as BEMF. The electromagnetic torque produced by the motor, T_{em} can be expressed as Equation 2.29 (Goss et al., 2012).

$$T_{em} = \frac{3N}{2}\left[\lambda_f i_q + (L_d - L_q) i_d i_q\right] \qquad \text{Equation 2.29}$$

For a non-salient machine, where $L_d = L_q$, the term $(L_d - L_q)$ falls away and in the case of salient machines where $L_d < L_q$, torque is generated as a result of the difference of d and q axis inductance, known as reluctance torque (Goss et al., 2012). SPM motors are non-salient motors as the effect of the permanent magnets on *dq* inductance is independent of rotor position. The relationship between the line inductance in the *uvw* frame to inductance in the *dq* frame is given by Equation 2.30 for non-salient machines (MathWorks™, 2017d).

$$L_d = L_q = \frac{L_{line(uvw)}}{2} \qquad \text{Equation 2.30}$$

The dynamic equation of a PMSM motor can be used to compute the output torque of the motor, T_m using Equation 2.31 and Equation 2.32 (Park et al., 2014).

$$T_m = T_{em} - B_m \omega_m - J_m \frac{d\omega_m}{dt} \qquad \text{Equation 2.31}$$

$$\omega_m = \frac{\omega_r}{N} \qquad \text{Equation 2.32}$$

In the above, ω_m is the rotor angular speed, B_m is the viscous friction coefficient and J_m is the rotor moment of inertia.

The above equations consider only the stator copper losses and mechanical friction but ignore core losses. Core losses can be represented an extra resistance, R_c as shown in Figure 2.25 which is typically determined through experimental measurements (R. Palka, 2016). According to Equation 2.24, core losses are function of motor speed and therefore R_c must increase with motor speed. Figure 2.26 shows the relationship between speed and R_c for a 50 kW PMSM measured through a no-load experimental analysis.

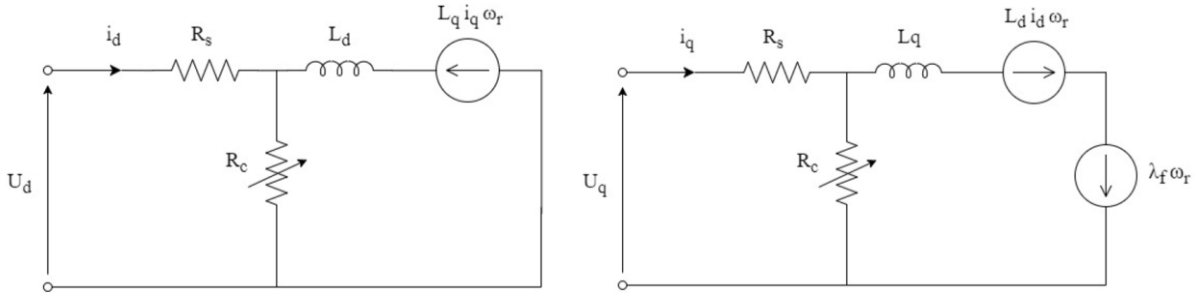

Figure 2.25. Equivalent PMSM circuit with core losses.

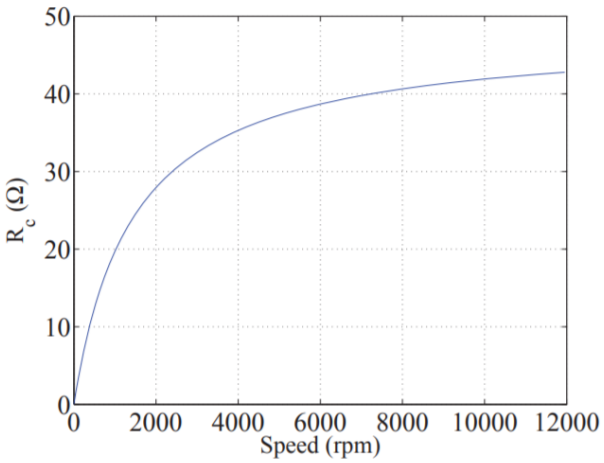

Figure 2.26. Relationship between R_c and motor speed (A. Rabiei, 2012).

2.8.4 Regenerative braking limitations

When the motor acts as a generator, torque becomes negative as it acts in a direction to oppose the motion of the vehicle. It can be assumed that the torque and speed limits can be mirrored to the negative torque region (Genikomsakis & Mitrentsis, 2017). The magnitude of regenerative braking is further limited by the SOC and temperature of the battery as the battery must be able

to accept the energy produced from braking (Yeo, Kim, Hwang, & Kim, 2004). The maximum charging current into the battery, and therefore the magnitude of regenerative braking, may be decreased linearly to zero as the battery reaches a 100 % SOC (Yeo et al., 2004). Alternately regenerative braking can be set to zero when the SOC of the battery is above a certain SOC threshold.

At low speeds, little regenerative energy is available and driver comfort may be infringed (Yeo et al., 2004). Therefore regenerative braking is often disabled at low speeds (Day, 2014; Larminie & Lowry, 2013; Yeo, Kim, Hwang, & Kim, 2004). Regenerative braking is also be disabled under emergency braking or when an ABS or TCS acts to maintain vehicle stability.

2.8.5 PMSM control

Various control strategies can be implemented to control PMSM motors. One such strategy is the maximum torque per ampere (MTPA) strategy which aims to minimise the stator current vector for a given torque value. It can be easily inferred from Equation 2.29 that i_d does not increase the torque output of the motor for non-salient motors and therefore the MTPA strategy is simply achieved by setting the value of i_d to zero (Guzzella & Sciarretta, 2013). In order to operate the motor in Mode II and Mode III the value of i_d can be set to a non-zero value to magnetise the permanent magnet field.

This strategy does not however ensure the motor operates at the highest efficiency over the full torque speed envelope, especially at higher speeds where iron losses become dominant (Goss et al., 2014; Stipetic & Goss, 2016). Maximum efficiency control strategies may be implemented, such as increasing the demagnetising current (i_d) at higher speeds, to reduce the iron losses which increase with motor speed (Goss et al., 2014). Although an increase in i_d causes an increase in the total current vector, and therefore copper losses, there is a point where the decrease in iron losses exceeds the increase in copper losses (Goss et al., 2014).

As the power source in an EV is a battery pack which provides DC power, power electronics are required to convert the DC voltage to a three phase AC voltage to drive the motor. A voltage source inverter with variable amplitude voltage and frequency is typically used as this also allows for control of the motor torque and speed (Iqbal, Lamine, Ashraf, & Mohibullah, 2006). In an EV, the combination of an inverter and control loop is known as the motor controller. The motor controller receives a requested torque input from the driver or speed control system which can be used to determine a reference *dq* current using Equation 2.29, which is then transformed into the *uvw* reference frame to drive the motor.

In order to set the motor current to the requested current, the input voltage is varied to achieve the desired current using a proportional-integral (PI) feedback control loop as shown in Figure 2.27. The output voltage of the stator must be transformed back to the *dq* reference to allow feedback in the PI loop, which requires the position of the rotor for the transformation. The motor must therefore use a position determining devise such as Hall Effect sensors. The variable voltage and frequency of the inverter is achieved using pulse width modulation (PWM) (Park et al., 2014).

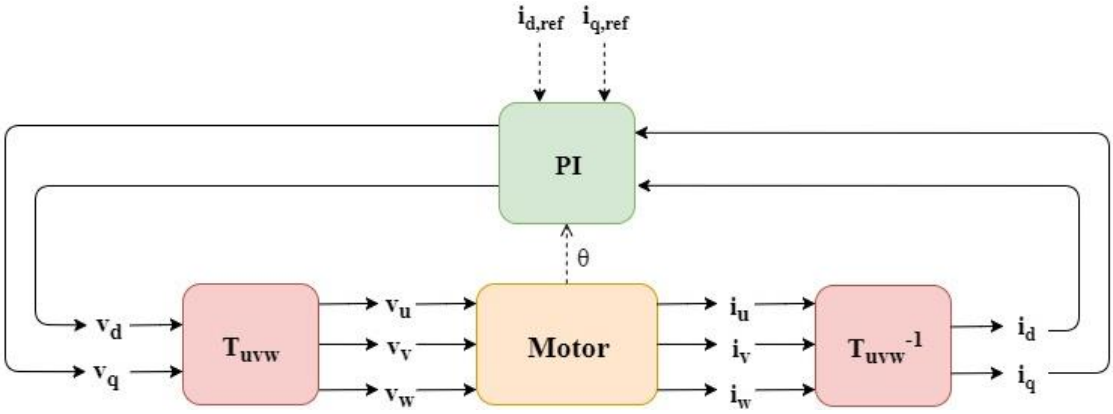

Figure 2.27. PMSM control loop.

PWM is realised using fast semiconductor switches such as insulated-gate bipolar transistors (IGBTs) used for higher power controllers or metal–oxide–semiconductor field-effect transistors (MOSFETs) used for lower power controllers (Guzzella & Sciarretta, 2013). Six of these switches are used in a configuration shown in Figure 2.28. The on/off duty of the switches determines the voltage of the output and the switching sequence determines the frequency of the output. The on/off control signal for each switch is commonly determined using a technique called Space-Vector Modulation (SVPWM) (Guzzella & Sciarretta, 2013). This technique will not be disccused in this work however the imposed limitation of the DC bus voltage, V_{Batt} on the maximum motor phase voltage, $V_{phase,max}$ must be considered according to Equation 2.33 (Maamoun, Alsayed, & Shaltout, 2010).

$$V_{phase,max} = \frac{V_{Batt}}{\sqrt{3}} \qquad \text{Equation 2.33}$$

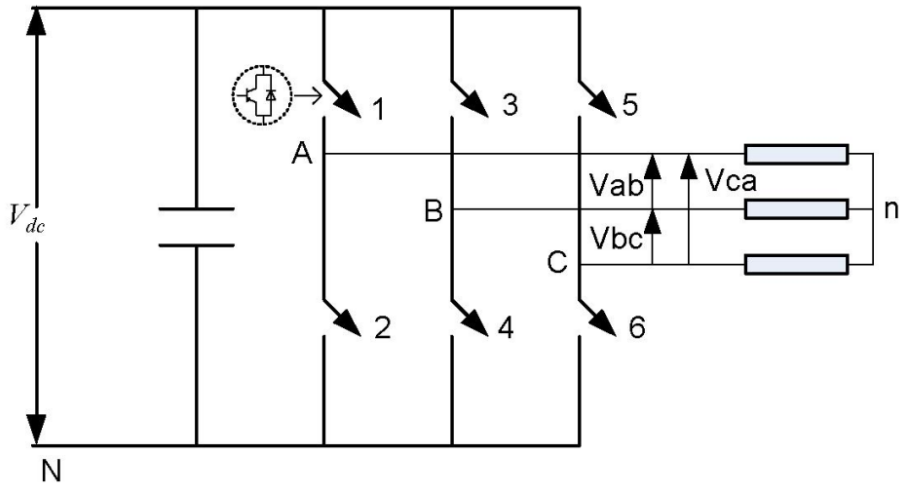

Figure 2.28. Three phase variable voltage and frequency inverter schematic (Iqbal et al., 2006).

2.8.5.1 Inverter losses

Voltage source inverters implemented using modern power electronics typically have high efficiencies in the range of 97 % to 99 % (Mazgaj, Rozegnal, & Szular, 2015). Losses in such inverters are dominated by losses from the semiconductor switching devise used and its associated free-wheeling diodes (Mazgaj et al., 2015). Losses in these components comprise switching losses and conduction losses (Mazgaj et al., 2015).

Switching losses are due to energy lost during both the switch-on and switch-off periods and depend on the DC voltage applied to the inverter, the load current and the dynamic characteristics of the semiconductor (Mazgaj et al., 2015). Conduction losses arise due the ohmic resistance of the semiconductor whilst in an on-state and depend on collector current, collector-emitter voltage and junction temperature (Mazgaj et al., 2015). Conduction power losses, P_{con} can be estimated using the drain-source on state resistance, R_{on} and Equation 2.34 (Graovac, Marco Pürschel , & Kiep, 2006).

$$P_{con} = \frac{1}{T_p} \int_0^{t_{con}} \left(R_{on} \cdot i_{drain}^2(t) \right) dt \qquad \text{Equation 2.34}$$

In the above, T_p is the switching period, $i_{drain}(t)$ is the drain current, and t_{con} is the transistor conduction time.

If the RMS value of the semiconductor on-state current, i_{Drms} is used, Equation 2.34 can be simplified to give Equation 2.35 (Graovac et al., 2006).

$$P_{con} = R_{on} \cdot i_{Drms}^2$$ Equation 2.35

In order to analyse inverter losses, the current and voltage waveforms of the semiconductor device must be understood and this usually requires a simplification in order to use datasheet values to characterise these dynamics (Mazgaj et al., 2015). A simplified approach is to use the rated switching loss energy, E_{sr} from the device's datasheet for a rated collector voltage, V_r and current, I_r (Hassan, 2011). The switching loss power for current and voltages other than the rated values can be linearly scaled according to Equation 2.36 (Hassan, 2011).

$$P_{sw} = \frac{E_{sw,r}}{T_p} \cdot \frac{V}{V_r} \cdot \frac{I}{I_r}$$ Equation 2.36

2.9 Li-ion batteries

Li-ion battery modelling has received a great deal of interest recently as li-ion batteries are becoming the preferred choice of energy storage for a vast array of applications (Erdinc, Vural, & Uzunoglu, 2009). Li-ion batteries offer very high energy and power densities making them superior to older chemistries such as lead acid and Nickel-Metal-Hydride (Seaman, Dao, & McPhee, 2014). Therefore li-ion batteries are being embraced by the EV industry. The battery pack is the most expensive component of an EV and therefore it is of critical importance to ensure that the cells operate within conditions that maximise the range of the vehicle as well as the usable life of the cells (Tie & Tan, 2013). It is also important to ensure that the cells are capable of meeting the demanding operating conditions of EV applications (Seaman et al., 2014).

Battery models are used for various applications in the EV sector, namely on-line state of charge estimation, control system development and drive cycle simulations (Seaman et al., 2014). This study will focus on battery modelling for drive cycle simulations as the other applications are not within the scope of this research. For such simulations the aims of the battery model should be the following (Min & Rincon-Mora, 2006):

1. Predict run-time and I-V performance for different load profiles
2. Optimise system performance
3. Improve battery energy efficiency

Researchers have developed a plethora of model types in attempt to model these effects, with different levels of model fidelity and complexity (Seaman et al., 2014). The three most prevalent methods for modelling li-ion cells are electrochemical modelling, equivalent circuit modelling and analytical models (Seaman et al., 2014).

2.9.1 Li-ion performance characteristics

Li-on batteries exhibit a variety of unique performance characteristics that must be accurately and efficiently represented by any battery modelling effort.

2.9.1.1 Dynamic voltage response

In its simplest form, a li-ion battery can be represented as an ideal voltage source. However in reality, numerous non-idealities exist which cannot be ignored when building an accurate system level EV battery model. All batteries exhibit the properties of an equivalent series resistance which causes an instantaneous drop in terminal voltage when discharging a cell and an increase whilst charging (Seaman et al., 2014). This effect is depicted in Figure 2.29 by the dashed "Voltage without depletion" line.

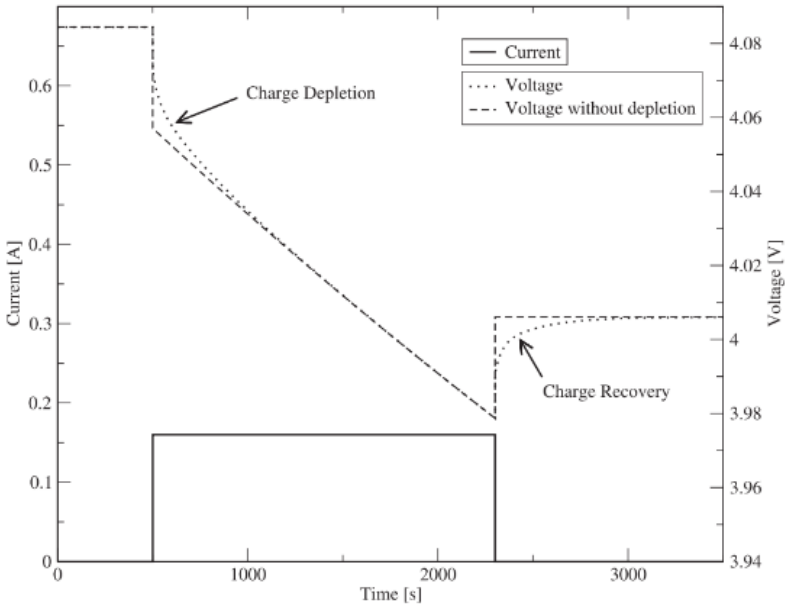

Figure 2.29. Charge depletion and recovery (Seaman et al., 2014).

Figure 2.29 also depicts the phenomena of charge depletion and recovery. Charge depletion and recovery are caused by the change in concentration of chemical products at the cathode and anode (Seaman et al., 2014). Charge depletion can be observed during discharge when the concentration of chemical products decreases over time and causes a drop in voltage. Once charging has stopped, the concentration increases as chemical products diffuse to the anode and cathode

causing a rise in cell voltage, a process known as charge recovery (Seaman et al., 2014). These effects can be observed in Figure 2.29 which compares the voltage response of a cell with and without the effects of depletion.

These effects result in a hysteretic effect which implies that a cell exposed to two different load profiles, with the same average current, can have very different runtimes (Petricca et al., 2013). Therefore a dynamic model is required to accurately predict the response of a cell under a different temporal current profiles (Petricca et al., 2013).

2.9.1.2 Usable capacity

The usable capacity of a cell can be defined as the energy that can be extracted from a cell under specific operating conditions (Min & Rincon-Mora, 2006). The usable capacity of a cell is affected by cycle number, storage time, temperature and discharge current (Min & Rincon-Mora, 2006). Figure 2.30 (a), (c) and (d) show that an increase in cycle number, discharge current and storage time causes a drop in the usable capacity of the cell. An increase in temperature however, increases the usable capacity of the cell (Figure 2.30(b)) but also accelerates electrode oxidation which reduces the service life of the cell (Seaman et al., 2014).

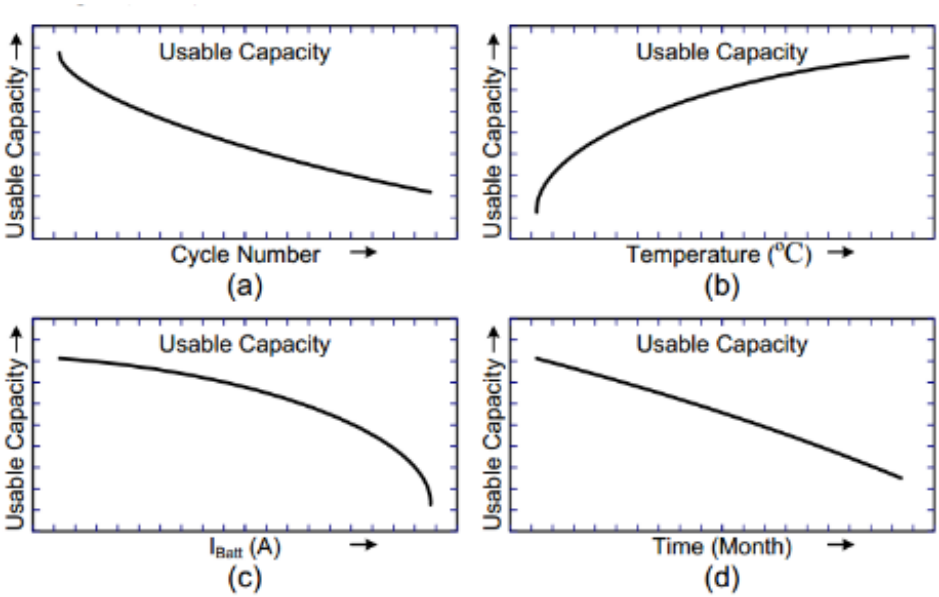

Figure 2.30. Typical effects of cycle number (a), temperature (b), discharge current (c) and storage time (d) on usable capacity of li-ion batteries (Min & Rincon-Mora, 2006).

2.9.2 Electrochemical models

Electrochemical models are the most accurate models as they explicitly represent the chemical processes within the cell as a series of highly non-linear differential equations (Seaman et al., 2014). The most widely used and accepted model is based on porous electrode theory and in many cases is used to validate other theoretical models (Seaman et al., 2014). Although these equations offer high model fidelity and are useful for optimising physical design aspects of batteries, they have high computational complexity making these models impractical to model multiple charge–discharge cycles (Min & Rincon-Mora, 2006). They also require a vast number of parameters which can be difficult to measure or obtain due to the proprietary nature of the cells (Min & Rincon-Mora, 2006).

2.9.3 Mathematical models

Mathematical or analytical models can be empirical or stochastic models that predict battery run-time, efficiency or capacity with an accuracy range of 80 to 95 % (Min & Rincon-Mora, 2006). Most of these models can only be applied to a specific system and can only predict system level parameters such as battery runtime, efficiency or capacity (Min & Rincon-Mora, 2006). The most common model is the Peukert Equation (Equation 2.37) which estimates the runtime of a battery empirically based on a constant current discharge (Min & Rincon-Mora, 2006).

$$LT = \frac{C_P}{{I_{Batt}}^k} \qquad \text{Equation 2.37}$$

In the above, C_p is the Peukert capacity in Ah, k is the Peukert coefficient, LT is battery runtime in hours and I_{Batt} is battery current in Amperes.

2.9.4 Equivalent circuit models

Equivalent circuit or electrical models represent the battery as a set of electrical components which can be structured in various ways to simulate the performance characteristics of li-ion cells. Although the fidelity of these models is lower than electrochemical models they are less computationally expensive (Seaman et al., 2014). The accuracy of these model types are typically 95 to 99 %, lying between electrochemical and mathematical models (Min & Rincon-Mora, 2006). Electrical models also offer other advantages such as ease of implementation, as they make use of basic circuit components, they are intuitive (Min & Rincon-Mora, 2006) and can be easily incorporated into system level EV models (Seaman et al., 2014). A disadvantage of these models is that they cannot be used to optimise physical design parameters of the cell such as the electrode size and composition (Seaman et al., 2014). Electrical models can be further broken down into

three sub categories, namely impedance, Thėvenin and run-time based models (Min & Rincon-Mora, 2006).

2.9.4.1 Impedance models

Impedance models are based on a parameter extraction technique known as electrochemical impedance spectroscopy (EIS). EIS is a process whereby a battery's voltage response to a range of low frequency AC signals is measured (Seaman et al., 2014). The batteries complex impedance can then be determined by analysing the magnitude and phase of this response (Seaman et al., 2014). EIS is not often used as a stand-alone model but rather to calculate the state of charge (SOC) or state of health (SOH) of a resting cell and it can be used in conjunction with a Kalman filter for online parameter estimation (Seaman et al., 2014).

2.9.4.2 Thėvenin models

The circuit diagram of a Thėvenin based electrical battery model is shown in Figure 2.31. R_S is a resistor placed in series which represents the equivalent internal series resistance of a battery. A number of resistor capacitor parallel networks ($R_i C_i$) are also placed in series to model the exponential decay of the voltage response with respect to current due to depletion (Seaman et al., 2014). The open circuit voltage (OCV) is represented as a constant ideal voltage source and simulates the OCV at a particular SOC. Whilst these models can capture the dynamic voltage response of a battery at a certain SOC they cannot predict battery runtime or steady-state voltage variations (Min & Rincon-Mora, 2006).

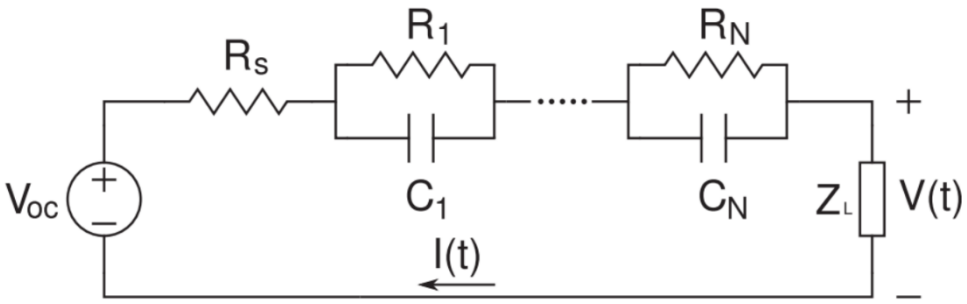

Figure 2.31. Thėvenin model of a li-ion cell (Seaman et al., 2014).

The fidelity of Thėvenin based models can be increased by making the components of the model dependant on internal states of the cell such as SOC and temperature or increasing the number of resistor-capacitor (RC) pairs (Seaman et al., 2014). As the number of RC pairs are increased the complexity and computational complexity of the model is also increased. Hanlei and Mo-Yuen (2010) studied the relationship between model fidelity and computational efficiency as the

number of RC pairs is increased and found that two RC pairs were a good compromise between model fidelity and computational complexity. However Kroeze and Krein (2008) found that the two RC pairs did not accurately predict the SOC of a hybrid electric vehicle (HEV) during a drive cycle simulation because accuracy for short duration loads (less than 1 s) which are expected from HEV drive cycles are lost.

2.9.4.3 Run-time models

Min and Rincon-Mora (2006) developed a comprehensive run-time model which added elements from Thėvenin models to existing run-time based models. The model developed is considered as a standard among equivalent circuit models (Petricca et al., 2013). The model consists of two separate circuits, a battery lifetime circuit on the left and a voltage response circuit on the right, as seen in Figure 2.32. The battery lifetime circuit consists of capacitor with capacitance, $C_{capacity}$ which is equal to the usable energy of the battery converted to a charge in coulombs. $C_{capacity}$ can be calculated by Equation 2.38 (Min & Rincon-Mora, 2006).

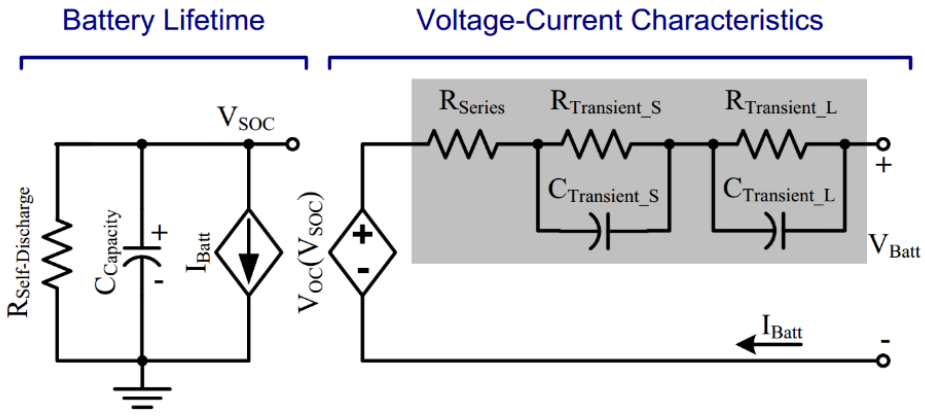

Figure 2.32. Modified run-time based model (Min & Rincon-Mora, 2006).

$$C_{Capacity} = 3600 \times C_N \times f_1(cycle) \times f_2(temp) \qquad \text{Equation 2.38}$$

In the above, C_N is the nominal cell capacity in Ah and $f_1(cycle)$ and $f_2(temp)$ are correction factors used to adjust the capacity of the cell according to temperature and the number of cycles. When the voltage across the capacitor, V_{SOC} is 1 V the SOC of the battery is 100 % and at 0 V it is 0 % (Min & Rincon-Mora, 2006). Therefore V_{SOC} is not a physical voltage but rather a quantitative indication of the SOC (Min & Rincon-Mora, 2006). The capacitor acts as a current integrator as the voltage across a capacitor is the first time integral of current flowing through it and so SOC is determined by Equation 2.39 (Seaman et al., 2014).

$$SOC(t) = SOC(t_0) + \frac{1}{C_N}\int_{t_0}^{t} I_{Batt}(\tau)d\tau \qquad \text{Equation 2.39}$$

In the above, $SOC(t)$ is the state of charge after a time period t where 1 is a fully charged battery and 0 is an empty battery. The initial state of charge is taken at time, t_0 and I_{Batt} is the net current flowing through the battery at time instant τ.

The circuit on the right contains traditional RC pairs from Thėvenin based models to simulate the dynamic voltage response of the cell. The circuit uses a variable voltage source as the OCV, V_{OC} to represent the change in V_{OC} as a function of SOC. The value of current flowing through the battery, I_{Batt} is used to set the current in the battery lifetime circuit through the variable current source. This current source can charge or discharge the capacitor such that SOC changes dynamically which in turn changes the OCV in the voltage response circuit (Min & Rincon-Mora, 2006). If two RC pairs are used to characterise the transient voltage response, $R_{Trans,S}$, $C_{Trans,S}$, $R_{Trans,L}$ and $C_{Trans,L}$ are used to capture the short and long-time constants as shown Figure 2.33.

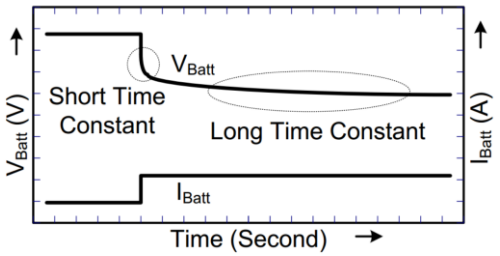

Figure 2.33. Transient response to a step current (Min & Rincon-Mora, 2006).

Battery run-time is the time when V_{Batt} reaches the end-of-discharge voltage, V_{min} and not when $C_{Capacity}$ reaches 0 V. This is because $C_{Capacity}$ does not take into account the loss of energy caused by the internal resistance of the cell. Once the end-of-discharge voltage is reached some charge will be left in the capacity which will indicate this loss of energy.

The model presented by Min and Rincon-Mora (2006) does not fully take into account the reduction in usable capacity as discharge current is increased as shown in Figure 2.30. Although the model does consider the energy loss through the resistance of the cell which increases with current, further losses are incurred due to an increase in the rate of unwanted side reactions which cause a further drop in the usable capacity of the cell (Min & Rincon-Mora, 2006). Kroeze and Krein (2008) propose adding a rate factor, $f_3\,(current)$ to Equation 2.38 to overcome this shortcoming.

$R_{Self-discharge}$ is in place to model the loss of battery capacity while no current is being drawn from the cell. This effect is typically ignored in EV applications as the vehicles are frequently recharged and li-ion batteries have very low self-discharge (Seaman et al., 2014).

All the parameters presented in Figure 2.32 are in fact multivariable functions of SOC, temperature, cycle life and current (Min & Rincon-Mora, 2006). Also, although ignored by Min and Rincon-Mora (2006), each parameter has a different value when the battery is being charged and when the battery is being discharged (Kroeze & Krein, 2008). Some of these dependencies can be ignored under certain conditions. The effect of cycle life can be ignored when analysing the energy efficiency of an EV in its new state and not throughout its service life. Temperature can be ignored when thermal management systems are in place to maintain battery temperature and when discharge currents are kept relatively low (Min & Rincon-Mora, 2006).

The dependency on SOC and current however cannot be ignored as SOC and current will vary throughout any run-time simulation. Min and Rincon-Mora (2006) tested the effect of SOC and discharge current on OCV and the parameters of the RC networks. The results are shown in Figure 2.34 and show that the RC parameters are mostly independent of SOC between 20 to 100 % SOC and vary exponentially between 0 to 20 % SOC. The discharge current however has little effect on model parameters.

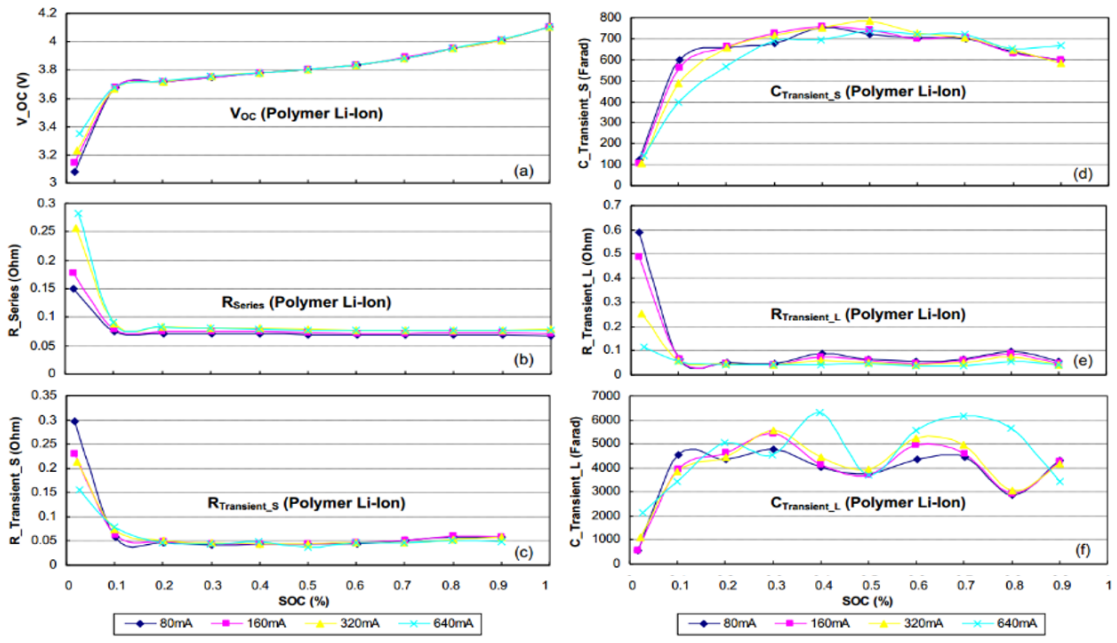

Figure 2.34. Extracted parameters of a lithium polymer cell at room temperature (Min & Rincon-Mora, 2006).

Min and Rincon-Mora (2006) tested the accuracy of the proposed run-time model by comparing the simulated response of polymer li-ion cells to experimental data from the same cell under the same load profile and operating conditions. It was found that the maximum predicted voltage error was 30 mV and the maximum runtime error was 0.4 % (Min & Rincon-Mora, 2006). Figure 2.35 shows the simulated voltage response to periodic four step discharge overlaid on experimental data from the same test.

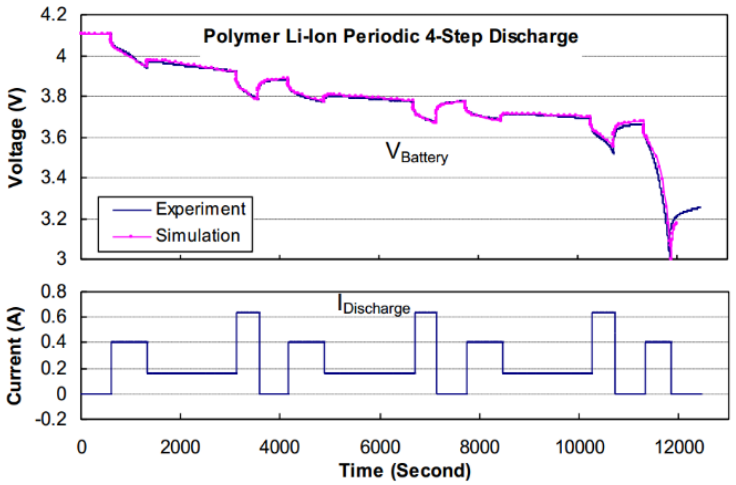

Figure 2.35. Comparison of simulation data and experimental data for a periodic 4 step discharge (Min & Rincon-Mora, 2006).

2.9.4.4 Parameter extraction

The structure of the chosen model largely depends on the parameters that can be calculated from data sheet values or that can be extracted experimentally (Seaman et al., 2014). Petricca et al. (2013) analyse various datasheets from various battery manufacturers with the aim of automatically selecting and generating a model based on available data. As some manufactures provide more data than others, the accuracy of the model ultimately depends on the data available. Most data sheets contain voltage versus SOC plots for a range of discharge currents and these curves can be used to calculate R_{Series} (Petricca et al., 2013).

In order to model the dynamic behaviour of batteries due to the recovery effect, a discharge curve for a pulsed discharge current is required, as shown in Figure 2.36. Three regions can be observed, the instantaneous voltage drop, V_R, a short-time effect voltage drop, V_S and a long-time effect voltage drop, V_L. The instantaneous voltage drop is characterised by a resistor, R_{Series} and the short and long-time effect dynamics are characterised by the RC pairs, $R_{Trans,S}$, $C_{Trans,S}$ and $R_{Trans,L}$, $C_{Trans,L}$ respectively. A tangent line, t_s is drawn at the beginning of the short-time effect curve. The time constant τ_S is taken as the intersection of the asymptote s and the line t_s. The end

of the short-time region is defined as $5 \cdot \tau_S$ after the instantaneous voltage drop and is used to define V_S. The values of the short-time effect can then be calculated from Equation 2.40 and Equation 2.41 (Petricca et al., 2013).

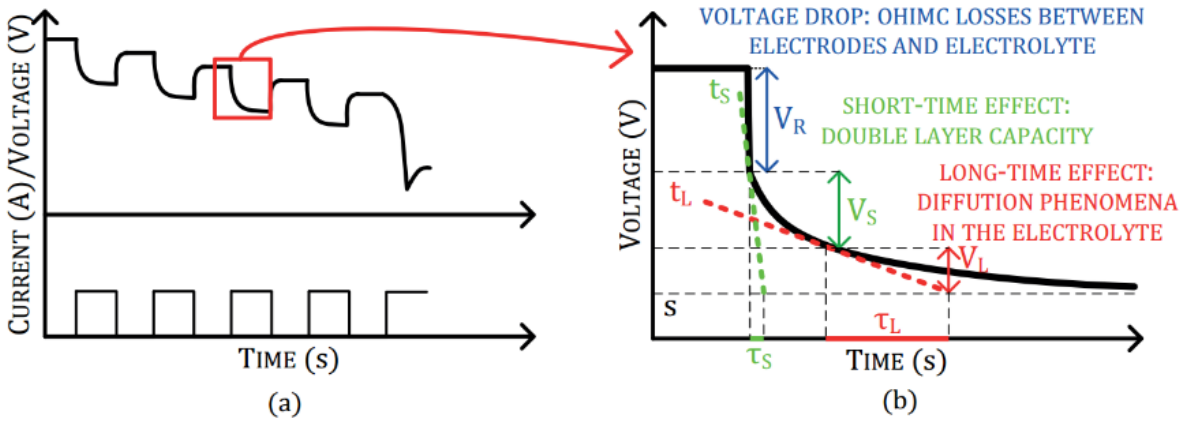

Figure 2.36. (a) Discharge curve for a pulsed current train and (b) extraction of RC parameters (Petricca et al., 2013).

$$R_{Trans,S} = \frac{V_S}{I_{Batt}} \qquad \text{Equation 2.40}$$

$$C_{Trans,S} = \frac{\tau_S}{R_{Trans,S}} \qquad \text{Equation 2.41}$$

The long-time effect region begins at the end of the short-time effect region and a tangent line, t_L is generated at this point. The time τ_L is taken as the time from the beginning of the long-time effect region to the intersection of t_L and the asymptote s. The values of the long-time effect can then be calculated from Equation 2.42 and Equation 2.43 (Petricca et al., 2013).

$$R_{Trans,L} = \frac{V_L}{I_{Batt}} \qquad \text{Equation 2.42}$$

$$C_{Trans,L} = \frac{\tau_L}{R_{Trans,L}} \qquad \text{Equation 2.43}$$

The model also requires the generation of an OCV function based on the SOC of the battery, $V_{OC}(SOC)$. A least squares approximation can be used to create a function from an OCV versus SOC polynomial curve up to the sixth order as shown in Equation 2.44 (Kroeze & Krein, 2008). Figure 2.37 shows an example of an OCV versus SOC curve as well as the voltage response of a 1C charge and 1C discharge. The C-rate of a battery is defined as the discharge current divided

by the theoretical current draw which would result in a one hour discharge (Battery University, 2017).

$$V_{OC}(SOC) = a0 + a1 \times SOC + a2xSOC^2 \ldots \quad \text{Equation 2.44}$$

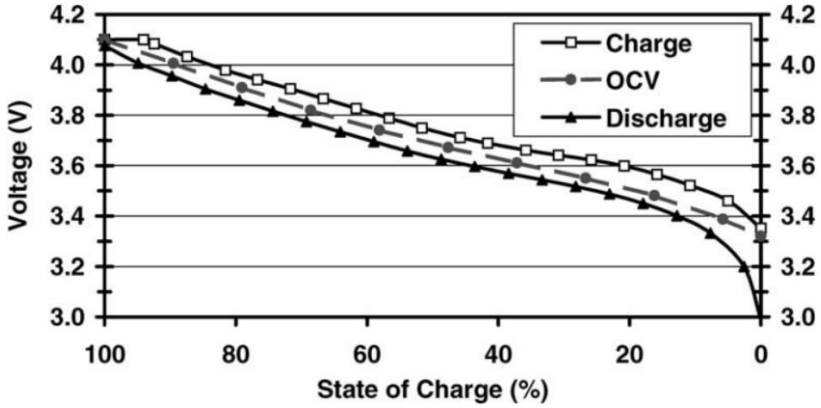

Figure 2.37. Voltage response of a li-ion cell with a 1C charge and discharge current (Nelson, Bloom, Amine, & Henriksen, 2002).

2.10 Auxiliary systems

While all major system losses have been discussed, auxiliary electrical loads must also be considered for a complete energy analysis of an EV. An EVs battery pack is largely responsible for powering a high voltage traction motor which enables vehicle motion. This same battery pack is also required to power a low voltage auxiliary system which can account for 15 % or more of vehicles energy consumption (Vražić, Barić, & Virtic, 2014). This auxiliary system is responsible for both essential systems such as cooling and heating of the battery pack and traction motor as well as non-essential luxury systems such as electric windows, mirrors and infotainment systems. Power to the low voltage system is typically provided by a DC/DC buck convertor which steps down the high voltage of the battery pack to 12 V.

Some of the auxiliary systems have a minor impact on energy consumption of the entire vehicle however other systems, especially heating and air conditioning can significantly increase overall energy consumption of the vehicle (Fiori et al., 2016). The total auxiliary power consumption comprises a base load from components in constant use and a peak load from components which are used in certain circumstances, such as the use of turning signals.

2.10.1 Heating, ventilation and cooling (HVAC)

2.10.1.1 Cabin

Cabin air conditioning and heating systems are commonly present in electric vehicles to ensure driver comfort. Heating, which is traditionally sourced from excess heat produced by an IC engine, must be provided electrically in EVs using energy from the battery. Electric heaters can be powered by the high voltage or low voltage auxiliary system and can draw up to 4 kW depending on operating demands (Randall, 2006). The air conditioning system uses a 3 kW to 5 kW electric compressor and is also powered by either the high voltage or low voltage system.

Figure 2.38 shows the auxiliary power load at various ambient temperatures as measured on 7375 Nissan Leaf vehicles. The auxiliary power demand considers the cabin heater and fan, battery heater, headlights, power steering, radio etc. (Allen, 2014). It can be seen that there is increase in energy consumption the further the ambient temperature increases or decreases beyond the "comfortable temperature range" of 60 to 75°F (15 to 24°C) (Allen, 2014).

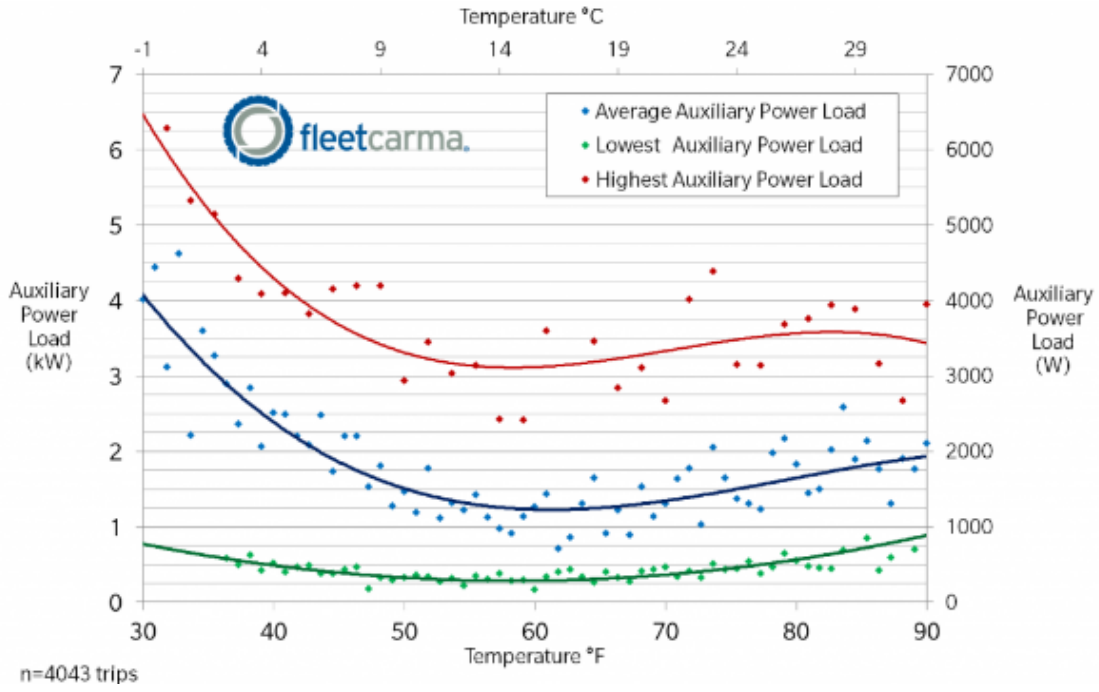

Figure 2.38. Auxiliary power consumption of the Chevrolet Volt versus ambient temperature (Allen, 2014).

2.10.1.2 Battery

EVs are typically powered by li-ion battery packs which must be operated within a certain temperature range to prevent reduced cycle life and reduced charge and discharge performance. Heating is critical during low temperature charging as li-ion cells cannot be charged below 0°C.

Cooling is typically required during peak power discharge and to reduce the rapid cycle life capacity fade li-ion cells experience at higher temperatures.

2.10.1.3 Motor cooling

Traction motors can also be cooled to increase the peak output power of the motor and to increase the longevity of the motor (Karim & Yusoff, 2014). Cooling can be achieved through forced air cooling or through a liquid cooling system. Forced air cooling systems typically consist of a fan attached to the output shaft of the motor which will draw power from the battery, although not directly, through an increased load on the motor. A liquid cooling system however requires power for pumps to circulate the coolant through a cooling system, and radiator fans.

2.10.2 Lighting

Lighting can be split into two categories, internal lighting and exterior lighting. Exterior lighting includes turn signal lights, head lights (low and high beam), side markers, stop lights, tail lights, reverse light/s and a number plate light. Some cars may also be fitted with daytime running lights which are only active during the day. LED lighting can be used to significantly decrease the power consumption of the entire lighting system (Vražić et al., 2014). Certain lights are only required at night, during the day or during both day and night and only at certain intervals, for example indicators are powered for an average of 50 s per trip (Vražić et al., 2014).

2.10.3 Miscellaneous electronics

Various other electrical systems consume power from the auxiliary system. These systems include electric windows, instrumentation, entertainment/sound system, electric mirrors and seats, battery management systems, motor controllers, windscreen wipers, relays, contactors, hooter, power steering and brake vacuum pump. The power consumption of these components can be relatively easily determined from manufacturer's datasheets, for example power steering can consume 2 – 3 kW (Vražić et al., 2014).

2.10.4 DC/DC efficiency

Most auxiliary loads will be powered through the DC/DC convertor which also has an associated energy loss. DC/DC convertors used in EVs are switch mode buck convertors which use power electronics to step down voltage. Typical peak efficiency of these convertors is greater than 90 % at rated load however efficiency drops as the power output of the converter decreases (Keeping, 2013).

2.11 Drive cycles

Drive cycles have been developed for a number of different purposes but ultimately their aim is to represent real-world driving conditions as a velocity-time profile. This velocity time profile can then be used to simulate driving conditions on a laboratory chassis dynamometer or through a computer model (Brady & O'Mahony, 2016). Various different drive cycles exist which are intended to represent different driving conditions such as urban driving, sub-urban driving or highway driving. Standard drive cycles can be used for the following purposes (Brady & O'Mahony, 2016):

1. Assist in understanding the requirements of the vehicle's powertrain
2. Provide standard measurement procedures for the fuel or energy consumption of vehicles
3. Assist in analysing EVs impact on the electricity grid
4. Analysing a vehicle's lifecycle

Two types of drive cycles can be identified, transient cycles which have a wide range of velocities and accelerations and modal cycles which have periods of constant acceleration and velocity (Brady & O'Mahony, 2016). Two categories of drive cycles also exist, drive cycles used for legislative purposes and those used for non-legislative purposes (Brady & O'Mahony, 2016). Legislative drive cycles such as the New European Drive Cycle (NEDC) and the Federal Test Procedure 75 (FTP-75) are used to certify that new vehicles comply to emission and fuel consumption limits within their jurisdictions (Brady & O'Mahony, 2016). Non-legislative cycles can be used for other purposes such as vehicle design, for example the Athens cycle (Tzirakis, Pitsas, Zannikos, & Stournas, 2006).

Many drive cycles, especially modal cycles, used for legislative purposes, are good for comparison purposes however they have been found to have very little accuracy in comparison to real-world driving conditions (Brady & O'Mahony, 2016). Tzirakis et al. (2006) found that fuel consumption values tested with the NEDC cycle varied 7 to 79 % from real-world driving conditions and emissions were reported to be up to 300 % higher.

2.11.1 New European Drive Cycle (NEDC)

The NEDC test is a legislative cycle used in Europe to measure the emissions and fuel consumption of vehicles on a laboratory dynamometer (Fiori et al., 2016). The cycle runs for 1180 s over an equivalent 11 km route with an average speed of 33.6 km/h and is conducted in a 20 to 30°C environment with a simulated wind and inertial load (Genikomsakis & Mitrentsis, 2017). The cycle, as shown in Figure 2.39 consists of four ECE-15 low speed urban cycles

followed by a single highway driving cycle (Genikomsakis & Mitrentsis, 2017). The cycle is however a stylised cycle and is not indicative of real-world driving conditions.

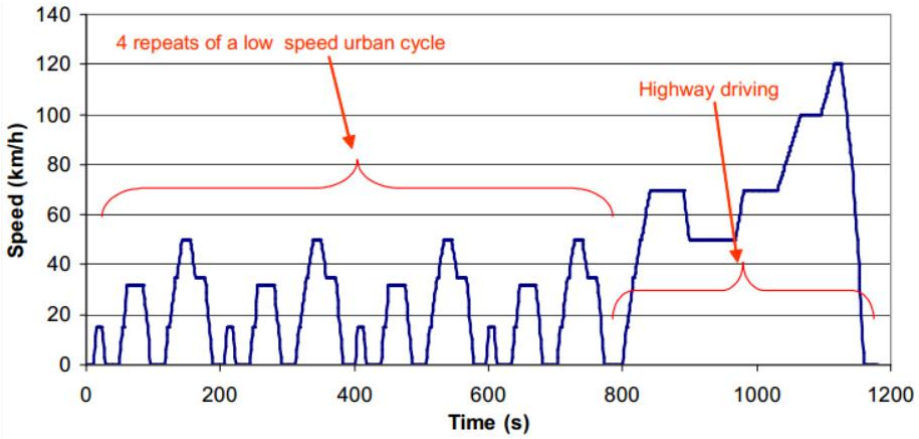

Figure 2.39. NEDC drive cycle (Barlow, Latham, McCrae, & Boutler, 2009).

2.11.2 Environmental Protection Agency (EPA) cycles

The EPA is a legislative body in the United States which defines various legislative drive cycles. Two Federal Test Procedure (FTP) cycles are defined, the FTP-72 and the FTP-75, shown in Figure 2.40 (Barlow et al., 2009). The FTP-72 cycle, also known as the Urban Dynamometer Driving Schedule (UDDS) is 1874 s in duration and covers 17.8 km with an average speed of 34.2 km/h. This cycle represents city driving conditions with frequent stops. The Highway Fuel Economy Test (HWFET) was designed to represent highway driving conditions over a 16.6 km route with an average speed of 77.7 km/h (Barlow et al., 2009).

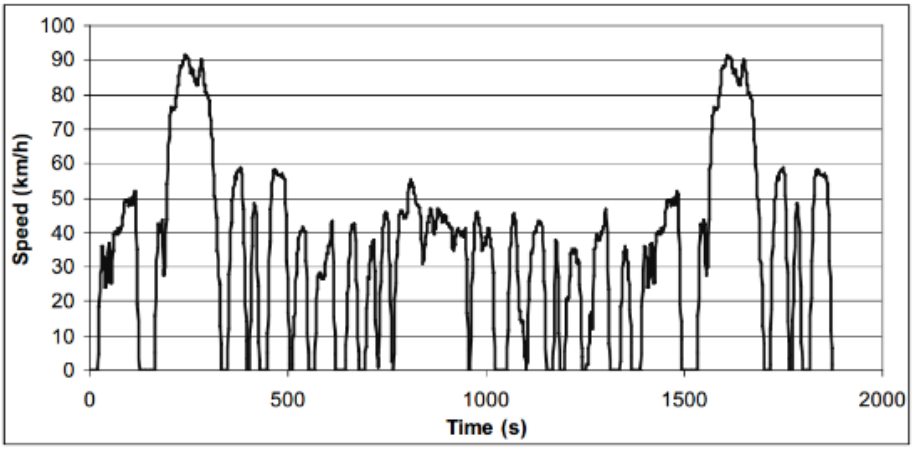

Figure 2.40. FTP-75 drive cycle (Barlow et al., 2009).

2.11.3 Electric vehicle cycles

As EV drive cycles have only recently been developed, EV manufacturers have relied on existing IC vehicle drive cycles to test the range of EVs under laboratory conditions (Brady & O'Mahony, 2016). This is problematic as these drive cycles were developed for IC vehicles which have inherently different performance characteristics to EVs (Brady & O'Mahony, 2016). For instance, torque in an IC vehicle is not delivered instantly but only within a defined power band range where an electric motor can provide maximum torque immediately.

2.11.3.1 Dublin Drive Cycle

Brady and O'Mahony (2016) have developed a drive cycle based on real-world data extracted from a large number of EVs being used in Dublin over a six month period. This data was processed and synthesised to form the cycle shown in Figure 2.41. The accuracy of the cycle was measured by comparing some key statistics of the drive cycle against the same statistics from the real-world data. It was found that the Dublin City Drive cycle varied by 4 % from the real-world data. Other legislative drive cycles were also compared to the data and the FTP-75 and NEDC cycles differed by 8 % and 66 % respectively (Brady & O'Mahony, 2016).

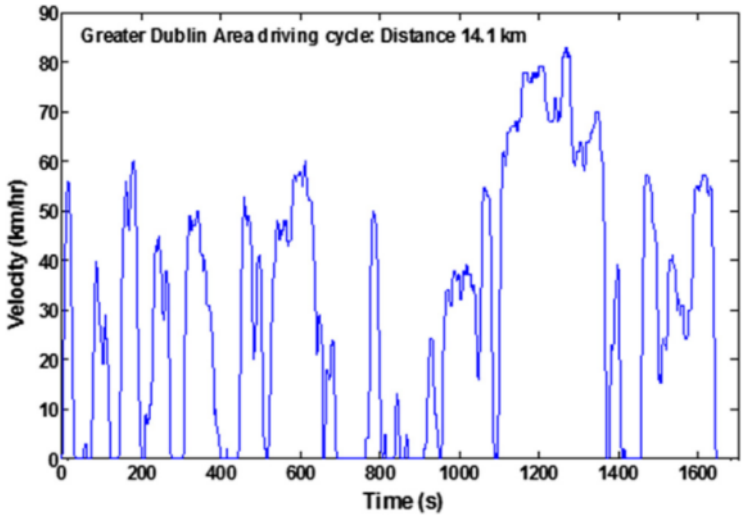

Figure 2.41. Dublin drive cycle (Brady & O'Mahony, 2016).

2.11.3.2 World-Harmonised Light Duty Vehicles Test Procedure (WLTP)

In 2009, the United Nation's World Forum for Harmonization of Vehicles Regulations (WP.29) proposed a roadmap for the development of a worldwide harmonised drive cycle which accurately represents real-world driving conditions (International Council on Clean Transportation, 2013).

The harmonised system will have many advantages such as (International Council on Clean Transportation, 2013):

1. Vehicle manufacturers will only be required to test a model under one set of conditions reducing testing time and cost
2. The results of the drive cycle will be more indicative of actual driving conditions allowing consumers to make more informed decisions
3. The test prevents manufacturer's proposed energy reduction strategies from being effective only under drive-cycle conditions and not real-world driving conditions
4. The results will be comparable on a global scale

The proposed cycle was developed from more than 765 000 km of driving data from a broad range of vehicle types, driving conditions and road types (International Council on Clean Transportation, 2013). Three different cycles were developed based on the vehicle's maximum speed and power-to-mass ratio such that the acceleration and speed of the cycle will not exceed the vehicle's capability. Each cycle consists of four distinct speed phases; low, medium, high and extra-high, as seen in Figure 2.42, which shows the cycle for the highest speed and power class, a class 3 vehicle (International Council on Clean Transportation, 2013).

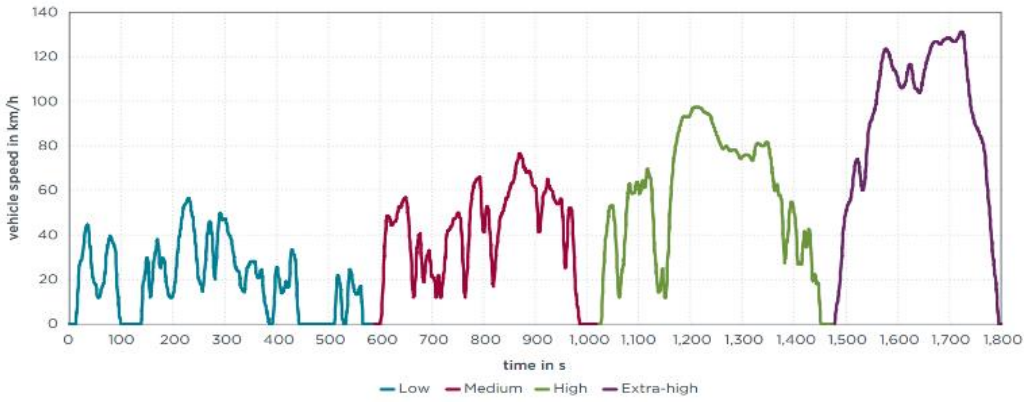

Figure 2.42. WLTP drive cycle for a Class 3 vehicle (International Council on Clean Transportation, 2013).

After testing the proposed cycle in laboratories throughout the world, the consensus is that the new cycle accurately represents real-world driving conditions and can be easily simulated on existing dynamometer platforms (International Council on Clean Transportation, 2013). EVs introduced to the market after September 2017 will be required to publish vehicle driving range based on this new cycle (as well as existing cycles such as FTP-75) and from September 2018 it will be required for all new vehicles sold (Cunningham, 2017).

The WLTP is also unique in that it has provisions for electrified vehicles which are differentiated from IC vehicle's testing methods. The term "electrified" vehicles covers not only pure BEVs but also vehicles containing both electric drivetrains and IC such as hybrid EVs. The testing procedure defines the range and the energy/fuel consumption under charge depletion and charge sustaining modes (International Council on Clean Transportation, 2013). For BEVs only the charge depletion mode is applicable.

All electric vehicles are considered class 3 vehicles regardless of the power-to-mass ratio of the vehicle (United Nations, 2015). The class 3 drive cycle is separated into two subcategories, class 3-1 for vehicles with a top speed of 120 km/h and class 3-2 where the top speed exceeds 120 km/h (United Nations, 2015). A city cycle variation of the standard cycle is also available where the vehicle is tested only with the low and medium phases of the full cycle (United Nations, 2015). When testing the range of an EV, consecutive cycles are implemented until the break-off criterion is reached. The break-off criterion is defined as when the actual speed of the vehicle differs from the reference speed by 2 km/h or more within a one second step (United Nations, 2015). If four or more consecutive cycles are required because the range of the EV exceeds the distance of four cycles, a shortened test procedure may be implemented (United Nations, 2015).

The shortened test procedure consists of two dynamic sections, DS_1 and DS_2 and two constant speed sections, CSS_M and CSS_E as shown in Figure 2.43. The dynamic sections comprise a standard WLTP cycle followed by the city cycle version and the constant speed sections simulate a constant speed of 80 km/h (United Nations, 2015). The duration of CSS_E must be set such that 10 % or less of the battery energy is available at the beginning of the CSS_E section and the duration of CSS_M must be set to make up the balance of the full range of the EV (United Nations, 2015). This requires an estimation of the EV range before simulations are run and may require an iterative process of selecting the length of the constant speed sections.

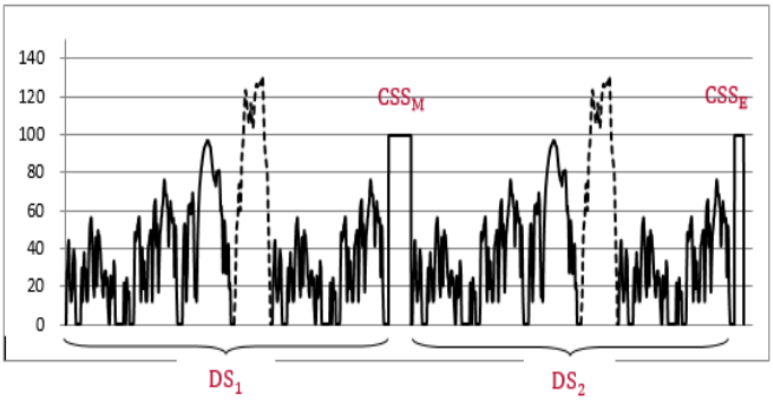

Figure 2.43. Shortened WLTP drive cycle (United Nations, 2015).

2.12 Chapter summary

A thorough investigation of the literature pertaining to EV modelling was presented in this chapter. EV modelling and its implementation was first considered in a broad sense followed by an analysis of each energy loss mechanism experienced by EVs. A critical analysis of the modelling techniques and equations for each loss mechanism was detailed including the accuracy and limitations of the available modelling approaches. Lastly, an investigation into standardised drive cycles was carried out. The findings of the survey will be used to develop a complete energy model of an EV in the following chapter.

CHAPTER 3: MODEL DESIGN

The development of a dynamic, physics based EV model is discussed in this chapter using the insights gained from the literature survey conducted. A graphical physical network modelling tool, Simscape™, is used to build and simulate the model numerically. The chapter begins with an overview of the model's aims and its high level design approach and assumptions leading into a motivation for the selection of Simscape™ as a modelling tool. An overview of the complete system is presented before discussing the development of custom Simscape™ component blocks coded using the Simscape™ coding language as well as composite blocks built using standard Simscape™ libraries. A model of the Mamba EV is then presented using the blocks developed and the parameters for the Mamba are discussed as well as the simulation settings used.

3.1 Modelling aims

The aims and objectives of the model developed in this work have already been presented in Section 1.3. The primary aim of the energy model is to fully understand and quantify the mechanisms of energy losses within the vehicle and to attempt to mitigate these losses through energy reduction strategies and component selection. In order to meet these objectives, the following should be considered in the construction of the model:

1. The range of the vehicle, according to standard drive cycles. This will be used to quantitatively assess the energy efficiency of the vehicle.
2. In order to assess different components during the selection process, it is important that the model is built based on parameters commonly published in manufacturer's data sheets or non-proprietary data which may be requested from manufactures. Consequently, a model which relies on empirical data or experimental analysis of component parameters should be avoided.
3. The developed model will be used to simulate the architecture of the Mamba EV, however care must be taken to ensure the model is as universal as possible, such that a variety of topologies and components can be tested in keeping with the aim of energy optimisation through iteration.

3.2 Simscape™

In order to model and simulate an electric vehicle using a dynamic approach, a modelling tool is required which is capable of numerically solving the system of ODEs used to represent the system. Graphical programming environments can be used to not only solve this system of

equations but also to generate the global set of equations based on smaller sub sections of the entire system. In graphical modelling, this is achieved by using a set of blocks and signals where a block defines the governing equations and signals are used to transfer variables between blocks. Blocks are therefore connected together in a "drag-and-drop" approach in order to form a schematic which models an entire system.

A graphical modelling approach allows large and complex systems, with many different components across multiple physical domains, such as electric vehicles, to be efficiently modelled and simulated. This approach also allows the model designer to quickly and easily reconfigure the model or improve sections of the model in future iterations. Such software should also allow for graphical presentation, manipulation and post-processing of simulation results.

Simscape™ is a toolbox in Simulink™, the graphical modelling tool in MATLAB™, which uses a graphical modelling approach focused on modelling physical systems. It was selected to build the model due to this adaptation to physical modelling which provides many useful features to the model designer. Such features include the automatic handling of units, pre-defined physical domains and the ability to generate custom components.

3.2.1 Custom components

Simscape™ has a variety of standard blocks across many different physical domains. Although some of these blocks were useful in the development of the model, they were not sufficient to model the EV and they do not allow for a bi-directional model that can simulate regenerative braking. Therefore custom blocks were written using the Simscape™ text-based programming language which allows users to develop custom blocks. This allowed full flexibility in the creation of the model in order to optimise the model and ensure that the model met the aims and objectives of this work. This was especially beneficial in ensuring that component models were built using readily available parameters and to set the level of detail of each block to reduce computational cost whilst ensuring model fidelity. The format and language used to build custom blocks was defined in Section 2.3.5.

3.3 Physical network overview

In the graphical modelling approach, the EV is modelled as a set of blocks connected to represent the whole system. The blocks used in the model are presented in Table 3.1, which lists each block, its corresponding physical domain and weather a standard or custom Simscape™ block was used. Figure 3.1 shows a high level schematic of the EV model developed, as well as the flow of energy and data between blocks. Blue coloured blocks indicate the block is a signal block, yellow

indicates the electrical domain, red indicates the mechanical (rotational) domain, orange is a combination of mechanical and electrical and green is the mechanical (translational) domain. Solid blue lines represent bi-directional physical conserving connections and dotted brown lines indicate directional physical signal connections.

Table 3.1. Block domains.

Block	Domain	Type
Motor	Electrical/Mechanical (rotational)	Custom Simscape™
Battery	Electrical	Composite block
Current sensor	Electrical	Standard Simscape™
MPTA Controller	Signal	Custom Simscape™
Inverter	Electrical	Custom Simscape™
Longitudinal Dynamics	Mechanical (translational)	Custom Simscape™
Rotational Dynamics	Mechanical (rotational)	Custom Simscape™
Wheel	Mechanical (rotational)	Standard Simscape™
Driver model	Signal	Composite block

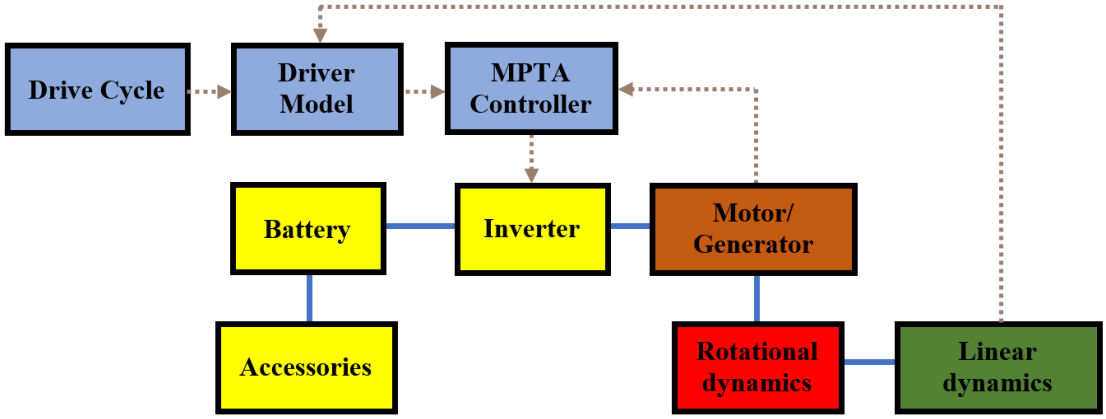

Figure 3.1. High level model schematic.

An electric vehicle is fundamentally a torque controlled system. A driver must set the requested or reference torque value through the accelerator pedal and adjusts this request according to the desired speed, driving conditions and the response of the vehicle. In effect, a driver acts as a proportional-integral-derivative (PID) speed control loop, regulating the speed of the vehicle (Eriksson & Nielson, 2014). This can also be achieved electronically, where the driver requests a

speed and a PID loop is implemented on a microcontroller which computes the torque required to maintain this speed.

The drive cycle block implements a speed versus time curve, where requested speed is fed into the driver model which computes a torque request which is fed into the MTPA controller. The controller computes the required three phase AC voltage to generate the requested motor torque and feeds this gating signal to an inverter. The inverter inverts the DC voltage from the traction battery pack to the requested AC motor voltage. The motor drives the wheels of the vehicle through a drivetrain which transfers the motor torque to the driven wheels and in some cases changes the ratio of torque and speed through a gearbox. During regenerative braking the flow of energy is reversed in order to recover kinetic energy into the battery to slow the vehicle.

The torque at the wheels is transmitted to the road at the contact patch which imparts a linear force on the vehicle. In the event of braking, a negative torque is requested and the motor will act as a generator and current will flow into the battery pack and the speed will decrease accordingly. Two feedback loops exist, a PI controller for the MTPA block and a PID controller for the driver model. As the torque output of the motor is directly proportional to current, the requested torque is converted to a current value in the *dq* reference domain. An inverter acts as a voltage source and therefore the voltage to achieve this desired current must be set using a feedback control loop.

3.4 High level model structure

The possible high level model structures were presented in Section 2.2. The selection of a suitable structure is a crucial step in ensuring the designed model meets the aims and objectives of this work. Selection and motivation of the chosen model structure is discussed in the following subsections.

3.4.1 Modelling approach

Three broad modelling approaches were identified in Section 2.2.3; steady-state modelling, quasi-steady modelling and dynamic modelling. The selection of a suitable approach is important, as it has a strong influence on the fidelity and computational complexity of the model. Although dynamic modelling has the highest computational expense, it was selected as the most suitable approach. Dynamic, physics based modelling was chosen as it offers the highest modelling fidelity and it allows for the vehicle to be effectively modelled based on parameters published by manufactures.

Steady-state modelling is the simplest approach however in the case of electric vehicles, that are characterised by a set of dynamic ODEs, steady-state modelling will provide very little accuracy

and flexibility. Quasi-steady modelling can offer the best of both approaches, with increased model fidelity and reduced computation time, however it is impractical to implement in the vehicle design phase. This is because efficiency maps and look-up tables, which provide energy efficiency over the full operational envelope of the component, are seldom provided by manufactures. Therefore this approach would require an experimental approach to generate this data which is impractical when a designer is required to make a decision based only on data available from the manufacturer. Such an approach also limits the ability to understand the effect on energy efficiency through manipulating fundamental component design parameters.

Although the broad approach considered is dynamic modelling, sub-sections of the model can be implemented as steady-state or quasi-steady sub-models. Approaches can also be taken to reduce computational complexity by simplifying high frequency switching devises such as the motor inverter. Also, the complexity of model design and execution can be greatly simplified through the use of modelling tools based on numerical integration software especially adapted to dynamic physical systems, such as Simscape™.

3.4.2 Direction of calculation

In order to respect physical causality of the model, a feed-forward approach was implemented. This approach requires the inclusion of a driver model which is implemented as a PID controller. Feed-forward modelling provides many advantages, such as HIL implantation and control development and tuning, as discussed in Section 2.2.4. It also provides a true representation of the actual EV as opposed to a backward facing approach which does not respect the physical causality of the system.

3.5 Model assumptions

The assumptions made in order to generate the set of equations used to model an EV will be discussed for each block in the following chapter. However, some general assumptions must first be considered as they will have a strong influence on the selection and implementation of the physical models used.

The model will consider a BEV travelling on a smooth, dry tar road according to a pre-defined speed and elevation versus time profile. A set of parameters will be used to define the vehicle under consideration and the main input to the model will be a speed versus time profile. The primary output of the model will be the distance the vehicle covers, to determine the range of the vehicle.

Although elevation is considered to compute the angle of inclination of the road, the absolute height above sea level will be assumed constant throughout simulations. The ambient temperature will be assumed as nominal temperature and the internal temperature of components will be assumed constant throughout the simulation. Although many parameters are functions of temperature, the internal temperature of components will only increase significantly under high accelerations and decelerations. Therefore the model will be limited to driving profiles which do not consider harsh driving conditions which is in line with the aim of simulating the efficiency of the vehicle under typical driving conditions. Furthermore, some components, such as the motor, battery and motor controller are likely to have thermal management systems in place which regulate the temperature of these components.

3.6 Rotational dynamics

In order to propel the vehicle, the motor applies a tractive torque to the ground through the drivetrain which comprises various components that propagate tractive power from the motor to the driven wheels through rotational motion and vice versa during regenerative braking. The rotational dynamics block considers the dynamics and energy efficiency of all the constituents of the drivetrain in order to compute the torque available at the driven wheels. The block comprises three PC nodes in the mechanical (rotational) domain (indicated by green lines), as shown in Figure 3.2. Node *R* connects to the rotor of the motor, node *C* is the rotational reference node and node *Wh* connects to the wheel block.

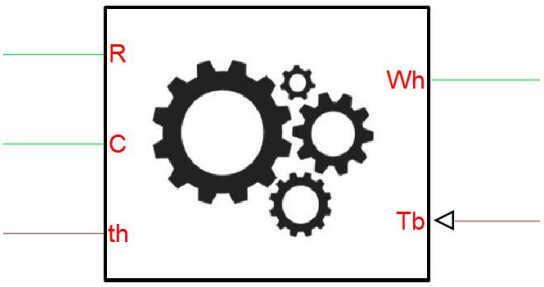

Figure 3.2. Rotational dynamics block.

The code used to build the block using the Simscape™ language is shown Appendix A.1 where each line is numbered for ease of reference. The three PC nodes and their domains are declared in lines 5 to 9. The block also comprises PS inputs (indicated by brown lines), *Tb* which defines the braking torque from the driver block, and a PS output port, *th* which provides rotor angular position to the torque controller. The PS inputs are declared in 25 to 27 and the outputs in lines

29 to 31. The declaration of PC nodes and PS ports follows this same straight forward coding format for all components and therefore will not be discussed for subsequent blocks.

The branch equations shown in lines 45 to 48 defines the positive direction and associated variable for the flow of through variables in relation to the blocks nodes. The flow of torque is separated as a flow from the input to ground and a flow from ground to the output in order to model the relationship between output and input torque due to the gear ratio of the gearbox.

Equation 2.7 is the governing equation for this block as it computes the torque output of the wheel as a function of motor torque considering the efficiency, rotational inertia and gear ratio of each drivetrain component. Equations referenced in this chapter are repeated in Appendix B for ease of reference. The equation considers a drivetrain where torque is transmitted from the motor through a clutch, fixed ratio gearbox, differential, axle shaft and CVJs and finally through the driven wheels. The efficiency of each constituent represents energy lost due to friction and damping and can be modelled as a constant efficiency, as discussed in Section 2.4.

Equation 2.7 is implemented in line 59 for positive motor torque and line 61 for negative motor torque and a conditional if statement is used to switch between the two equations. If the motor torque is negative, the reciprocal of the total drivetrain efficiency must be considered to ensure the inefficiency is remains computed as a loss. Equation 2.8, Equation 2.9 and Equation 2.10 are implemented in line 52, 53 and 54 respectively. Line 63 and 64 integrates the angular speed of the rotor in order to compute its angular position for feedback to the MTPA controller block. The relationship between the motor and wheel speed, defined by Equation 2.6 is realised in line 56.

3.6.1 Assumptions and limitations

Various drivetrain topologies are available, as discussed in Section 2.1.1, depending primarily on how many motors are used and which wheels are driven. Equation 2.7 considers one complete path from the motor to a pair of wheels and with drive shafts of the configuration depicted in Figure 2.2 (a). Figure 2.2 is repeated here as it is referenced multiple times throughout this section.

Although the efficiency, gear ratio and rotational dynamics of the differential are considered, it is assumed the torque is applied to the entire rear axle and not split between the left and right drive shafts and that there is no speed differential between the left and right wheels. Therefore the rotational inertia and efficiency of constituents after the differential should include all the rotational parts. In order to model the drivetrains presented in Figure 2.2 (b) or (c), the efficiency of the clutch can be set to 100 % and the rotational inertia set to zero. Similarly, if any other constituent is not used, such as the absence of a gearbox, the same approach can be taken.

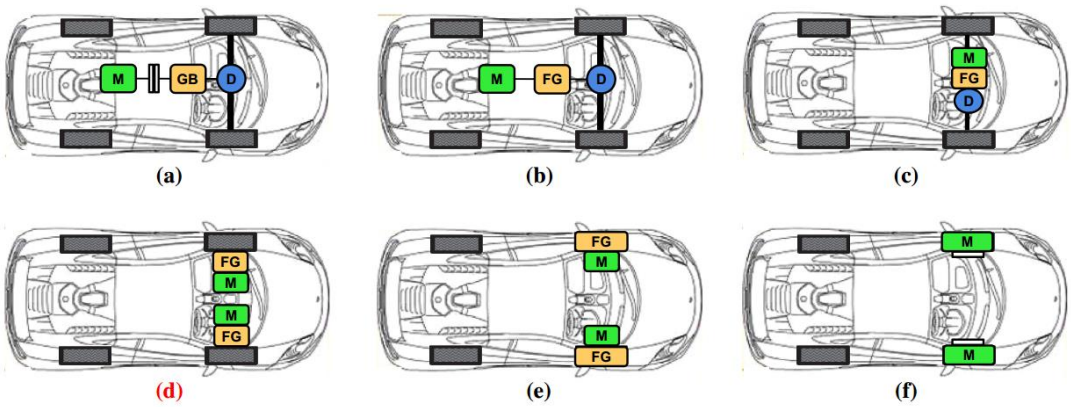

Figure 2.2. Front-wheel drive EV configurations (a) Conventional (b) No transmission, rear mounted motor (c) No transmission (front mounted motor) (d) No differntial (e) In-wheel drive with fixed gearing (f) In-wheel without fixed gearing (Park et al., 2014).

If a two motor configuration is used, such as Figure 2.2 (d), (e) or (f), two motor blocks can be used in the model in conjunction with two rotational dynamics, inverter and MTPA controller blocks. Again, constituents not present in the drivetrain can be ignored using the approach discussed earlier. This approach can be further extended to topologies consisting of four motors for all-wheel drive vehicles. The wheel torque nodes can then be connected in parallel to represent the total wheel torque transmitted to the longitudinal dynamics block.

Constant gear ratios are considered for both the gearbox and the differential. A positive ratio acts to increase torque and consequently decrease rotational speed, as shown by Equation 2.5 and Equation 2.6. In practise, a variable ratio gearbox may be used, in which case both equations remain valid, however the value of G_{gb} must be changed throughout the simulation according to some control strategy which defines gear changes. This may be implemented electronically or it may be a driver input in which case gear selection should be included in the driver model.

3.6.2 Parameter acquisition

A summary of the parameters required for the rotational dynamics block (line 12 to 22) is presented in Table 3.2. The rotational inertia of rotating components may be provided by manufacturers otherwise it can be determined analytically, especially in the case of axle shafts which have a simple geometry. In cases where the geometry is more complex and the geometry and mass distribution of the component is known, a computer aided design (CAD) package can be used to determine the value. The gear ratios of components will also be provided by manufacturers. The efficiency of CVJs is not typically provided however an estimation can be

obtained from the data presented in Section 2.1.1.1. The acquisition of the efficiency of the clutch, differential and gearbox is not within the scope of this work.

Table 3.2. Rotational dynamics block parameters.

Symbol	Description	Unit
J_{as}	Axle shaft rotational inertia	$kg \cdot m^2$
J_{wh}	Wheel rotational inertia	$kg \cdot m^2$
J_{df}	Differential rotational inertia	$kg \cdot m^2$
J_{gb}	Gearbox rotational inertia	$kg \cdot m^2$
G_{gb}	Gearbox ratio	-
G_{df}	Differential ratio	-
η_{df}	Differential efficiency	%
η_{gb}	Gear box efficiency	%
η_{cl}	Clutch efficiency	%
η_{as}	Axle shaft efficiency	%

3.7 Longitudinal dynamics

The longitudinal dynamics block considers the two wheel vehicle model shown in Figure 2.4. The torque applied to the road by the wheels imparts a linear driving force on the vehicle, as described by Equation 2.11, which acts to overcome resistive forces acting against the motion of the vehicle. The block models the resistive forces as a result of aerodynamic drag, rolling resistance, hill-climbing force as well as the dynamic effects due to the inertia of the vehicle.

The block contains two PC nodes in the mechanical translational domain (indicated by dark green lines), node *Fd* which connects to the wheel block and node *G* which is the translational reference node, as shown in Figure 3.3. A standard wheel model block is used from the Simscape™ library which implements Equation 2.11 and converts the rotational torque output of the rotational dynamics block to a linear driving force imparted on the road.

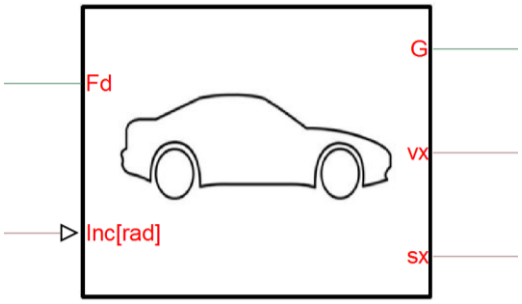

Figure 3.3. Longitudinal dynamics block.

The block's code appears in Appendix A.2. The block comprises one PS input, *Inc* which sets the road inclination and two PS outputs, *vx* and *sx* which output vehicle speed and displacement respectively. The speed of the vehicle is used as a feedback signal for the speed control loop realised in the driver model block. The displacement is calculated by integrating the speed in line 83 and 84 in order to determine the range of the vehicle over the drive cycle.

Equation 2.12, executed in line 79, defines the linear acceleration or deceleration of the vehicle as a function of the driving force and the resistive forces which are summed together in line 81. The hill-climbing force models the energy required to increase the potential energy of the vehicle and can be easily computed using Equation 2.14, implemented in line 66. The computation of aerodynamic drag and rolling resistance involve more complex phenomena which vary on a large number of operating variables and therefore a more detailed discussion is presented in Section 3.7.1 and 3.7.2 respectively.

In the vehicle model shown in Figure 2.4, body roll is considered along the longitudinal axes only and lateral body roll is ignored. Equation 2.15 and Equation 2.16, appearing in line 67 and 68, compute the normal forces on the front and rear wheels respectively and define the lateral weight shift under vehicle acceleration or deceleration. This is an important consideration particularly in cases where different tyres are used on the front and rear wheels, as the rolling resistances forces will be differ as their magnitudes are a function of the normal force acting on the tyre.

The block ignores tyre slip and assumes that all the wheel torque is transferred to the road through the contact patch. Tyre slip is an important consideration when harsh acceleration and braking is modelled and when safety systems to maximise vehicle grip, such as ABS, are to be simulated. Consideration of these phenomena is not within the scope of this work. The energy losses due to suspension are also ignored as it is assumed the vehicle is travelling on a smooth tar road and therefore the losses are negligible, as shown by Figure 2.14.

3.7.1 Rolling resistance

Rolling resistance is represented as a force opposing the motion of the vehicle, acting through the COG. This force is commonly computed using the rolling resistance coefficient measured according to ISO 28580 at a constant speed and tyre pressure, as discussed in Section 2.5.10.2. Equation 2.20 can then be used to approximate the rolling resistance force as a function of tyre load and the rolling resistance coefficient. Although this approach is beneficial for comparison of tyres' energy efficiency, it was found in Section 2.5 that rolling resistance varies with other variables such as speed, temperature and tyre pressure.

A more accurate approach to capture the energy losses would be the use of empirical data from testing carried out by manufacturers according to SAE J2452, discussed in Section 2.5.10.1. Experimental data is fitted to an empirical model (Equation 2.21) which then defines the rolling resistance force in terms of tyre inflation pressure, tyre load and vehicle speed for a particular tyre type. This model does however not take into account the increase in rolling resistance at lower temperatures during tyre warm up as testing is conducted after the tyre has been through a warm up phase, as shown in Figure 2.13.

Equation 2.21 is implemented in line 70 for the front wheels based on the front normal force and in line 71 for the rear wheels based on the rear normal force. As an empirical approximation is used, the units of the equation do not commensurate to a force. Therefore values are converted to a unitless number using the "*value*" expression. The speed is converted to km/h separately in line 69 as it used in multiple locations. The empirical approximation does not produce zero rolling resistance at zero speed which is physically impossible and therefore a conditional if statement is used in lines 72 to 76 to set the total rolling resistance value to zero when vehicle speed is zero.

By using Equation 2.21, temperature is ignored and therefore some error may be introduced. In the case of urban drive cycles, tyre temperature fluctuates about some mean temperature and in the case of highway driving equilibrium is reached after 20-30 minutes (Clark & Dodge, 1979). For urban drive cycles, if nominal temperature is assumed, the rolling resistance force will consider the average temperature and will ignore fluctuations about nominal conditions. During less transient cycles, such as highway driving, the simulated rolling resistance during warm up will be approximately one third lower than the actual value (Clark & Dodge, 1979). The error introduced on a system level will however be small as rolling resistance losses account for a small proportion of losses at higher speeds.

Only tyre deformation is considered in the rolling resistance force as it is the primary mechanism of energy loss in the tyre (Michelin, 2003). Bearing losses are also ignored as the losses are

negligible where high efficiency bearings are used (Michelin, 2003). It is also assumed that the vehicle is driven over a smooth tared surface with no tyre slip. Any aerodynamic losses will be taken into account with the aerodynamic model of the entire vehicle.

3.7.2 Aerodynamic drag

The resistance of the vehicle to move through air can also be expressed as a force opposing vehicle motion, known as aerodynamic drag. Drag can be calculated using a CFD analysis which accounts for actual flow conditions. As it is impractical to compute this value across the operational envelope of the vehicle, Equation 2.23 can be used to compute drag as a function of vehicle speed, wind speed, air density, frontal area and a drag coefficient as shown in line 77. The drag coefficient is computed using CFD at nominal conditions and can be assumed constant across a drive cycle, as discussed in Section 2.7. As wind speed is highly unpredictable it was ignored in Equation 2.23 and it therefore follows that the effect of yaw angle is also ignored. Air density was taken at a nominal value assuming sea level and nominal temperature.

3.7.3 Parameter acquisition

A summary of the parameters (line 6 to line 18) required for the linear dynamics block is presented in Table 3.3. It is assumed the vehicle's bulk geometry, chassis and suspension have been designed and modelled separately from the current model and therefore the chassis mass, the position of the COG and the frontal area of the car are known. The total mass of the vehicle can be computed by summing the masses of the various components used, the chassis mass and the mass of the driver and passengers.

Table 3.3. Linear dynamics block parameters.

Symbol	Description	Unit
m	Vehicle mass	kg
f	Distance from COM to front axle	m
r	Distance from COM to rear axle	m
h	Distance from COM to ground	m
P	Tyre inflation pressure	bar
α, β, a,b,c	SAE J1269 rolling resistance coefficients	-
R_{wh}	Wheel radius	m
ρ_{air}	Air density	$kg \cdot m^{-3}$
C_d	Aerodynamic drag coefficient	-
A_f	Frontal area	m^2

The SAE J1269 rolling resistance parameters can be requested from the tyre manufacturer. If these values are not available, the ISO 28580 value can be used and in a worst case scenario, the value can be estimated using Table 2.3 and the published fuel efficiency class required by legislation. The upper bound of the class should be considered as a conservative estimate. In order to use the ISO 28580 rolling resistance coefficient all the coefficients should be set to zero, except a and β which should be set to the rolling resistance coefficient and 1 respectively.

The tyre pressure should be set within the limits of the tyre set by the vehicle manufacturer. The WLTP testing procedure stipulates that the tyre pressure shall be set to the lower value of the tyre inflation pressure range specified by the vehicle manufacturer (United Nations, 2015).

The aerodynamic drag coefficient can be computed from a CFD analysis. If the geometry of the vehicle differs to the model used for the CFD analysis due to manufacturing differences or minor features, the actual drag coefficient may be higher than the modelled value and it may therefore be necessary to increase the simulated value.

3.8 Motor

The motor block models a non-salient PMSM motor which transforms electrical energy to mechanical rotational energy. The block considers SPM motors with an exterior or interior rotor architecture, operated below the continuous power rating and at speeds below the motor's base speed. The block comprises four nodes in the electrical domain and three nodes in the mechanical translational domain, as shown in Figure 3.4. The three phase power inputs, *u*, *v* and *w* connect to the inverter and *n* is the electrical reference node. Node *R* represents the rotor and connects to the rotational dynamics block and node *C* is the mechanical reference node.

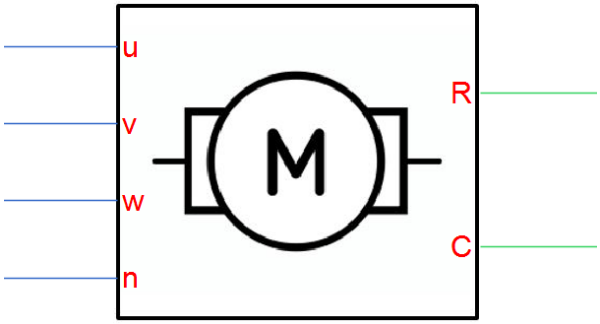

Figure 3.4. Motor block.

The code used to build the block is shown in Appendix A.3. Equation 2.26, Equation 2.27 and Equation 2.28 can be used to model the dynamics of the stator coils in the *dq* reference frame as implemented in lines 68 and 69. As the dynamics are considered in the *dq* reference frame, the phase voltages must be transformed from the *uvw* domain, as shown in lines 64 and 65. The computed *dq* current values must then be transformed back to the *uvw* domain to feed back to the controller block, which is achieved in lines 72 to 74. The zero axis dynamics are considered although in the majority of cases they can be ignored if a balanced three phase load is present and the zero axis inductance is assumed as $L_0 = 0.1 \times L$ (Narkhede, 2016).

The branch equations in line 45 to 47 defines the flow of current according to a three phase wye connection. The direction of positive torque flow from the case of the motor to the rotor is defined in line 48.

The equations used consider copper losses in the stator windings due to the stator resistance however they ignore windage and core losses. These losses can be ignored when the motor is operated at low speeds (at or below base speed) as copper losses are dominant at low speeds. This is shown in Table 2.5 and is further supported by Equation 2.24 which shows the dependency of core losses on motor speed.

If a motor is used beyond its base speed and a field weakening control strategy is implemented, then the core losses must be considered. Core losses can be approximated using Equation 2.24 or a parallel resistance as shown in Figure 2.26. Equation 2.24 is difficult to implement in the design phase of the EV. This is because the coefficients are seldom provided by manufacturers and determination requires experimentation, an analytical approach or finite element field analysis. Experimentation cannot be achieved before the motor is procured and the analytical and finite element field approach requires comprehensive details of the motor geometry and design which is usually proprietary data.

The electromagnetic torque output of the motor can then be computed using Equation 2.29 and the and in the case of non-salient machines, the second term of the equation falls away. Equation 2.31 considers the dynamics of the rotational inertia of the rotor as well as the viscous friction coefficient of the bearing used. These two equations are combined to give the motor torque in line 62. The viscous friction coefficient is often ignored if low friction bearings are used as the losses are negligible.

Motors are rated according to continuous and peak ratings which are dependent on the thermal management system in place. The stator coils can be cooled using liquid cooling channels or using a fan attached to the rotor. If the motor is operated at or below continuous ratings the temperature

of the stator will not exceed the temperature limits of the insulation. In this model, temperature is ignored under the assumption that the motor is operated according to a duty cycle with a peak power below the continuous rating and that a thermal management system is in place. Therefore the nominal ratings of the permanent magnet flux linkage and resistance can be taken as constant values. Also the effects of cross coupling and saturation can be ignored, assuming the motor is not operated in the field weakening region.

3.8.1 Parameter acquisition

The parameters (lines 6 to 11 of Appendix A.3) required for the motor block are presented in Table 3.4. The stator inductance is typically always provided by motor manufactures in either the *dq* reference frame or the *uvw* reference frame. In the case of non-salient motors, such as SPM motors, Equation 2.30 can be used to calculate the *dq* inductances from the line inductance in the *uvw* frame.

Table 3.4. Motor block parameters.

Symbol	Description	Unit
N	Number of pole pairs	-
L_d/L_q	*d*/*q* axis inductance	H
R_s	Phase to neutral resistance	R
λ_f	Flux linkage induced by permanent magnets	Wb
B_m	Viscous friction co-efficient	Nms/rad
J_r	Rotor moment of inertia	kg·m^2

The permanent magnet flux linkage at nominal temperature may be provided by the manufacturers and in cases where the value is not provided, it may calculated for non-salient machines from the commonly published velocity constant K_v [rad/sV] or the torque constant, K_t [Nm/A] using Equation 3.1 or Equation 3.2.

$$K_t = \frac{3N}{2}\lambda_f \qquad \text{Equation 3.1}$$

$$K_v = \frac{1}{N\lambda_f} \qquad \text{Equation 3.2}$$

Rotor inertia must be provided by manufacturers or it can be estimated from a CAD model of the rotor. The viscous friction coefficient can be ignored if a low friction bearing is used or it may be acquired from the bearing or motor manufacture's data sheet. Park et al. (2014) report a viscous friction coefficient of 0.005 Nm/rad/s for a 100 kW PMSM which can be considered negligible, especially if the motor is operated at low speeds.

3.9 MTPA controller

The MTPA block computes the three phase voltage which should be applied to the motor in order to achieve the requested motor torque. The block does not consider any energy losses in the system however it affects the efficiency of the motor over its operational envelope. A MTPA control strategy is considered as it is the most common strategy used by controller manufacturers (Goss et al., 2014). The assumptions of the motor block are assumed here too and therefore the block controls non-salient motors operated below their base speed with no field weakening. The block only processes PS data and uses no PC nodes, as shown in Figure 3.5.

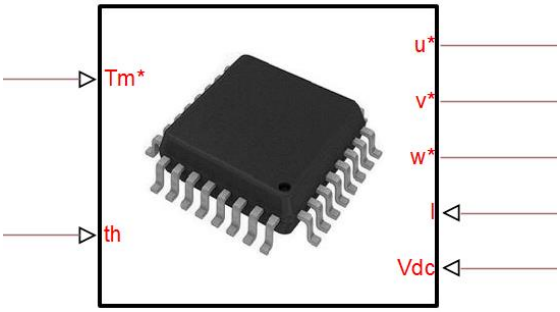

Figure 3.5. MTPA controller.

Four PS inputs are used, per the code appearing in Appendix A.4. The requested motor torque, *Tm** is received from the driver model block, the rotor's angular position, *th* is received from the rotational dynamics block, the voltage of the battery, *Vdc* is received from the battery block and the motor current vector, *I* is received from a current sensor in series between the inverter and motor. The remaining three ports are PS outputs, *u**, *v** and *w** which transmit a request for the correct three phase AC voltage to the inverter block.

The MTPA control strategy is discussed in Section 2.8.5. When a motor is operated below its base speed and core losses can be considered negligible, a MTPA control strategy is the most efficient way to control a PMSM motor (Goss et al., 2014). The control strategy is implemented in the *dq* reference domain in order to simplify calculations. Therefore the feedback currents, measured in the *uvw* domain, must be transformed to the *dq* domain, which is achieved in lines 33 and 34 and

the requested *dq* voltage must then be transformed back the *uvw* domain, per lines 57 to 59. The control strategy and reference frame transformations are depicted in Figure 2.27.

Motor current must be set by varying the voltage applied to the stator coils until the desired current is achieved and therefore a PI control loop must be implemented, as discussed in Section 2.8.5. The value of i_d (demagnetising current component) is set to zero, per line 36. Therefore in order to control motor torque, the value of i_q (torque producing current component) is determined using Equation 2.29 and the requested current is then computed in line 37. The error signal is integrated in lines 46 and 47 and the PI control loop is implemented in lines 39 and 40 in order to compute the required three phase voltage to achieve the requested current.

As discussed in Section 2.8.5, the requested *uvw* voltage is transformed to a gating signal using SVPWM in order to drive the semiconductor switching devices to achieve the required phase voltages. Because the inverter is modelled as an average value inverter, the reference voltage values are not transformed to gating signals but are rather transmitted as actual voltage values. Therefore, in order to respect the voltage limit of the inverter imposed by the relevant PWM strategy, the reference voltages should be limited according to the DC bus voltage which is achieved using a conditional if statement in lines 49 to 55. For SVPWM, the maximum phase voltage realisable from the supplied DC voltage is set in line 42 according to Equation 2.33.

3.9.1 Parameter acquisition

The parameters (lines 6 to 9) required for the MTPA control block are presented in Table 3.5. In order to calculate the requested torque from the requested current, the motor's parameters used in Equation 2.29 are required, as discussed in Section 3.8.1. The PI constants are typically set by the vehicle designer based on the dynamics of the vehicle under consideration and the desired stability and acceleration response of the system or they can be obtained from the motors controller's documentation.

Table 3.5. MTPA control block parameters.

Symbol	Description	Unit
N	Number of motor pole pairs	-
λ_f	Permanent magnet flux linkage	Wb
k_p	Proportional PI constant	-
k_i	Integral PI constant	-

3.10 Inverter

The inverter block is responsible for inverting the DC supply of the battery pack to a three phase AC supply suitable to drive the motor. The inverter is modelled as an average value inverter and therefore it ignores the dynamics of the high frequency switching devices whilst still capturing the associated power losses.

The block comprises five PC nodes in the electrical domain (indicated by blue lines), as shown in Figure 3.6. The *B*+ and *B*- nodes on the DC side connect to the respective nodes of the battery block, and the *u*, *v* and *w* nodes on the AC side of the block, connect to the motor's stator coils. The block also comprises three PS input ports, *u**, *v** and *w** which receive the reference voltage signal from the MTPA controller block. The code used to build the block appears in Appendix A.5.

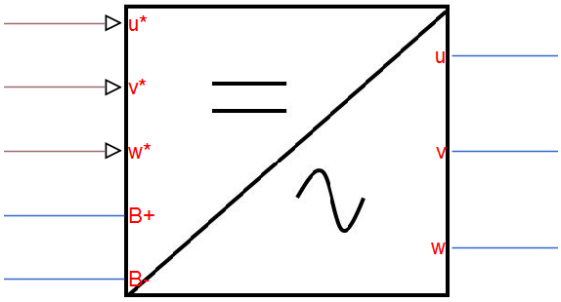

Figure 3.6. Inverter block.

The implementation of an inverter using power electronics is detailed in Section 2.8.5. In order to model the dynamics of the switching devices, a simulation time step of an order of magnitude greater than the switching frequency, typically in the order of 10 kHz (Kelly Controls, 2015), is required in order to capture the switching transients. This will significantly increase the computational complexity of the entire model as the global time step must be reduced to capture the high frequency response. In order to reduce the computational complexity of the model, an average value inverter model is considered. This model ignores the dynamics of the switching devices and considers only the phase voltage limit and the energy losses of the semiconductor devices.

The three phase current flow is defined in the branch equations shown in lines 41 to 43 and the DC current flow in line 40. The three phase voltages on the AC side of the inverter are set to the values requested by the MTPA controller block in lines 49 to 54. The DC power drawn from the battery is then equated to the sum of AC power and the inverter power losses, as shown in line

64. The inverter losses considered are the switching losses and conduction losses as these are the dominant losses in motor drives, as discussed in Section 2.8.5.1.

The switching losses are considered as an average power value which can be scaled from the datasheet using Equation 2.36. A conditional if statement is used in lines 56 to 62 in order to invert the switching power losses when the inverter feeds DC current back into the battery such that they remain computed as losses. The statement also sets the losses to zero when the inverter is not drawing a current and therefore is not in use.

The conduction losses are approximated using Equation 2.34 which uses the equivalent series resistance of the semiconductor device. The resistance of these devices increases with an increase in temperature (Graovac et al., 2006). This effect is not considered as it is assumed that the inverter has a thermal management strategy in place and the heat generated by the inverter will be small as the motor is operated below its continuous power rating.

3.10.1 Parameter acquisition

A summary of the parameters (lines 5 to 8) required for the inverter block is presented in Table 3.6. The inverter block requires the on state resistance of the semiconductor device used. The controller manufacturer may provide this resistance value or the exact model of the MOSFET or IGBT device used in which case the value can be extracted from the device's datasheet. The switching losses can be extracted from the MOSFET or IGBT datasheet and scaled using Equation 2.36 or requested directly from the motor controller manufacturer.

Table 3.6. Inverter block parameters.

Symbol	Description	Unit
R_{on}	On state MOSFET/IGBT resistance	Ω
P_{sw}	Rated switching losses	W

3.11 Battery

The battery block models a li-ion traction pack comprising cells connected in parallel and series using an equivalent circuit, run-time based model. Although electrochemical models are the most accurate, they are difficult to implement and require a large number of parameters which are usually proprietary (Seaman et al., 2014). The developed model assumes that all cells within the pack have equal parameters and therefore no cell balancing is required. A li-ion chemistry was chosen as it the preferred choice for EVs, as discussed in Section 2.9.

The battery block was not developed using the Simscape™ language but rather as a composite block using standard Simscape™ components connected to form an electrical circuit. Some Simulink blocks were also used to process PS data. A mask was then used to create an interface for the sub-model, as shown in Figure 3.7. The sub-model of the battery block is shown in Appendix C.1. The block consists of two PC nodes in the electrical domain which represent the positive and negative terminals of the battery, *B*+ and *B*- respectively. The block also comprises three PS outputs which output the voltage of the battery, *Vdc* to the MPTA controller, the SOC of the battery, *SOC* to the driver model and the battery current, *Ib* to a display block.

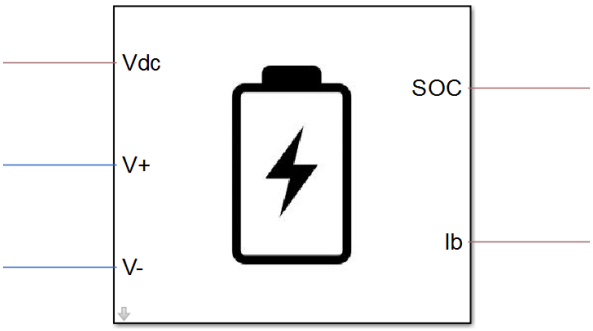

Figure 3.7. Battery block.

The literature used to build this model is presented and discussed in Section 2.9.4.3 and the equivalent circuit topology is shown in Figure 2.32, repeated here for ease of reference. The figure is repeated here as multiple references are made to it in this section. The sub-model was built using the Simscape™ electrical library and components were connected according to the two equivalent circuit topologies presented in Figure 2.32. The OCV is modelled as a variable voltage supply which is set according to the output of a Simulink function block that computes the OCV based on the SOC of the battery obtained from the battery lifetime circuit, using Equation 2.44.

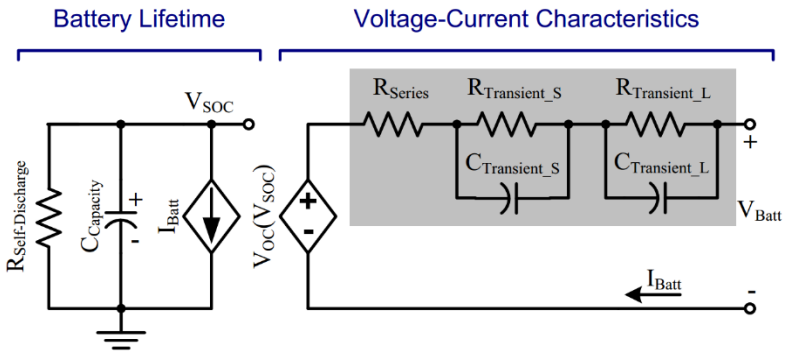

Figure 2.32. Modified run-time based model (Min & Rincon-Mora, 2006).

As discussed in Section 2.9.4.3, the battery run-time is determined when the voltage of the battery reaches the end-of-discharge voltage. The end-of-discharge voltage is dependent on the exact li-ion chemistry used however it may be set to a higher value in order to extend the cycle life of the battery (Muenzela et al., 2015). An assertion block was used to ensure that the battery voltage exceeds the minimum battery voltage specified throughout the simulation. When this criterion fails, the simulation is automatically stopped, indicating the battery is depleted.

3.11.1 Assumptions and limitations

Figure 2.34 shows how the values of the circuit elements vary with discharge current and SOC. The OCV varies over the full SOC range of the battery, but is largely independent of discharge current. The values of the resistors and capacitors remain fairly constant for SOC values above 10 % and do not differ significantly for different discharge values. The value of the long-time effect capacitance varies periodically above a SOC of 10 %. Therefore, an acceptable approach to reduce the complexity of the model whilst maintaining model fidelity, is to assume constant values for the RC pairs and the equivalent series resistance.

Although this could induce significant error from 0 % to 10 % SOC, it will have little effect on the accuracy of the complete solution. Also, the SOC range of li-ion cells is often restricted to exclude low SOC values so as to prolong cell life (Muenzela et al., 2015). It is however important to model the change in OCV with SOC as this relationship will be used to predict voltage during the simulation. In the voltage-current characteristic circuit, more than two RC pairs may be used to increase model fidelity however computational cost is increased. Two RC pairs will be used as literature has shown this to be a good compromise between model fidelity and computational cost for BEVs, as discussed in Section 2.9.4.2.

The usable energy of the battery is modelled using a capacitor in the battery lifetime circuit and the relationship between the capacitance and the usable capacity of the pack is given by Equation 2.38 which includes a cycle and temperature factor. A rate factor should also be included to model the decrease in usable capacity as discharge rate increases, as shown in Figure 2.30. The effect of capacity decay over time will be ignored as this phenomenon does not fall within the aims of the model and therefore the cycle factor is ignored.

If the discharge current from the battery is low and seldom exceeds 1C, temperature can be ignored during the simulation (Barreras, Schaltz, Andreasen, & Minko, 2012). Therefore, the rate and temperature factors are ignored. The effects of self-discharge will also be ignored as this does not have an effect on the energy efficiency of the battery and therefore the capacity is taken as the nominal capacity of a new cell.

The battery under consideration may consist of one or more battery modules connected in a series string to increase the pack voltage, where N_S defines the number of modules in series. Each module may consist of one or more cells connected in parallel to increase the pack capacity, where N_P is the number of cells connected in parallel. Therefore the circuit elements appearing in Figure 2.32 should consider the equivalent values for the entire pack (such that each element is representative of the entire pack). If it is assumed that each cell is identical, the well-known rules for calculating the equivalent resistances and capacitances can be used (Avison, 1989). Equation 3.3 and Equation 3.4 can therefore be easily derived in order to determine the equivalent resistance, R_{eq} and equivalent capacitance, C_{eq} values.

$$R_{eq} = \frac{N_S}{N_P} \cdot R_{cell} \qquad \text{Equation 3.3}$$

$$C_{eq} = \frac{N_P}{N_S} C_{cell} \qquad \text{Equation 3.4}$$

The equivalent OCV voltage, OCV_{eq} is given by Equation 3.5, the equivalent end-of-discharge voltage, $V_{min_{eq}}$ is given by Equation 3.6 and the nominal capacity of the pack, $C_{N_{eq}}$ is given by Equation 3.7.

$$OCV_{eq} = N_S \cdot OCV \qquad \text{Equation 3.5}$$

$$V_{min_{eq}} = N_S \cdot V_{min} \qquad \text{Equation 3.6}$$

$$C_{N_{eq}} = N_P \cdot C_N \qquad \text{Equation 3.7}$$

3.11.2 Parameter acquisition

A summary of the parameters required for the battery block is presented in Table 3.7. The values of the RC pairs are not provided by cell manufacturers however the procedure outlined in Section 2.9.4.4 can be used to determine the values if the voltage response of a cell or pack pulse discharge test is given. The value of the series resistance may be provided on the cell datasheet or it can be determined from a pulse discharge test. The value may also be determined if voltage versus SOC data is given for multiple discharge rates (Petricca et al., 2013).

Table 3.7. Battery block parameters.

Symbol	Description	Unit
R_{Series}	Equivalent series resistance	Ω
$R_{Trans,S}$	Short transient response resistance	Ω
$C_{Trans,S}$	Short transient response capacitance	F
$R_{Trans,L}$	Long transient response resistance	Ω
$C_{Trans,S}$	Long transient response capacitance	F
C_N	Nominal cell capacity	Ah
N_S	Number of cells in series	-
N_P	Number of cells in parallel	-
V_{min}	End-of-discharge voltage	V
a_0, a_1, a_2, a_3	OCV versus SOC equation coefficients	-

The coefficients for the OCV versus SOC equation can be determined using a curve fitting tool such as the MATLAB™ Curve Fitting Toolbox if the cell manufacturer has provided an OCV curve. Alternatively a discharge versus voltage curve with a low C-rate, 0.05C or lower, provides a good estimate of the OCV voltage (Weng, Sun, & Peng, 2014).

The end-of-discharge voltage can be determined by measuring the cell voltage when the battery is depleted or it may be set by the vehicle designer in accordance with the limits set by the cell manufacturer and cycle life requirements.

3.12 Auxiliary load

The auxiliary load block models the electrical loads drawn by the auxiliary system as well as the energy losses of the DC/DC used to stepdown the voltage of the battery pack. The various relevant auxiliary loads have been discussed in Section 2.10. The block comprises two nodes in the electrical domain, *B*+ and *B*- which connect to the battery block, as shown in Figure 3.8. The code used to build the block is presented in Appendix A.6.

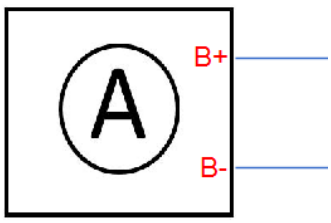

Figure 3.8. Auxiliary load block.

The DC/DC block is modelled under steady-state conditions and considers the average auxiliary power draw. The load is split into components that draw power through the DC/DC, and therefore the DC/DC efficiency is considered for these loads, and high voltage loads that draw power directly from the battery. The efficiency of the DC/DC is assumed as a constant efficiency which is typically greater than 90 % (Keeping, 2013).

Line 29 computes the current drawn from the battery pack and the branch equation in line 22 defines the flow of current from the positive terminal of the block to ground. The efficiency of the DC/DC is considered for the low voltage power draw only. A conditional if statement is employed in lines 28 to 32 in order to delay the power draw from the battery pack to improve simulation stability during initialisation.

With the exception of heating and cooling, the auxiliary load of EVs is typically significantly lower than the tractive power output, especially when steps are taken to reduce the auxiliary load such as the implementation of LED lighting (Vražić et al., 2014). If a full cabin HVAC system is considered it may be necessary to model the compressor dynamically.

3.12.1 Parameter acquisition

The parameters (lines 6 to 8) required for the auxiliary load block are shown in Table 3.8. The low voltage auxiliary power draw can be estimated by summing all constant loads such as normally open contactors, driver displays and instrumentation and adding an estimated average power draw of components that draw auxiliary power periodically. The same approach should be considered for high voltage auxiliary components which draw power directly from the battery pack. The efficiency of the DC/DC can be determined from the manufactures datasheet. The load drawn from the DC/DC should be considered relative to its rated load to consider the decrease in efficiency as this ratio drops, as discussed in Section 2.10.4.

Table 3.8. Auxiliary block parameters.

Symbol	Description	Unit
P_{LV}	Low voltage auxiliary power draw	W
P_{HV}	High voltage auxiliary power draw	W
η_{conv}	DC/DC efficiency	%

3.13 Driver model

The driver model block computes the requested torque in order to achieve the desired speed as set by a pre-defined drive cycle. In order to control the torque to achieve the desired speed, a PID control loop is used which replicates the action of a human driver controlling the speed of the vehicle through the accelerator pedal. The block comprises a sub-model built using Simulink components, shown in Appendix C.2, as well as a torque limiter block built in Simscape™, shown in Appendix A.7. A mask was used to create an interface for the sub-model, which appears in Figure 3.9.

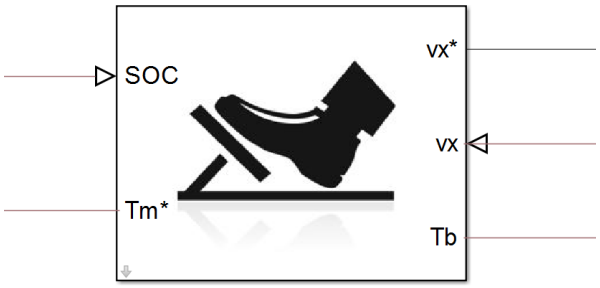

Figure 3.9. Driver model block.

A look-up table outputs the requested speed throughout the simulation based on a predefined drive cycle. A number of relevant drive cycles are presented in Section 2.11. The block receives the simulation time as an input and uses linear interpolation to compute the requested speed at each time step. The actual vehicle speed, received from the linear dynamics block, is then subtracted from the speed request to generate an error signal which is fed into a Simulink PID block.

The PID block outputs a requested torque value to the torque limiter block based on the PID constants. The outputs of the PID block are saturated according to the maximum motor torque such that the torque request does not exceed the limits of the physical system. It is assumed that the absolute value of the maximum motor torque applies to positive and negative torque values. The torque limiter block limits the torque request output based on vehicle speed and battery SOC and will be discussed further in Section 3.13.1. A positive torque request implies a positive tractive force to accelerate the vehicle and a negative torque request implies a braking force to decelerate the vehicle.

If a drive cycle which includes road inclination is implemented, the look-up table data should be extended to include the road gradient at each time step which can be outputted to the inclination port of the linear dynamics block. It may also be necessary to implement a gear changing

algorithm which defines gear changes when a variable speed gear box is used, as discussed in Section 3.6.1.

3.13.1 Torque limiter

The torque limiter block receives the requested reference torque from the PID loop and outputs a requested torque to the MTPA controller after applying limits to the signal based on the speed of the vehicle and SOC of the battery. The torque output of the PID loop is saturated according to the maximum motor and regenerative torques however further limitations must be applied based on the speed of the vehicle and SOC of the battery.

The block comprises three PS inputs, *SOC* which receives the SOC of the battery, *vx* which receives the speed of the vehicle and *Tm_r* which receives the requested torque reference signal from the PID block. The block also comprises two outputs, *Tm** which outputs the positive or negative reference torque to the MTPA controller block and *Tb* which output the mechanical braking torque to the rotational dynamics block, as shown in Figure 3.10. The code used to build the block appears in Appendix A.7.

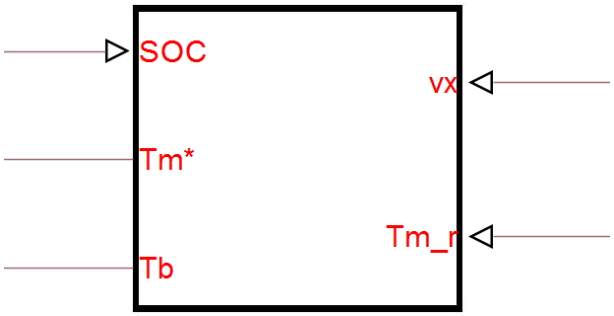

Figure 3.10. Torque limiter block.

In cases when the speed of the vehicle needs to be reduced, a negative torque value is required to reduce the speed of the vehicle. If the negative torque request is fed to the MTPA controller block, the motor will act as a generator and the direction of the current will change such that the battery is charged. This effect is known as regenerative braking. If the negative torque request is fed to the rotational dynamics block, a negative torque is applied to the drivetrain such that no energy is recovered. This is representative of the mechanical braking system in a vehicle where the kinetic energy of the vehicle is lost as waste heat (Guzzella & Sciarretta, 2013).

In both cases a negative braking torque acts to resist the motion of the vehicle and therefore a negative torque may only be requested when the speed of the vehicle is above zero. In reality the electric vehicle can achieve negative speeds by reversing the direction of electrical commutation

of the motor, however this effect is not modelled. During regenerative braking the battery acts as an energy sink in order to recover the kinetic energy of the vehicle. Therefore, when the battery is fully charged it cannot accept a charging current. A buffer region is also often implemented in order to mitigate the safety hazard of overcharging li-ion batteries which can cause thermal runaway.

The torque limiter restricts the torque of the motor to the regions shown in Figure 3.11. In order to prevent the speed of the vehicle becoming negative, a negative torque request is only allowed when the speed of the vehicle is positive. When the SOC of the battery exceeds a limit set by the model designer, the negative torque request is sent through the *Tb* port to achieve mechanical braking, as depicted in Figure 3.11(a). If the SOC is below the SOC limit, the negative torque request is sent through the *Tm** port such that regenerative braking is realised, as depicted in Figure 3.11(b). This logic is implemented in lines 21 to 33 using a conditional if statement.

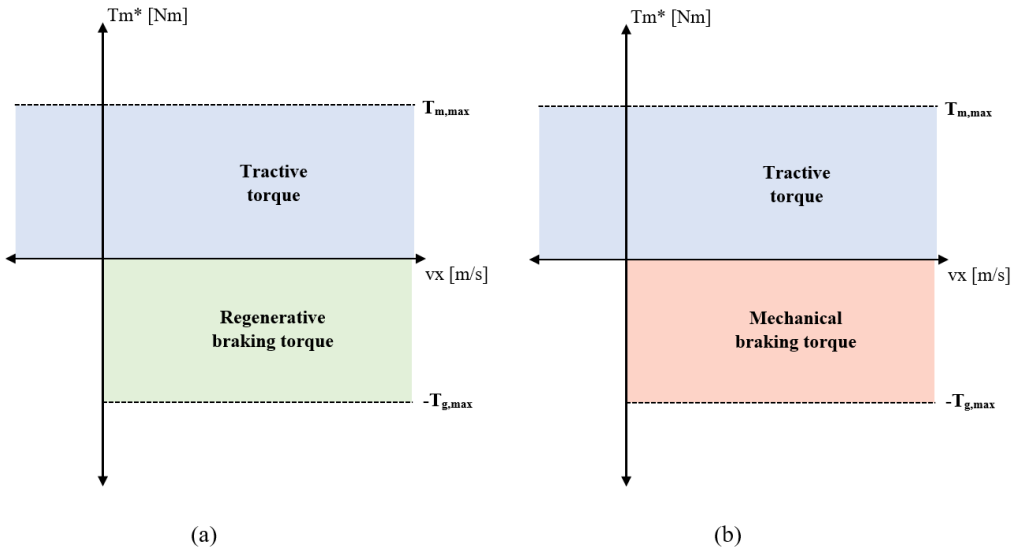

Figure 3.11. Torque operating regions and limits when the battery (a) can accept a charging current and when (b) the battery cannot accept a charging current.

3.13.2 Parameter acquisition

A summary of the parameters required for the driver model block is given in Table 3.9. The drive cycle speed and time points are not shown in Table 3.9 as this data is not considered as parameters but rather the main input to the model. The maximum motor and generator torque can be determined by considering the lower value of the maximum continuous power ratings of the motors and motor controllers.

Table 3.9. Driver model parameters.

Symbol	Description	Unit
$T_{m,\,max}$	Maximum motor torque	Nm
$T_{g,\,max}$	Maximum generator torque	Nm
K_p	Proportional PID constant	-
K_i	Integral PID constant	-
K_d	Derivative PID constant	-

The PID constant of the driver can be set using the heuristic Zeigler-Nichols approach. In this approach the integral and derivative gains are set to zero and the proportional constant is increased until it reaches the ultimate gain, K_u where the speed of the vehicle has consistent and stable oscillations (Ziegler & Nichols, 1993). The oscillation period, T_u is then used with K_u to set the PID constants according to Table 3.10 (Ziegler & Nichols, 1993).

Table 3.10. Ziegler-Nichols PID tuning (Ziegler & Nichols, 1993).

K_p	K_i	K_d
$0.6 \cdot K_u$	$\frac{1}{2} \cdot T_u$	$\frac{1}{8} \cdot T_u$

3.14 High voltage cabling

Copper losses in cabling from the battery to the inverter and from the inverter to the motors were considered by computing the equivalent resistance of the battery and motor cabling. A resistor from the Simscape™ electrical library was placed in series for each length of wire and the resistance can be computed using Equation 3.8 (Avison, 1989). Resistance of auxiliary cabling was ignored as the losses are negligible.

$$R = \frac{\rho_{cable} \cdot L}{CSA} \qquad \text{Equation 3.8}$$

In the above, R is the resistance of the conductor, ρ_{cable} is the resistivity of the cable conductor and CSA is the cross sectional area of the cable.

3.14.1 Parameter acquisition

A summary of the parameters required for the cable loss resistors is presented in Table 3.11. The lengths of cable can be measured if they are not known and the cross sectional area of the cable can be read of the markings on the cabling. The resistivity of the cabling can be determined based of the conductor material.

Table 3.11. High voltage cabling parameters.

Symbol	Description	Unit
L_{batt}	Battery cable length (total)	m
CSA_{batt}	Battery cable cross sectional area	m^2
L_{motor}	Motor cable length (per phase)	m
CSA_{motor}	Motor cable cross sectional area	m^2
ρ_{cable}	Conductor material resistivity	$\Omega \cdot m$

3.15 Parameter initialisation

A MATLAB™ script, shown in Appendix A.8, was written to initialise all the model parameters. This allows parameters to be analysed and easily changed across the entire model. The script file also reads the speed and time points of the selected drive cycle from an excel file in line 32 and 33. Once the script file is run, all the parameters are loaded as variables in the MATLAB™ workspace which can be read by Simulink and Simscape™.

3.16 Modelling of the Mamba EV

Figure 3.12 presents the topology of the complete model used to simulate the Mamba EV, presented in Section 1.2, using the Simulink and Simscape™ blocks discussed above. A larger image of the model also appears in Appendix C.3 to ensure readability of the text. The Mamba uses two motors each driving a rear wheel through separate drivetrains. Each motor is driven by a separate motor controller. Therefore, two rotational dynamics blocks, two motor blocks, two inverter blocks and two MTPA controller blocks were used and the motor torque nodes where connected in parallel to a single linear dynamics block.

Although the battery pack of the Mamba is physically split between the rear and front of the vehicle it may considered as one component in the electrical domain. The inputs of the inverter blocks and the auxiliary load block are paralleled as power is provided from a single battery pack. Finally, a driver model block is used to implement a drive cycle in order to determine the range

of the vehicle. Various drive cycles are implemented to simulate the Mamba EV and the results are presented in Chapter 4.

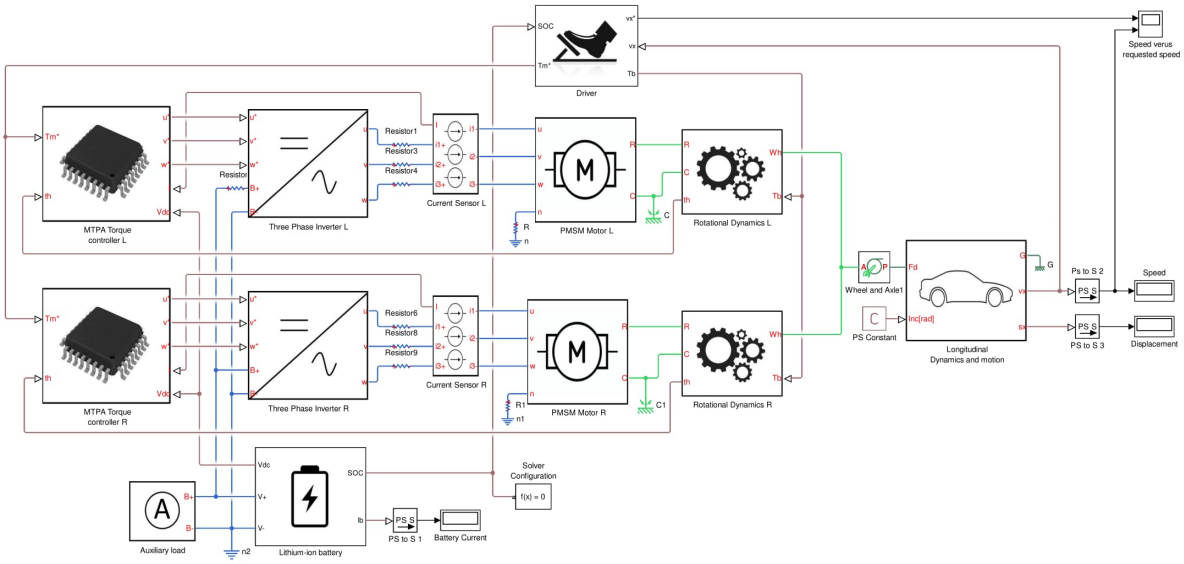

Figure 3.12. Complete Simscape™ model of the Mamba EV.

3.17 Mamba parameters

In order to simulate the Mamba, all the parameters presented in the preceding sections are required. In the following sections the parameters of the Mamba are presented per component or general category as well as the source of each parameter. All parameters also appear in Appendix A.8, where parameters are arranged according to their respective blocks.

3.17.1 Motor

Two *EnerTrac Corp.* Dual-603 motors with dual stator coils are used to drive the rear wheels of the Mamba. The stators are treated as a single stator in the model and therefore the parameters appearing in Table 3.12 are for each dual motor. Limited data was available on the datasheet however missing parameters were easily obtained from the motor manufacturer through e-mail communication with the owner. The viscous friction coefficient could not be obtained however Park et al. (2014) provide a value for a similar motor and the sensitivity of this parameter is very low. The rotor's moment of inertia was obtained from the CAD model of the motor supplied by the manufacturer.

Table 3.12. Motor parameters.

Symbol	Description	Value	Unit	Source
N	Number of pole pairs	12	-	E-mail (M. Gelbien, personal communication, August 2, 2016)
K_v	Velocity constant	0.733	rad/sV	Datasheet (Enertrac Corp., n.d.)
L_u, L_v, L_w	Stator *uvw* phase inductance	350	μH	Communication (M. Gelbien, personal communication, September 7, 2016)
L_d, L_q	Stator *dq* phase inductance	87.5	μH	Calculated using Equation 2.30
R_s	Phase resistance	0.0544	Ω	E-mail (M. Gelbien, personal communication, October 6, 2016)
λ_f	Flux linkage induced by permanent magnets	0.11367	Wb	Calculated using Equation 3.2
B_m	Viscous friction co-efficient	0.005	Nm·s/rad	Literature (Park et al., 2014)
J_r	Rotor moment of inertia	0.368	kg·m^2	CAD model

3.17.2 Motor controller

Four *Kelly Controls LLC* KLS14301-8080I sinusoidal wave brushless motor controllers were used to drive the motors. The motor controller is represented by the inverter and MTPA controller blocks. Two controllers are used to drive each set of motor coils and each set is represented as one controller block in the model. Therefore the parameters shown in Table 3.13 are for a set of two controllers. Limited data was obtained from the manual of the controller however other technical data was available from the manufacturer through e-mail communication, this is shown in Table 3.13.

Table 3.13. Motor controller parameters.

Symbol	Description	Value	Unit	Source
k_p	Proportional PI constant	80	-	Manual (Kelly Controls, 2015)
k_i	Integral PI constant	1000	-	Manual (Kelly Controls, 2015)
R_{on}	On state MOSFET resistance	9.7	mΩ	E-mail (F. Chen, personal communication, September 7, 2016)
P_{sw}	Rated switching losses	40	W	E-mail (F. Chen, personal communication, November 8, 2017)
I_{max}	Maximum continuous current	240	A	Manual (Kelly Controls, 2015)

3.17.3 Battery

The author was involved in the design and manufacture of the battery pack and therefore parameters could be easily obtained. A quantity of 2016 *Panasonic* NCR18650PF cells were assembled together to form the pack. The parameters used appear in Table 3.14. The voltage response of a pulse discharge current was not available and therefore the transient resistor and capacitor values could not be obtained without testing. The experimental procedure presented in Section 2.9.4.4 could not be used as the author did not have access to the necessary testing equipment.

The data presented for li-polymer cells by Min and Rincon-Mora (2006) was used to estimate the transient resistor and capacitor values as the cell chemistry is similar. It was assumed that the NCR18650PF cells would have a similar dynamic response to the cells tested by Min and Rincon-Mora (2006) however the total internal resistance of the NCR18650PF cell is 43 mΩ (Panasonic, 2013) as opposed to 175 mΩ of the cell used by Min and Rincon-Mora (2006). Therefore the same capacitor values were used however the resistor values were scaled linearly to ensure the total resistance equalled that of the PF cells and the results are shown in Table 3.14.

An OCV versus SOC curve could not be provided by the manufacturer and the lowest discharge voltage versus SOC curve was for a 0.2C rate. A discharge curve may be used only if it represents a discharge rate lower than 0.05C (Weng et al., 2014). Therefore a *REVOLECTRIX* PowerLab 8x2 battery analyser was used to obtain a voltage versus SOC curve at a discharge rate of 0.14 A (0.046C) which will provide an accurate estimation of the OCV as discussed in Section 3.11.2. The curve was then fitted to an analytical expression using the MATLAB™ Curve Fit toolbox.

An exponential function of the form of Equation 3.9 was determined to fit the data closer than the least squares approximation discussed in Section 2.9.4.4. The results of the curve fitting are shown in Table 3.14 and a screenshot of the curve fitting toolbox is shown in Appendix D.

$$OCV = a_o \cdot e^{a_1 \cdot SOC} + a_2 \cdot e^{a_3 \cdot SOC} \qquad \text{Equation 3.9}$$

Table 3.14. Battery parameters.

Symbol	Description	Value	Unit	Source
R_{Series}	Equivalent series resistance	0.019	43mΩ	Scaled data from Literature (Min & Rincon-Mora, 2006)
$R_{Trans,S}$	Short transient response resistance	0.012	Ω	Scaled data from Literature (Min & Rincon-Mora, 2006)
$C_{Trans,S}$	Short transient response capacitance	700	F	Literature(Min & Rincon-Mora, 2006)
$R_{Trans,L}$	Long transient response resistance	0.012	Ω	Scaled data from Literature (Min & Rincon-Mora, 2006)
$C_{Trans,L}$	Long transient response capacitance	4500	F	Literature (Min & Rincon-Mora, 2006)
C_N	Nominal cell capacity	2.9	Ah	Datasheet (Panasonic, 2013)
N_S	Number of cells in series	42	-	-
N_P	Number of cells in parallel	48	-	-
V_{min}	End-of-discharge voltage	2.5	V	-
a_0	OCV versus SOC equation coefficients	3.672	-	MATLAB™ curve fitting toolbox and experimental data
a_1		0.06615	-	
a_2		-1.907e^{-11}	-	
a_3		-14.22	-	

3.17.4 Drivetrain

The drivetrain is of a simple topology comprising only axle shafts and two Rzeppa CVJs per motor. Therefore the rotational inertia and efficiency of components not present in the drivetrain are set to zero and one respectively, as discussed in Section 3.6.1. The rotational inertia of the axle shaft was calculated using Equation 3.10 (Young & Freedman, 2012). The resultant parameters appears in Table 3.15.

$$J_{as} = \frac{1}{2} m_{as} \cdot R_{as}^2$$ Equation 3.10

Table 3.15. Drivetrain parameters.

Symbol	Description	Value	Unit	Source
J_{as}	Axle shaft rotational inertia	6.15×10^{-4}	kg·m^2	Calculation
J_{wh}	Wheel rotational inertia	1.06	kg·m^2	Literature (Automotive Forums, 2017)
J_{df}	Differential rotational inertia	0	kg·m^2	-
J_{gb}	Gearbox rotational inertia	0	kg·m^2	-
G_{gb}	Gearbox ratio	1	-	-
G_{df}	Differential ratio	1	-	-
η_{df}	Differential efficiency	1	%	-
η_{gb}	Gear box efficiency	1	%	-
η_{cl}	Clutch efficiency	1	%	-
η_{as}	Axle shaft efficiency	99.5	%	Literature (Fujio, 2013)

The efficiency of the CVJs was not available from the manufacturer and therefore an approximation of the energy losses was used. The approximation used is the linear increase in energy loss rate from approximately 0.25 % at a joint angle of 4° to 1.25 % for a joint angle of 12° for standard Rzeppa joints (Fujio, 2013). Under maximum and neutral suspension deflection, the angle of the Mamba's CVJs is 12.66° and 1.19° respectively (Sim, Woods, Mons, & Chetty, 2016). Therefore the minimum listed loss value (at 4°) was considered which will also include further losses as the angle of the drive shaft changes due to road asperities. The reported loss is for one joint and therefore the energy losses were doubled to determine the total efficiency shown in Table 3.15.

3.17.5 Tyres

The Mamba uses *Continental* EcoContact 5 tyres with different sizes on the front and rear axles. Two 185/55 R15 tyres are used on the front and two 225/45 R17 are used on the rear axle. The ISO28580 rolling resistance coefficients were obtained for the front and rear tyres from the manufacturer through e-mail communication with the head of rolling resistance testing at Continental AG. However the SAE J1269 coefficients, which appear in Table 3.16, were only available for the front tyres. These values were used for both the front and rear tyres in order to capture the effects of speed and tyre pressure on the rolling resistance force. This is a reasonable

approximation as the ISO28580 coefficient of the rear tyres is only 1.3 % greater than the front tyres (C. Struebel, personal communication, October 18, 2016).

Table 3.16. Tyre parameters.

Symbol	Description	Value	Unit	Source
P	Tyre inflation pressure	2.5	bar	Assumed
a	SAE J1269 rolling resistance coefficient (185/55 R15)	0.111	-	E-mail (C. Struebel, personal communication, October 18, 2016)
b		2.53×10^{-4}	-	
c		8.67×10^{-7}	-	
α		-0.388	-	
β		0.940	-	
R_{wh}	Wheel diameter	0.3172	m	Literature (Errol's Tyres, n.d.)

3.17.6 Car mass and weight distribution

The total mass of the car was obtained by weighing the car (with no driver) and adding an estimated driver mass achieving the total vehicle mass, as shown in Table 3.17. The weight distribution of the car was determined from the CAD model.

Table 3.17. Car mass parameters.

Symbol	Description	Value	Unit	Source
m	Vehicle mass	657	kg	572 kg (measured) + 85 kg driver
f	Distance from COM to front axle	1.2563	m	CAD model
r	Distance from COM to rear axle	1.0937	m	CAD model
h	Distance from COM to ground	0.3809	m	CAD model

3.17.7 Aerodynamics

The aerodynamic drag coefficient was computed from a CFD analysis carried out by another vehicle designer and the results appear in Table 3.18 (Wieringen, Gyasi-Agyei, & Reddy, 2017). The drag coefficient was taken at nominal conditions at a simulated speed of 80 km/h.

Table 3.18. Aerodynamic parameters.

Symbol	Description	Value	Unit	Source
ρ	Air density	1.25	kg·m^3	Literature (Larminie & Lowry, 2013)
C_d	Aerodynamic drag coefficient	0.33725	-	CFD analysis (Wieringen et al., 2017)
A_f	Frontal area	1.55	m^2	CAD model

3.17.8 DC/DC

An *Elcon* TDC-144V-12V converter is used in the Mamba. The efficiency of the DC/DC is assumed as its maximum efficiency as this is the only efficiency data available from the manufacturer, as shown in Table 3.19. The auxiliary system of the Mamba does not include any high voltage components and therefore the high voltage auxiliary draw is set to zero. The low voltage auxiliary load was estimated by summing the power draw of auxiliary components which draw a continuous load whilst the car is driving.

Table 3.19. DC/DC parameters

Symbol	Description	Value	Unit	Source
P_{LV}	Low voltage auxiliary loads	100	W	Calculated
P_{HV}	High voltage auxiliary loads	0	W	-
η_{conv}	DC/DC efficiency	92	%	Datasheet (Elcon, n.d.)

3.17.9 Driver model

The parameters used for the driver model appear in Table 3.20. The PID constants were tuned using the Zeigler-Nichols approach introduced in Section 3.13.2, to ensure the speed of the vehicle did not differ from the requested speed throughout the simulation. The maximum SOC at which regenerative braking is allowed was set according to the battery management system of the vehicle. The maximum motor and generator torque values were set according to the maximum continuous torque of the motor which was obtained from the manufacturer. This value was used as it was lower than the maximum continuous torque rating of the controllers.

Table 3.20. Driver model parameters.

Symbol	Description	Value	Unit	Source
K_p	Proportional PID constant	200	-	Tested
K_i	Integral PID constant	100	-	Tested
K_d	Derivative PID constant	25	-	Tested
SOC_{regen}	Maximum SOC at which regenerative braking is permitted	96	%	-
$T_{m,\,max}$	Maximum motor torque	400	Nm	(M. Gelbien, personal communication, January 12, 2016)
$T_{g,\,max}$	Maximum generator torque	400	Nm	-

3.17.10 High voltage cabling

The parameters of the high voltage cabling were either known by the author or were measured and calculated to attain the values shown in Table 3.21. All cabling used copper conductors and therefore the resistivity of copper was utilised.

Table 3.21. High voltage cabling parameters.

Symbol	Description	Value	Unit	Source
L_{batt}	Battery cable length (total)	8	m	Measured
CSA_{batt}	Battery cable cross sectional area	95×10^{-6}	m^2	-
L_{motor}	Motor cable length (per phase)	0.8	m	Measured
CSA_{motor}	Motor cable cross sectional area	16×10^{-6}	m^2	-
ρ_{Cu}	Copper resistivity	1.68×10^{-8}	$\Omega \cdot m$	Literature (Young & Freedman, 2012)

3.18 Simulation setup

A local solver was used to simulate the Simscape™ model with the configuration parameters shown in Figure 3.13. A backward Euler approach is more stable than a trapezoidal rule approach and is recommended when no oscillations are expected (MathWorks™, 2014). Therefore, Backward Euler was selected as a solver type. As sample time is decreased, both the computational cost and model fidelity increases. As an average value inverter is used (and is thus not the limiting factor), the sample time should be small enough to ensure that the dynamics of the three phase motor supply are captured according to ω_r. The electrical period at maximum motor speed (considering a vehicle speed of 120 km/h) can be calculated using Equation 2.32 to be 0.005 s. The sample time was therefore set to 0.0003 s which was is approximately 15 times smaller than the period.

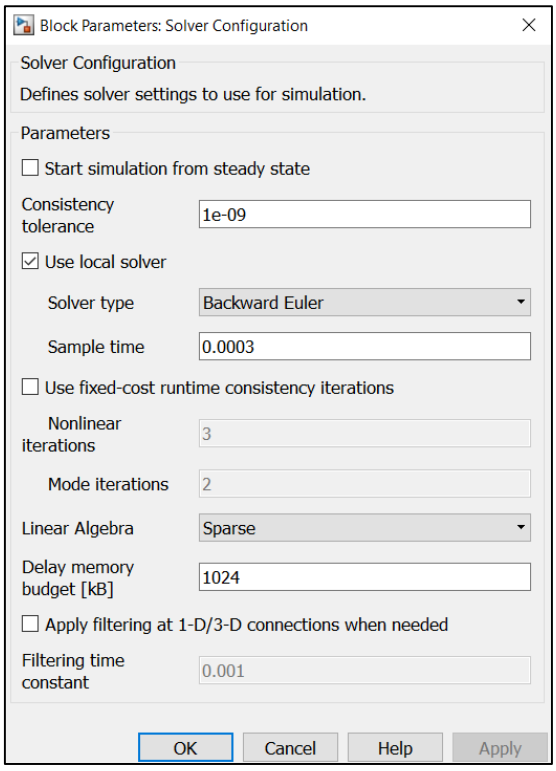

Figure 3.13. Simscape™ solver configuration settings.

A variable time step solver was selected as opposed to a fixed-cost solver to allow for a decrease in simulation time during not transient periods. The global solver used was an ode45 solver which is a variable step solver as is recommended by MathWorks™ in line with the flowchart presented in Figure 2.3.

3.19 Chapter summary

This chapter discussed the implementation of the equations presented in the previous chapter to model each subsection of the EV and the interconnection of the sub-models to build a complete energy model. The complete energy model was built using custom coded Simscape™ component blocks which represent a component or subsystem of the EV. The development of each block was outlined including a motivation for the selection of the primary modelling equations, supported by the literature survey. The limitations and assumptions of each block and the chosen modelling technique was discussed as well as possible parameter acquisition approaches. The interconnection of these blocks into a complete model to represent the Mamba EV was also shown.

The parameters of the Mamba EV are presented followed by a motivation for the Simscape™ simulation settings and parameters chosen. The results of the simulations of the Mamba EV during various different drive cycles will be presented in the following chapter using the developed energy model.

CHAPTER 4: RESULTS

The primary input to the model developed in this work is a set of speed and time points defined by a particular drive cycle. Numerous different drive cycles are available as discussed in Section 2.11. The WLTP drive cycle was chosen to simulate the energy consumption and range of the Mamba EV as it accurately represents real driving conditions and electric vehicle manufacturers are required by legislation to use the WLTP cycle when advertising the range of the vehicle, as discussed in Section 2.11.3.2. This drive cycle consists of four regions, a low speed region, a medium speed region, a high speed region and an extra-high speed region, as shown in Figure 2.42, which is repeated here for ease of reference. A city version of the cycle is also available which includes only the low and medium sections (International Council on Clean Transportation, 2013).

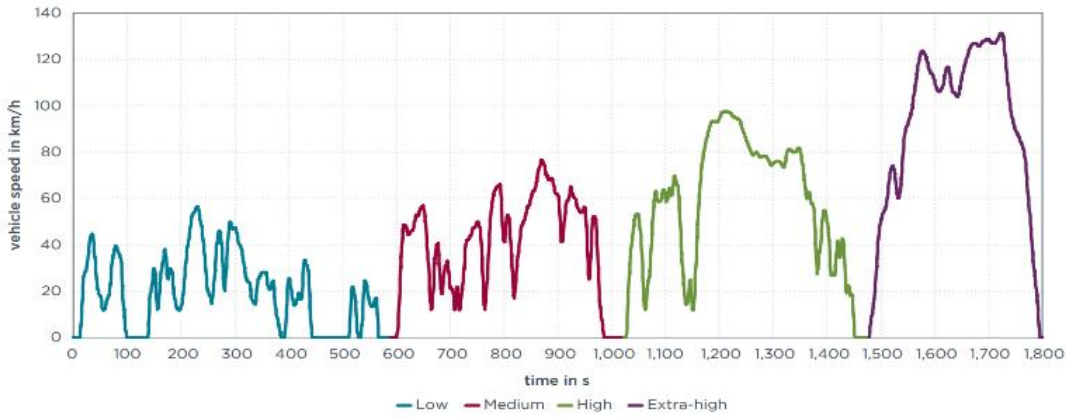

Figure 2.42. WLTP drive cycle for a Class 3 vehicle (International Council on Clean Transportation, 2013).

If the legal speed limit of the country does not exceed 120 km/h, then the extra-high speed region may be ignored (International Council on Clean Transportation, 2013). In order to test the range of an EV the full cycle followed by a city cycle is run repeatedly until the battery is depleted. If the range of the vehicle exceeds the distance of four repeated cycles, a shortened test procedure must be used to determine the range of the vehicle (International Council on Clean Transportation, 2013). The shorted test procedure consists of the full cycle followed by the city version of the cycle as well as two constant speed sections of 80 km/h and is discussed in detail in Section 2.11.3.2. A shortened version of the city cycle is not available and therefore the city cycle must be repeated until the battery is depleted in order to determine the range of the vehicle.

In the following chapter three different variations of the WLTP cycle are run in order to compare the range and energy consumption of the Mamba under different driving conditions. A city cycle was first run, consisting of the WLTP city cycle repeated until the battery was depleted. Secondly a hybrid cycle was run, which consists of repetitions of the full cycle in order to simulate a combination of city and highway driving. Finally, the shortened WLTP cycle was run. As a large portion of this cycle consists of a constant speed range of 80 km/h, this cycle can be considered a highway driving cycle. The result of this cycle also provides an estimate of the vehicle range which can be advertised in accordance with the WLTP regulations.

The Simscape™ model discussed in this chapter was run using the parameters presented in Section 3.17, and the simulation setup outlined in Section 3.18, for each of the three drive cycles. The results of each simulation appear in the following subsections and the chapter is then concluded with a summary of the results.

4.1 WLTP city cycle

Table 4.1 shows the main simulation results and simulation statistics of the full city cycle simulation. A Sankey diagram showing how the battery energy is used during the drive cycle appears in Figure 4.1.

Table 4.1. City WLTP simulation results and statistics.

Metric	**Value**
Range	420.8 km
Driving time	54885.46 s
Average speed	27.6 km/h
Maximum absolute speed error	0.70 m/s
Simulation time	11:55:06 hours
Average step size	3.00 $x10^{-4}$ s
Total steps	182969852

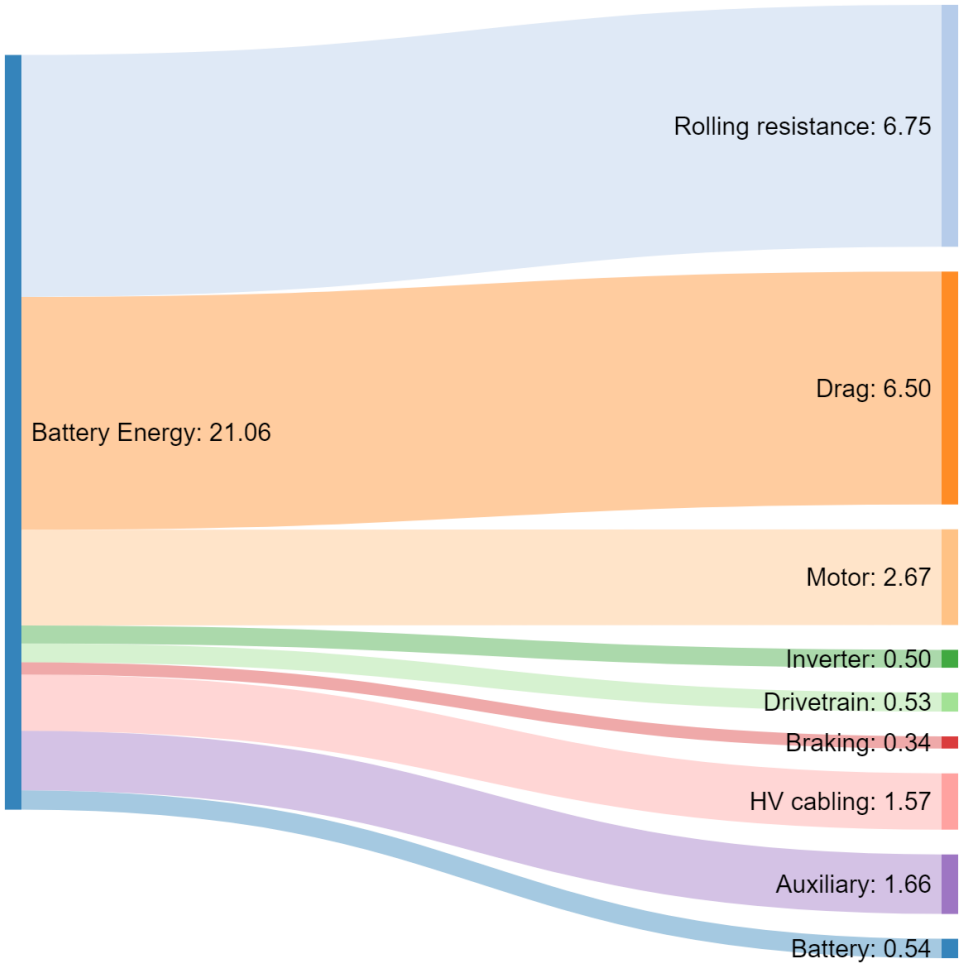

Figure 4.1. Sankey diagram showing the distribution of battery energy [kWh] during a WLTP city cycle.

The battery voltage and SOC over the entire simulation is shown in Figure 4.2. In order to ensure readability of the graphs, only the first city subcycle is shown for the remaining variables as the dynamic response of the repeated subcycles will be similar throughout the entire simulation as the same city subcycle is repeated. The actual and requested speed and vehicle displacement appear in Figure 4.3 and actual vehicle speed and power at the wheels appears in Figure 4.4. Requested motor and mechanical braking torque, torque at the wheels and battery current appear in Figure 4.5 before regenerative braking is allowed.

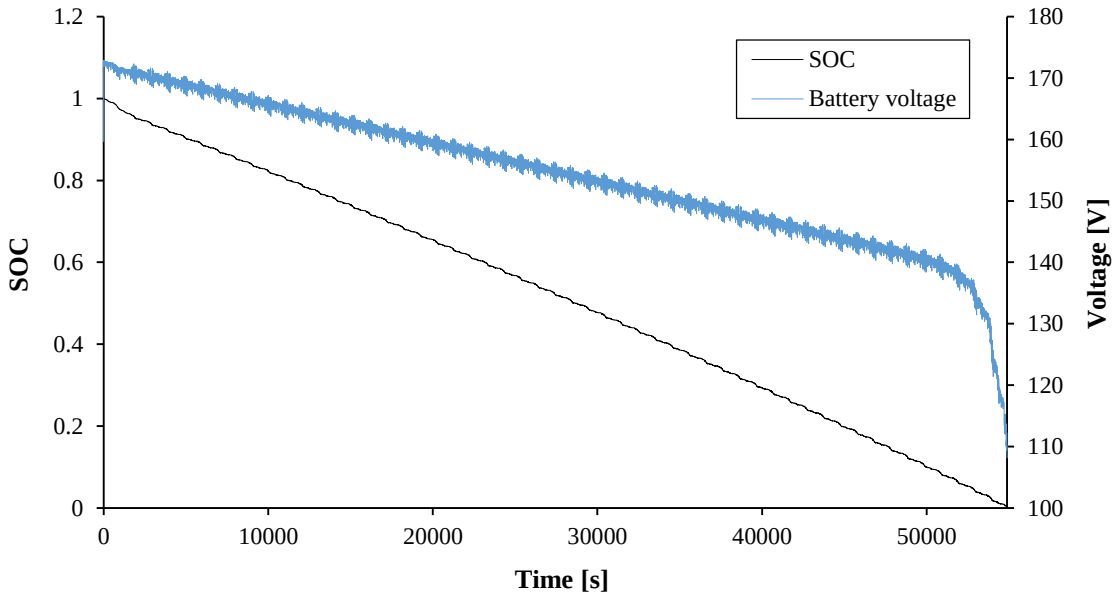

Figure 4.2. Battery voltage and SOC versus time over the full city cycle.

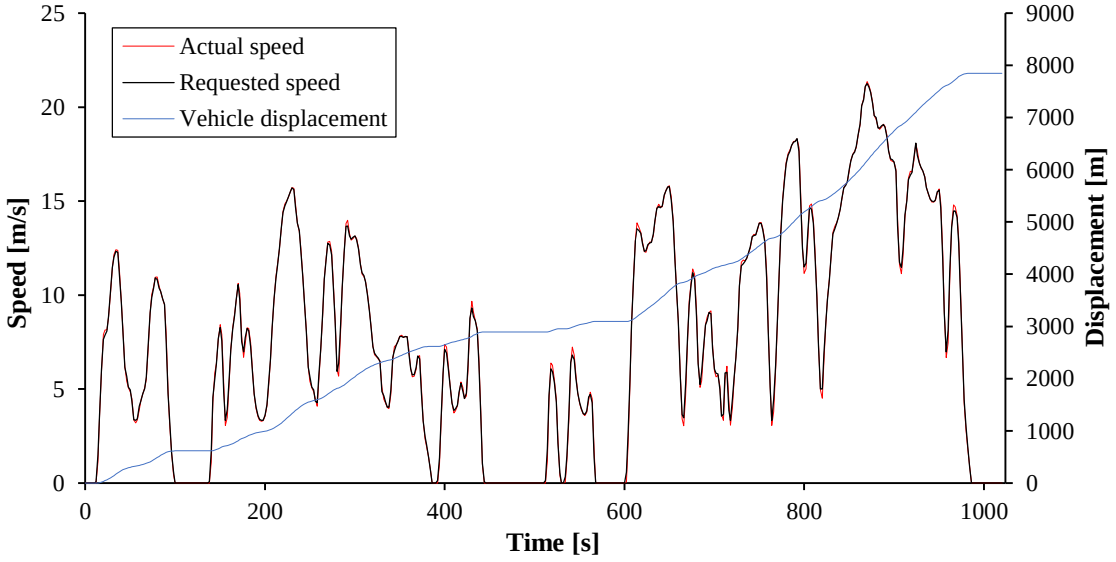

Figure 4.3. Actual and requested vehicle speed and displacement versus time over one city cycle.

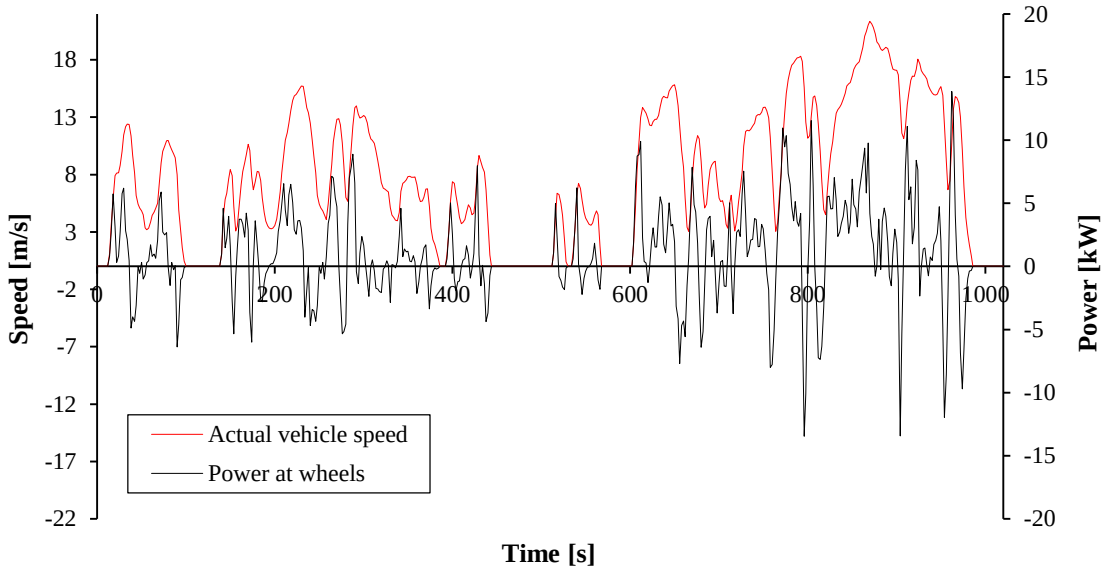

Figure 4.4. Power at the wheels and vehicle speed versus time over one city cycle.

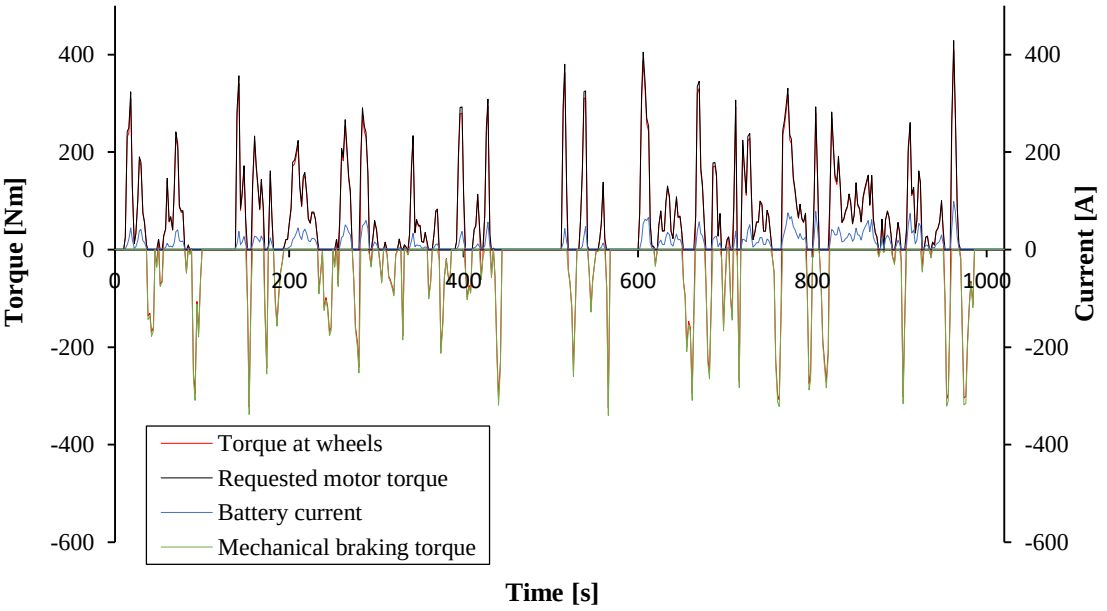

Figure 4.5. Requested torque, actual torque and battery current versus time over one city cycle with no regenerative braking.

The requested torque, actual torque and battery current versus time is also shown for the third city subcycle of the simulation as the battery SOC at this stage of the simulation was below the threshold to allow regenerative braking, as seen in Figure 4.6.

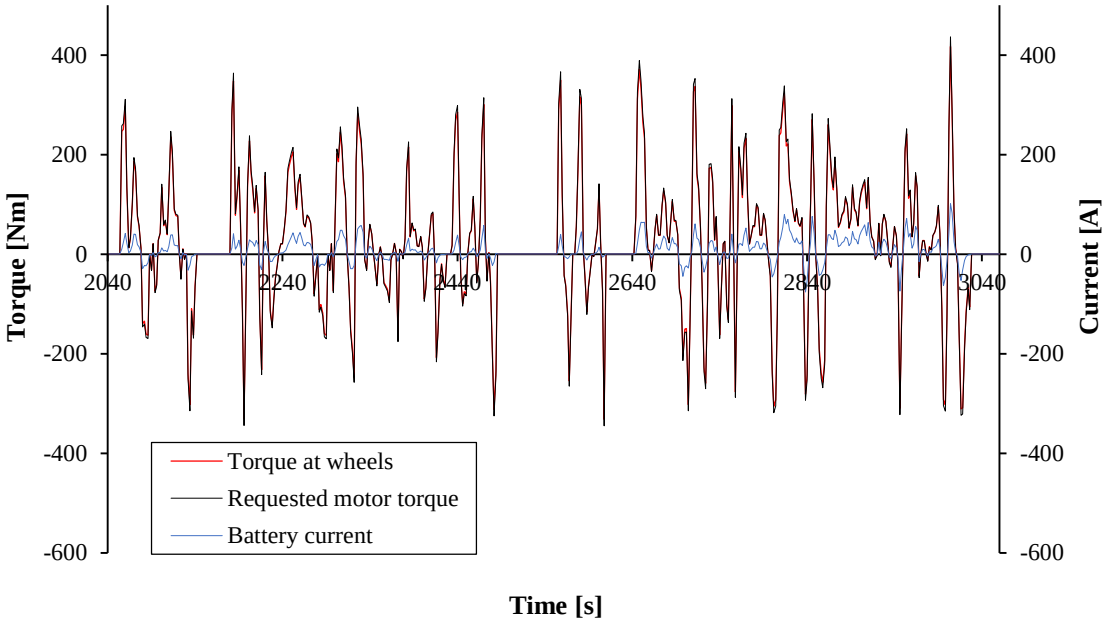

Figure 4.6. Requested torque, actual torque and battery current versus time over one city cycle with regenerative braking.

4.2 WLTP hybrid cycle

Table 4.2 shows the main simulation results and simulation statistics of the full hybrid cycle simulation. A Sankey diagram showing how the battery energy is used throughout the drive cycle appears in Figure 4.7.

Table 4.2. Hybrid WLTP simulation results and statistics.

Metric	Value
Range	366.8 km
Driving time	40224.54 s
Average speed	32.8 km/h
Maximum absolute speed error	0.71 m/s
Simulation time	8:31:04 hours
Average step size	3.00 x10^{-4} s
Total steps	134095225

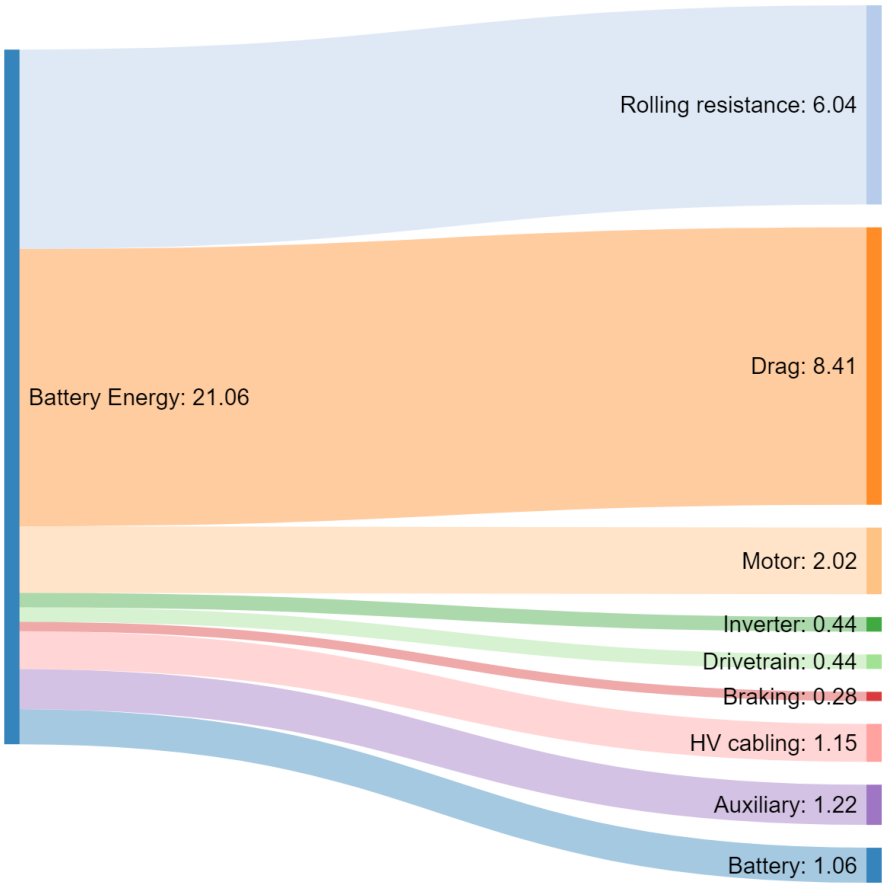

Figure 4.7. Sankey diagram showing the distribution of battery energy [kWh] during a WLTP hybrid cycle.

The battery voltage and SOC over the entire simulation is shown in Figure 4.8. In order to ensure readability of the graphs, only the first hybrid subcycle is shown for the remaining variables as the dynamic response of the repeated subcycles will be similar throughout the entire simulation as the same hybrid subcycle is repeated. The actual and requested speed and vehicle displacement appear in Figure 4.9 and actual vehicle speed and power at the wheels appears in Figure 4.10. Requested motor and mechanical braking torque, torque at the wheels and battery current appear in Figure 4.11.

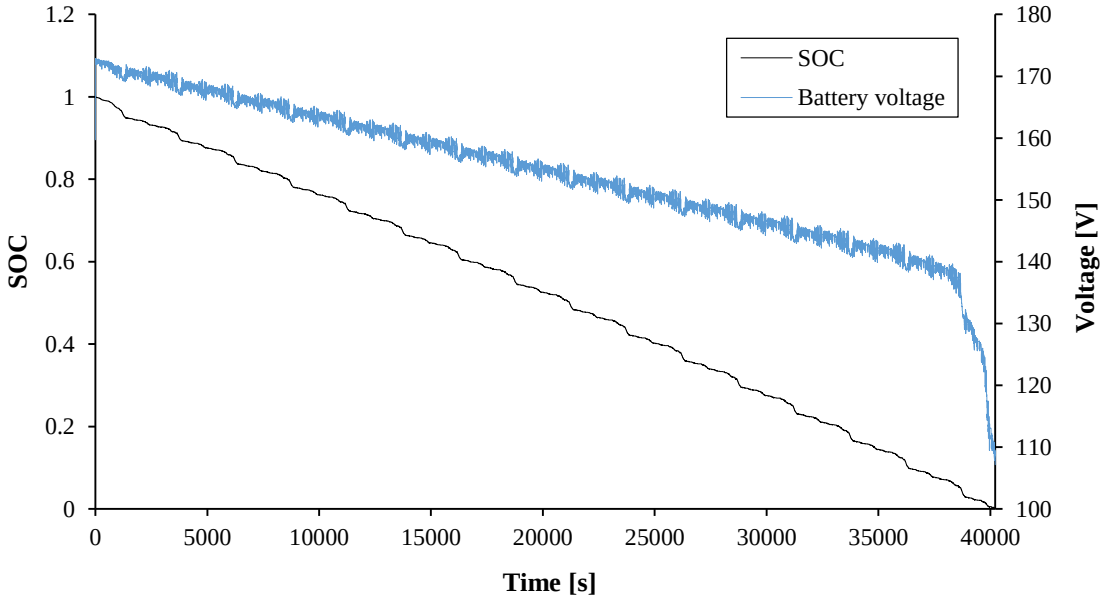

Figure 4.8. Battery voltage and SOC versus time over the full hybrid cycle.

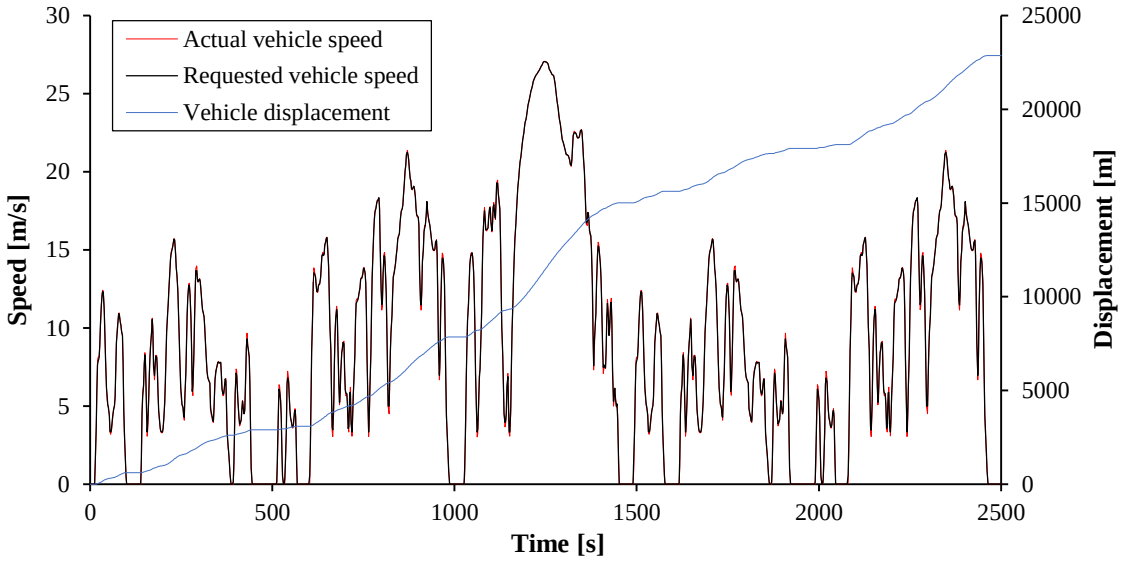

Figure 4.9. Actual and requested vehicle speed and displacement versus time over one hybrid cycle.

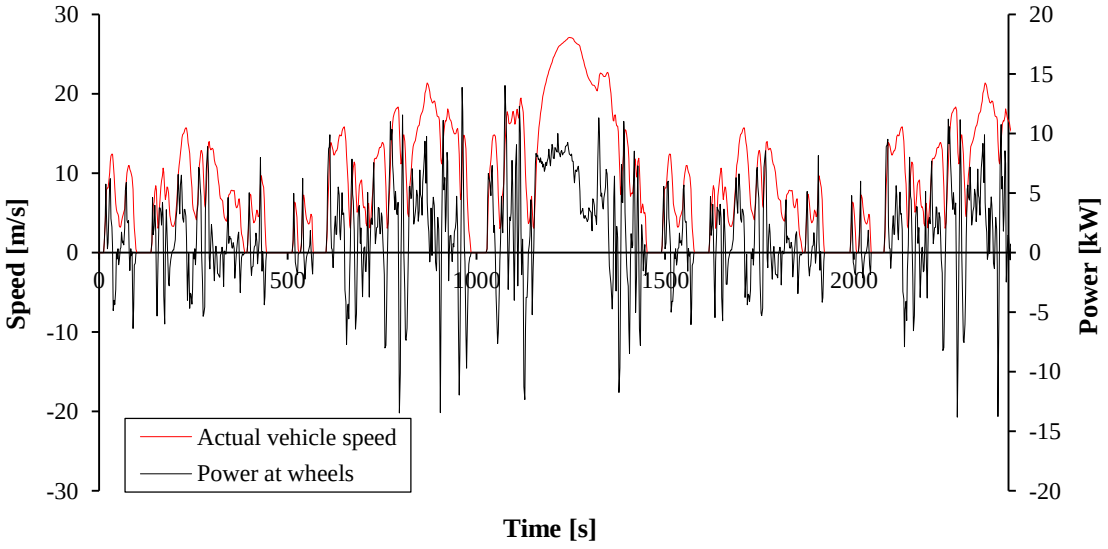

Figure 4.10. Power at the wheels and vehicle speed versus time over one hybrid cycle.

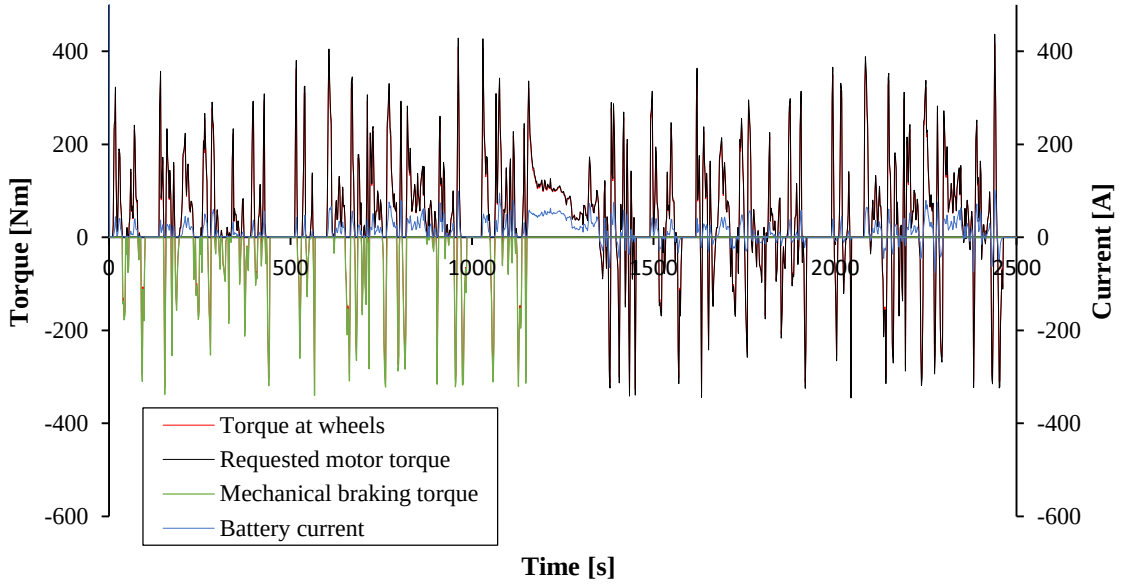

Figure 4.11. Requested torque, actual torque and battery current versus time over one hybrid cycle.

It can be observed in Figure 4.11 that the battery SOC falls below the threshold to allow regenerative braking during the first subcycle and therefore a separate graph is not required to show the results of regenerative braking.

4.3 WLTP highway cycle

Table 4.3 shows the main simulation results and simulation statistics of the shortened WLTP drive cycle simulation representing highway driving conditions. A Sankey diagram showing how the battery energy is used throughout the drive cycle is shown in Figure 4.12.

Table 4.3. Highway WLTP simulation results and statistics.

Metric	Value
Range	285.3 km
Driving time	15776.5 s
Average speed	64.8 km/h
Maximum absolute speed error	0.88 m/s
Simulation time	3:13:58 hours
Average step size	3.00 x10^{-4} s
Total steps	55217874

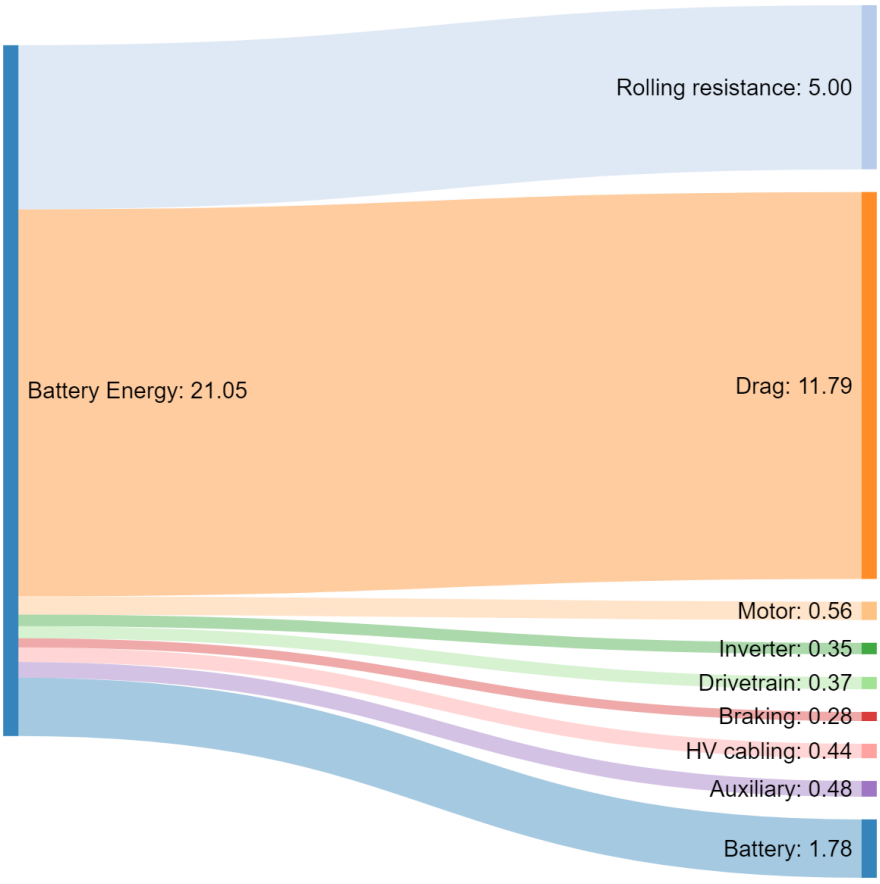

Figure 4.12. Sankey diagram showing the distribution of battery energy [kWh] during a highway WLTP cycle.

The battery voltage and SOC over the entire simulation is shown in Figure 4.13.

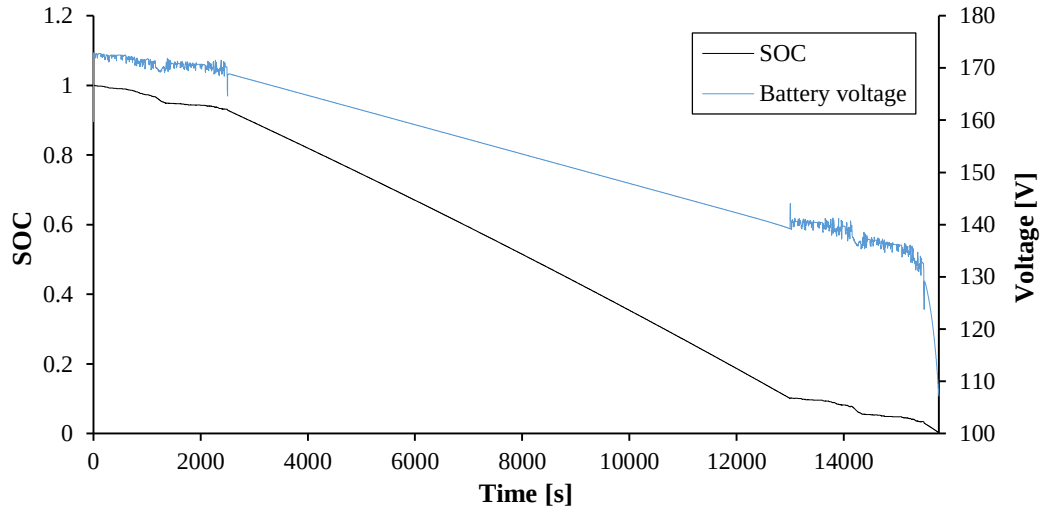

Figure 4.13. Battery voltage and SOC versus time over the full highway cycle.

The actual and requested vehicle speed and displacement versus time over the full highway cycle is shown in Figure 4.14, which also shows the two constant speed sections of 22.22 m/s (80 km/h). The first constant speed section was run for 10500 s and the second constant speed section was started when 2.9 % of the battery energy was available. Therefore the cycle meets the criteria set out by the regulation which states that the amount of charge in the battery should be 10 % or less when the second constant speed section is started (International Council on Clean Transportation, 2013).

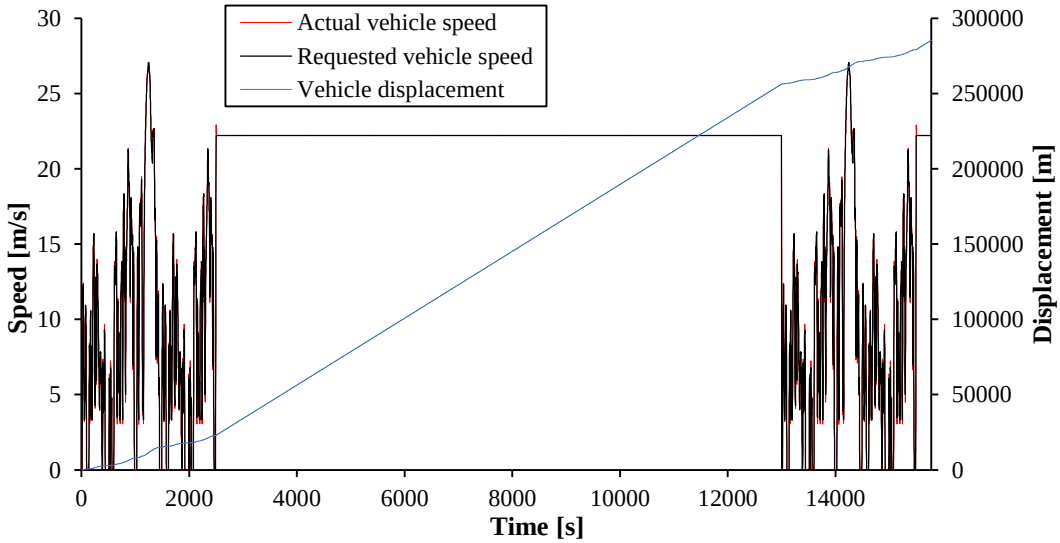

Figure 4.14. Actual and requested vehicle speed and displacement versus time over the full highway cycle.

Other results are not shown for this cycle as the results of the dynamic phases of the simulation will be the same as the results presented for the hybrid cycle in the previous section as the same subcycle is used.

4.3.1 Increase in vehicle mass

Table 4.4 shows the main simulation results and simulation statistics of the same cycle with a 50 % increase in vehicle mass. A Sankey diagram showing how the battery energy is used throughout the drive cycle is shown in Figure 4.15.

Table 4.4. Highway WLTP simulation (50 % increase in vehicle mass) results and statistics.

Metric	Value
Range	243.7 km
Driving time	12439.50 s
Average speed	70.63 km/h
Maximum absolute speed error	0.88 m/s
Simulation time	2:31:11 hours
Average step size	2.88 x10^{-4} s
Total steps	43538315

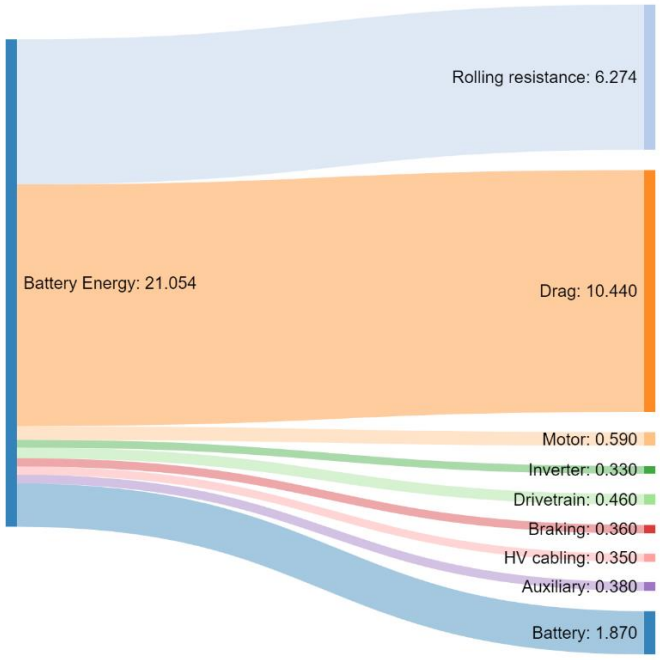

Figure 4.15. Sankey diagram showing the distribution of battery energy [kWh] during a highway WLTP cycle with a 50 % increase in vehicle mass.

4.3.2 Increase in step size

A highway simulation was also run using the original vehicle mass with the time step increased to 0.0005 s. The simulated range remained the same at 285.3 km and the simulation time decreased to 2:50:05 hours.

4.4 Summary of results

A summary of the range and average speed for each of the three drive cycles is shown in Table 4.5 and a summary of the energy losses in Table 4.6.

Table 4.5. Range and average speed of each drive cycle.

	City	**Hybrid**	**Highway**
Range	420.8 km	366.8 km	285.3 km
Average speed	27.6 km/h	32.8 km/h	64.8 km/h

Table 4.6. Summary of energy losses for each drive cycle.

	City		**Hybrid**		**Highway**		**Highway** (50% mass increase)	
	Loss [kWh]	**%**	**Loss [kWh]**	**%**	**Loss [kWh]**	**%**	**Loss [kWh]**	**%**
Rolling resistance	6.75	32	6.04	29	5.00	24	6.27	30
Aerodynamic drag	6.49	31	8.41	40	11.79	56	10.44	50
Motor	2.67	13	2.02	10	0.560	3	0.592	3
Drivetrain	0.530	2	0.438	2	0.374	2	0.456	2
Braking	0.340	2	0.277	1	0.277	1	0.362	2
Inverter	0.502	2	0.436	2	0.350	2	0.326	2
HV Cable	1.57	7	1.15	5	0.444	2	0.354	2
Auxiliary	1.66	8	1.22	6	0.476	2	0.376	2
Battery	0.540	3	1.06	5	1.78	8	1.87	9

4.5 Chapter summary

This chapter presented detailed results of the simulation of the Mamba EV across three different drive cycles; a city drive cycle, a highway drive cycle and a hybrid drive cycle. The dynamic response of crucial variables was graphically presented for each drive cycle. The most important result of these simulation was the range which was predicted using the model and the associated Sankey diagrams which provided a visual representation of how energy is lost during a drive cycle. Key simulation statistics such as runtime and number of steps was also provided for each drive cycle. The results will be discussed in the following chapter followed by concluding remarks in the final chapter.

CHAPTER 5: DISCUSSION

The primary aim of this work was to characterise and quantify the energy consumption and efficiency of the Mamba EV. The crucial objective to achieve this aim was developing and building a model to simulate the range of the vehicle in order to quantify energy usage for a particular drive cycle. To this end, a Simscape™ model was developed using primarily custom coded components. Custom coded components were used in order to allow complete flexibility in building a model that met the exact aims and objectives of this work as well as ensuring a freely available design which can be improved and altered in future iterations and adapted to other EV architectures and designs. By using the Simscape™ language, a well-documented and universal approach to physical modelling, a strong foundation was available to not only further develop the model but also to allow for future improvement and modification.

A further requirement of the model was the ability to assist vehicle designers in optimising the EV through selecting or designing the vehicle's chassis and its components to increase the overall efficiency of the EV. In order to achieve this, various important considerations were identified. Firstly, in order to select the most suitable components, the vehicle designer must rely only on non-proprietary data obtainable either through communication with the manufacturer, directly from datasheets or through calculation or manipulation of available data. Secondly, the model should be universal, as energy optimisation may not only involve the selection of components but also the adjustment of the architecture and topology of the EV. This is especially true for the drivetrain, as EVs can employ a wide range of different topologies making use of different components. Finally, the model should be able to simulate the energy consumption quick enough to ensure optimisation through iteration whilst still maintaining model fidelity.

This work began with an in-depth and thorough survey of the available literature to assess the energy loss mechanisms of the vehicle and how each mechanism could be modelled. The investigation was thorough in two senses, firstly an extensive range of energy loss mechanisms were considered and secondly each mechanism of energy loss was considered in detail to ensure it was accurately captured by the modelling approach chosen. This led to the consideration of energy losses often ignored in other models and by other authors such as losses due to suspension and auxiliary loads. Also, the complexities of rolling resistance are often ignored through the use of a simple approximation intended to allow for the comparison of tyres which does not accurately model energy loss phenomena.

5.1 Model development

Two primary choices were made in developing the energy model presented in this work. Firstly, the use of Simscape™ as a modelling tool and secondly, the use of a dynamic physics based modelling approach. The merits of this approach and the modelling tool have already been discussed in depth and it was found these approaches provided the greatest flexibility and accuracy in modelling each sub-system of the EV.

Although the broad modelling approach chosen is dynamic physics based modelling, not all components employ a true physics model. The battery model relies on the physical simulation of an electrical circuit which models the behaviour of a li-ion cell. The rolling resistance and aerodynamic drag model rely on empirical approaches, however crucially the empirical data can be easily obtained and does not require experimental testing. The auxiliary load block relies on a steady-state modelling approach which is sufficient to model the Mamba as no HVAC system is used. The motor is modelled with a physics based model which considers operation up to the base speed of the motor as core losses are not considered. The motor inverter is modelled as an equivalent circuit which ignores the dynamics of the high frequency switching devices whilst ensuring the energy losses resulting from these devices is captured. This significantly reduces the computational complexity of the model without reducing model fidelity.

As li-ion batteries have only recently begun to become popular in vehicle design, many models rely on simplified battery models designed for older chemistries or assume a constant efficiency approach. Also, many models do not accurately capture the voltage response of the battery. The voltage response of the battery is important in determining when the battery is depleted as well as determining the energy losses of the battery which is a function of battery current and therefore battery voltage. Also, the battery voltage limits the voltage applied to the motor as the inverter can only step down voltage. The battery model developed in this work relies on the parameters of a single cell to represent the entire battery pack which usually comprises a number of cells connected together in series and parallel to form the complete pack.

An extremely universal drivetrain model was employed which considers a variety of different components even though this was not necessary for the Mamba EV, which employs a very simple drivetrain. The modelling approach also allows for different drivetrain topologies to be easily modelled by utilising the “drag and drop” approach to rearrange the topology of the model. This is an important consideration in developing a universal EV model as the drivetrain of EVs can vary drastically due to the simplicity of electric drivetrains and the use of hub motors.

5.2 Analysis of results

The developed model was then used to run various simulations of the Mamba EV. This was shown in Section 3.17, where the procurement of each parameter of the Mamba was detailed. This section evidenced that all of the parameters of the Mamba were obtainable without experimental testing, ensuring the vehicle can be simulated early in the design phase. The only exception was the coefficients of the OCV curve which were determined experimentally in order to increase the fidelity of the simulation. Typically, the OCV curve of a cell is provided by a manufacturer however in the case of the cells used for the battery of the Mamba, a curve was not provided and the lowest discharge voltage versus capacity curve was a 0.2C curve. Testing of battery parameters only requires the acquisition of at least three sample cells (to achieve a statistical average) and therefore experimental testing of battery parameters is feasible.

The results show that the model is able to compute the range of each drive cycle as well as the energy consumption of each component or energy loss mechanism, as shown by the Sankey diagrams presented in Chapter 4. Furthermore, the model is able to capture the dynamic response of many other variables throughout the simulation. Such variables include the vehicle speed, torque, power, battery voltage, current and SOC as shown by the graphs presented in Chapter 4.

Conventional IC vehicles typically have lower fuel consumption for highway driving compared to city driving due to the losses of braking energy and the relative inefficiency of an IC engine at low power and varying speed. EVs however are able to recuperate the energy lost during braking through regenerative braking and therefore they are expected to have a greater range during city driving as the aerodynamic losses are significantly reduced. This was evidenced through the simulated range of each driving cycle. The highest range, of 420.8 km was observed during city driving and the lowest range of 285.3 km was observed during highway driving. The hybrid cycle showed a range between these two values, 366.8 km.

The Sankey diagrams provide a wealth of information when characterising the energy losses of the EV according to different driving styles. They provide a clear and graphical means of comparing the energy losses across different drive cycles. The highway and city cycles show the most variation as they simulate two very different driving conditions and are shown side by side in Figure 5.1 for ease of comparison.

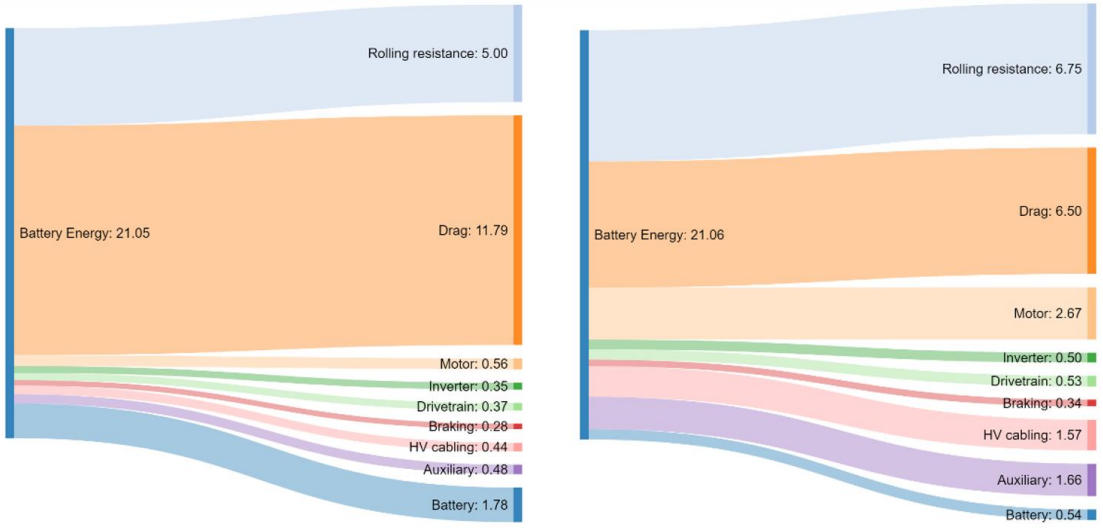

(a) Highway (b) City

Figure 5.1. Sankey diagrams of the (a) highway and (b) city cycle.

For the highway cycle, the losses are dominated by aerodynamic drag as the energy is proportional to the third power of speed. On the contrary, during the city cycle, the greatest loss resulted from rolling resistance although the aerodynamic loss was only marginally smaller. As the city drive cycle is a highly transient cycle, the motor losses contribute a significantly greater portion than the highway cycle as losses are increased under acceleration and deceleration (regenerative braking), which is proportional to motor current which results in an exponential increase in copper losses. For this same reason the HV cabling losses during the city cycle are significantly greater.

Because battery energy losses are also a function of current, due to the internal resistance of the battery, it was expected that the battery losses for the city cycle should be greater. However, the results showed a greater energy loss during highway driving. The reason for this phenomenon is due to the voltage drop caused by a discharge current and because the simulation is terminated when the battery reaches its end-of-discharge voltage. When the highway cycle ended the vehicle was travelling at a higher speed and therefore drawing more current from the battery. This in turn caused a voltage drop and the cycle was terminated even though the battery could still deliver power at a reduced rate. Therefore, the usable capacity of the battery during the highway driving cycle was less and this resulted in a greater energy loss figure.

The auxiliary loss is a function of time only and therefore the loss is greater for the city cycle as the driving time during the city cycle is 71 % greater than the highway cycle due to the increased range of the vehicle. Drivetrain and inverter losses are very similar largely because the energy losses through these components is relatively very small. The braking energy is also very low and

shows little difference between simulations. This is because mechanical braking is only implemented during the first 3 % of the battery SOC until regenerative braking is employed. The hybrid cycle showed values roughly in between the other two cycles, somewhat closer to the city cycle as the average speed was closer to the city cycle (27.6 km/h versus 32.8 km/h).

The graph showing actual vehicle speed and requested vehicle speed indicates a close correlation with very little error. Some overshoot and undershoot was observed however it was limited to sections of rapid acceleration and deceleration. The requested and actual torque values also show good correlation. The battery current was plotted on the same set of axes as torque is directly proportional to current and also to show the effect of regenerative braking. It can be observed that when mechanical braking is employed (when the SOC of the battery is above the charging threshold) the battery current does not fall below zero. However, when a negative motor torque is requested, the battery current turns negative which indicates a flow of energy into the battery.

The highway WLTP cycle, which is the legislative cycle, had the shortest simulation time due the large constant speed sections of the model and the variable step solver employed. The other two cycles, which simulated highly transient cycles, had significantly longer simulation times. Simulations were run on a laptop PC with an Intel Core i7 2.60 GHz processor with 16.0 GB RAM. Therefore, the model can be simulated on high performance computers usually available to vehicle designers to decrease simulation time significantly. A highway drive cycle was also run with an increased time step of 0.0005 which resulted in the same predicted range however only a small reduction in simulation time due to the use of a variable solver.

The weight of the vehicle was increased by 50 % over a highway drive cycle to show the effect of the vehicle's mass on range. This provides an example of how the model might be used to optimise the design of the EV by assessing how changes in the design, such as reducing the vehicle's mass, would affect the energy efficiency of the vehicle. As expected, the rolling resistance losses increased due the increase in weight, which caused a decrease in the range of 14.6 %.

5.3 Limitations and future research

The model does not consider temperature, in line with the aims of simulating regular driving conditions and not harsh/high acceleration driving conditions. This was shown to be true for all three WLTP drive cycles as the requested torque never exceeded the maximum continuous rating of the motor. Inclusion of temperature in the model will allow the designer to simulate the vehicle under all driving conditions and can provide other important information beyond the aims of this

work. Modelling temperature will aid in understanding how the vehicle will perform in different climates, which may be especially important in considering colder climates where the temperature drops below freezing. Inclusion of temperature would also allow the designer to asses and design thermal management systems.

The effect of wind might also be considered in future models to improve the accuracy of the aerodynamic losses. Although wind is highly unpredictable, it has a significant effect on the aerodynamic drag of the vehicle which was shown to have significant effect on the overall energy consumption of the vehicle. Inclusion of the effect of wind speed into the aerodynamic model can be implemented easily, however determining the actual wind speed and direction versus time profile would require a comprehensive investigation into the average wind speed which would vary based on location and weather conditions.

The motor block considers only a PMSM motor operating up to its base speed. In reality some vehicles may operate above the base speed of the motor, especially if a gearbox is used. In these cases the core losses due to eddy and hysteresis must be considered. Typically, this is achieved using experimental techniques to determine the coefficients of an empirical approximation. Therefore an approach should be investigated which allows for the losses to be estimated without experimental testing.

Once the Mamba has been fully tested for safety and has received its road-worthiness certificate, it is intended that the vehicle be tested and the data compared to that predicted by the model developed in this work. Each sub-model within the model developed has already been validated against modelling methods proven in literature; but it is necessary to later validate the model as a whole by comparing it to a real-life system. This is expected to be achieved by recording time, vehicle speed, altitude and wind speed and direction whilst the car is driven along a given route. This physical route data can then be inputted to the model to compare the simulated range against the actual measured range, among other parameters. Some inaccuracy can be expected since the model will not perfectly capture all environmental factors, such as instantaneous wind speed and direction; and if the driver relies on mechanical braking instead of regenerative braking even when the SOC is below the threshold, there will be further inaccuracy if the model is not adjusted to account for this (note that this is not required for standardised drive cycles). The model in its current form is expected to predict relevant parameters, particularly range, to a degree of accuracy entirely acceptable for its purpose, assisting in the design and optimisation of battery electric vehicles.

CHAPTER 6: CONCLUSION

As the impetus to reduce the impact of the transport sector on the environment reaches critical levels, EVs are enjoying increasing popularity. This popularisation is driving the need for design tools and methods to ensure successful EV designs. At the core of a successful and commercially viable EV design, is the management of the energy consumption and efficiency of the EV to ensure the battery energy is used to its fullest. To this end, the simulation of EVs is a critical requirement to ensuring these objectives are met.

The energy model developed in this work is able to assist vehicle designers with this task early in the design process, from design inception and improvement to prototype manufacture. A comprehensive literature survey was completed at the start of this work in order to assess the mechanisms of energy losses in an EV and current methods used to model and simulate these losses. This ensured that the developed model of the EV captures all energy losses in an efficient and accurate manner.

A significant advantage of the model is that it relies almost entirely on datasheet values or non-proprietary values that can be obtained from the manufacturer and therefore no experimental testing is required. This allows vehicle designers to make design decisions before the procurement of components which ensures that the components selected and the topology and architecture of the EV can be fully optimised throughout the design process.

The model was also built on a robust and efficient physical modelling platform, Simscape™, using a dynamic physics based modelling approach. It was developed using mostly custom coded blocks to guarantee complete flexibility in the design and construction of the model. Although the model was built principally to simulate the Mamba EV it was ensured the model was universal, allowing a designer to assess a variety of components and topologies and to ensure the model can be used by other EV designers. Simscape™ is a universal and well documented modelling tool which also allows for the model to be improved and adapted where required in future iterations. The computational cost of the model was optimised without jeopardising the fidelity of the model through the use of an average value inverter and a variable time step solver.

The model was used to simulate the Mamba EV and the acquisition of all its parameters was discussed at length as a means of satisfying the parameter acquisition requirements. The results evidenced that the model was able to produce the require metrics set out in the objectives of this work. The model was able to quantify the range of the vehicle, the relative magnitude of each of

the energy losses, as well as capturing the dynamics of important metrics such as battery voltage and current and motor torque and power.

The simulations of the Mamba EV showed an official range of 285.3 km according to the legislative WLTP drive cycle which simulates highway driving. The city version of the cycle resulted in a significantly increased rang of 420.8 km due to the lower aerodynamic losses and the ability to recover braking energy through regenerative braking. The simulations were also able to provide a comprehensive summary of the relative magnitudes of each energy loss mechanism over each drive cycle in order to best assess how to mitigate energy losses to improve vehicle efficiency.

The developed energy model has a variety of applications and uses for the EV designer. Vehicle designers can efficiently compare different components to determine and compare the effect on vehicle energy efficiency in conjunction with comparing different drivetrain topologies and architectures. The relative magnitude of each energy loss throughout a drive cycle can also be assessed to determine which energy losses are most important to mitigate. The range of the vehicle can be simulated against legislative drive cycles to predict the range of the vehicle that will be advertised by the EV manufactures. The model can also be used to tune PID parameters and develop control strategies as it employs a dynamic physics based approach which also allows for HIL implementation. The model can therefore be considered an invaluable tool for EV design and in ensuring that the energy efficiency of newly designed EVs is maximised.

APPENDIX A: SIMSCAPE™ CODE

A.1 Rotational dynamics

```
component Rotational_dynamics
%Rotational Dynamics
%Models rotational dynamics of the drivetrain.

nodes
    M = foundation.mechanical.rotational.rotational;    %R: left
    C = foundation.mechanical.rotational.rotational;    %C: left
    Wh = foundation.mechanical.rotational.rotational;   %Wh: right
end

parameters
    J_as = {0, 'kg*m^2'};           %Axle shaft rotational inertia
    J_wh = {0, 'kg*m^2'};           %Wheel rotational inertia
    J_df = {0, 'kg*m^2'};           %Differntial rotational inertia
    J_gb = {0, 'kg*m^2'};           %Gearbox rotational inertia
    G_df = {1, '1'};                %Differntial ratio
    G_gb = {1, '1'};                %Gearbox ratio
    N_as = {1, '1'};                %Axle shaft efficiency
    N_df = {1, '1'};                %Differntial efficiency
    N_gb = {1, '1'};                %Gearbox efficiency
    N_cl = {1, '1'};                %Clutch efficiency
    init_pos = {0, 'rad'};          %Initial rotor position
end

inputs
    T_b = {0, 'N*m'};               %Tb: right
end

outputs
    A = {0, 'rad'};                 %th: left
end

variables (Access = protected)
    w_m = {0, 'rad/s'};             %Motor angular speed
    theta_m = {0, 'rad'};           %Motor angular position
    t_m = {0, 'N*m'};               %Motor torque
    t_wh = {0, 'N*m'};              %Wheel torque
end

function setup
    theta.value = init_pos;
    theta.priority = priority.high;
end

branches
    t_m : M.t -> C.t;
    t_wh : C.t -> Wh.t;
end

equations
    let
       G_total = G_gb*G_df;
       N_total = N_cl*N_gb*N_df*N_as;
       J_total = J_gb*G_total*N_gb*N_df + J_df*N_df +
      (J_as +  J_wh)/G_total;
```

```
55          in
56             Wh.w == G_total*M.w;
57             w_m == M.w - C.w;
58             if t_m > 0
59             t_wh == G_total*N_total*t_m - J_total*w_m.der + T_b;
60             else
61             t_wh == G_total*1/N_total*t_m - J_total*w_m.der + T_b;
62             end
63             w_m == theta_m.der;
64             A == theta_m;
65          end
66       end
67       end
```

A.2 Longitudinal dynamics

```
component Longitudal_dynamics
    %Longitudinal Dynamics
    %A two axle vehicle model considering longitudinal dynamics of a
     vehicle.

    parameters
        m = {1000, 'kg'};           %Vehicle mass
        f = {1.5, 'm'};             %Distance from COM to front axle
        r = {1.5, 'm'};             %Distance from COM to rear axle
        h = {0.4, 'm'};             %Height of COM above ground plane
        P = {2, 'bar'};             %Tyre inflation pressure
        a = {1.1e-1, '1'};          %J2452 coefficient - a
        b = {2.5e-4, '1'};          %J2452 coefficient - b
        c = {8.7e-7, '1'};          %J2452 coefficient - c
        alpha = {3.8e-1, '1'};      %J2452 coefficient - alpha
        beta = {-9.4e-1, '1'};      %J2452 coefficient - beta
        rho = {1.25, 'kg*m^-3'};    %Air density
        Cd = {0.4, '1'};            %Drag coefficient
        Af = {1.5, 'm^2'};          %Frontal area
    end

    nodes
       Fd = foundation.mechanical.translational.translational; %Fd: left
       G = foundation.mechanical.translational.translational;  %G: right
    end

    outputs
        Vx = {0, 'm/s'};        %vx: right
        Sx = {0, 'm'};          %sx: right
    end

    inputs
        e = {0, 'rad'};         %Inc[rad]: left
    end

    variables
        fd = {0, 'N'};          %Driving force
        vx = {0, 'm/s'};        %Vehicle speed
        sx = {0, 'm'};          %Vehicle displacement
        fte = {0, 'N'};         %Tractive effort
        frr_f = {0, 'N'};       %Rolling resistance (front wheels)
        frr_r = {0, 'N'};       %Rolling resistance (rear wheels)
        frr = {0, 'N'};         %Total rolling resistance
        fad = {0, 'N'};         %Aerdoynamic drag
        fhc = {0, 'N'};         %Hill climbing force
        fzf = {0, 'N'};         %Normal forces (front wheels)
        fzr = {0, 'N'};         %Normal forces (rear wheels)
        vx_kph = {0, '1'};      %Velocity [km/h]
    end

    function setup
        vx.value = 0;
        vx.priority = priority.high;
        sx.value = 0;
        sx.priority = priority.high;
```

```
55          end
56
57          branches
58              fd: Fd.f -> G.f
59          end
60
61          equations
62              let
63                  g = {9.81, 'm/s^2'};
64                  l = f+r;
65              in
66                  fhc == m*g*sin(e);
67                  fzf == m*g*((r/l)*cos(e) - (h/l)*sin(e)) - (fd-fte)*h/l;
68                  fzr == m*g*((f/l)*cos(e) + (h/l)*sin(e)) + (fd-fte)*h/l;
69                  vx_kph == {value(vx, 'km/hr'), '1'};
70                  frr_f == {(value(P, 'kPa')^alpha) * (value(fzf, 'N')^beta) *
                    (a + b*vx_kph + c*vx_kph^2), 'N'};

71                  frr_r == { (value(P, 'kPa')^alpha) * (value(fzr, 'N')^beta) *
                    (a + b*vx_kph + c*vx_kph^2), 'N'};

72                  if vx > 0
73                      frr == frr_r + frr_f;
74                  else
75                      frr ==0;
76                  end
77                  fad == (rho*Cd*Af)/2 * vx^2;
78
79                  fd == m*vx.der + fte;
80                  vx == Fd.v - G.v;
81                  fte == fhc + fad + frr;
82                  vx == Vx;
83                  vx == sx.der;
84                  sx == Sx;
85              end
86          end
87      end
```

A.3 Motor

```
component Motor
    %PMSM Motor
    %Models a non-salient PMSM motor operating below base speed
     including bearing friction and rotor dynamics

    parameters
      N = {12, '1'};                    %Number of pole pairs
      Rs = {9e-3, 'Ohm'};               %Stator resistance - line?
      L = {0.14e-3, 'H'};               %Stator Inductance
      Lamda_f = {60, 'Wb'};             %Permanent magnet flux linkage
      B_m = {2.7e-5, '(N*m)*s/rad'};    %Motor viscous friction
      J_r = {0, 'kg*m^2'};            %Motor (rotor) rotational inertia
    end

    nodes
        u = foundation.electrical.electrical;              %u:left
        v = foundation.electrical.electrical;              %v:left
        w = foundation.electrical.electrical;              %w:left
        n = foundation.electrical.electrical;              %n:left
        R = foundation.mechanical.rotational.rotational    %R:right
        C = foundation.mechanical.rotational.rotational    %C:right
    end

    variables
        vU = {0, 'V'};              %U phase voltage
        vV = {0, 'V'};              %V phase voltage
        vW = {0, 'V'};              %W phase voltage
        omega = {0, 'rad/s'};       %Angular velocity
        iU = {0, 'A'};              %U phase current
        iV = {0, 'A'};              %V phase current
        iW = {0, 'A'};              %W phase current
        T_m = {0, 'N*m'};           %Motor torque
        id = {0, 'A'};              %d axis current
        iq = {0, 'A'};              %d axis current
        vd = {0, 'V'};              %d axis voltage
        vq = {0, 'V'};              %q axis voltage
        theta = {0, 'rad'};         %Rotor position
    end

    variables(Access = protected)
        v0 = {0, 'V'};
        i0 = {0, 'A'};
    end

    branches
        iU: u.i -> n.i;
        iV: v.i -> n.i;
        iW: w.i -> n.i;
        T_m: C.t -> R.t;
    end

    equations
        let
            lamda = sqrt(3/2)*Lamda_f;
            L0=0.1*L;
        in
            vU == u.v - n.v;
```

```
57              vV == v.v - n.v;
58              vW == w.v - n.v;
59              omega == R.w - C.w;
60
61              omega == theta.der;
62              T_m == N*lamda*iq - B_m*omega - omega.der*J_r
63
64              vd == sqrt(2/3)*(vU*cos(N*theta) + vV*cos(N*theta -
                (2*pi/3)) + vW*cos(N*theta+(2*pi/3)));
65              vq == sqrt(2/3)*(-vU*sin(N*theta) - vV*sin(N*theta -
                (2*pi/3) - vW*sin(N*theta+(2*pi/3)));
66              v0 == sqrt(1/3)*(vU + vV +vW);
67
68              L*iq.der == vq-Rs*iq - N*omega*(L*id+lamda);
69              L*id.der == vd-Rs*id + N*omega*L*iq;
70              L0*i0.der == v0-Rs*i0;
71
72              iU == sqrt(2/3)*(id*cos(N*theta)-iq*sin(N*theta)
                + (i0/sqrt(2)));
73              iV == sqrt(2/3)*(id*cos(N*theta-(2*pi/3))-
                iq*sin(N*theta-(2*pi/3)) + (i0/sqrt(2)));
74              iW == sqrt(2/3)*(id*cos(N*theta+(2*pi/3))
                -iq*sin(N*theta+(2*pi/3)) + (i0/sqrt(2)));
75          end
76      end
77  end
```

A.4 MPTA controller

```
component MTPA_controller
%MTPA controller
%This block generates a three phase AC voltage command for a three phase inverter to power a non-salient PMAC motor below base speed.

parameters
    N = {6, '1'};               %Number of pairs of rotor poles
    lamda_f = {30e-3, 'Wb'};    %Flux linkage induced by rotor magnets
    kp = {60, 'Ohm'};           %PI control - Proprtional gain
    ki = {3000, 'Ohm/s'};       %PI control - Integral gain
end

outputs
    vU_ref = {0.0, 'V'};        %u*: right
    vV_ref = {0.0, 'V'};        %v*: right
    vW_ref = {0.0, 'V'};        %w*: right
end

inputs
    iUVW = {[0,0,0], 'A'};      %I: right
    Tm_ref = {0, 'N*m'};        %Tm*: left
    theta = {0, 'rad'};         %th: left
    v_dc = {0, 'V'};            %Vdc: right
end

variables (Access = protected)
  xd = {value={0, 'A*s'},priority=priority.high};%d-axis integral error
  xq = {value={0, 'A*s'},priority=priority.high};%q-axis integral error
  vq_ref = {0, 'V'};
end

equations
    let
       id = sqrt(2/3)*(iUVW(1)*cos(N*theta) +
       iUVW(2)*cos(N*theta-(2*pi/3))+ iUVW(3)*cos(N*theta+(2*pi/3)));
       iq = sqrt(2/3)*(-iUVW(1)*sin(N*theta) -
       iUVW(2)*sin(N*theta-(2*pi/3)) - iUVW(3)*sin(N*theta+(2*pi/3)));

       id_ref = {0, 'A'};
       iq_ref={sqrt(2/3)*value(Tm_ref,'N*m')/
       (value(lamda_f,'Wb')*N),'A'};

        vd_ref = -kp*(id-id_ref) - ki*xd;
        vq_ref_ = -kp*(iq-iq_ref) - ki*xq;

        v_lim = v_dc/sqrt(2/3);

    in

        xd.der == (id-id_ref);
        xq.der == (iq-iq_ref);

        if vq_ref_ >= v_lim
        vq_ref == v_lim;
        elseif vq_ref_ <= -v_lim
        vq_ref == -v_lim;
        else
        vq_ref == vq_ref_;
```

```
55              end
56
57              vU_ref == sqrt(2/3)*(vd_ref*cos(N*theta) -
                vq_ref*sin(N*theta));
58              vV_ref == sqrt(2/3)*(vd_ref*cos(N*theta-(2*pi/3))
                -  vq_ref*sin(N*theta-(2*pi/3)));
59              vW_ref == sqrt(2/3)*(vd_ref*cos(N*theta+(2*pi/3))
                - vq_ref*sin(N*theta+(2*pi/3)));
60
61          end
62      end
63      end
```

A.5 Inverter

```
component Inverter
%Three Phase Inverter
%Average value inverter transforming a direct current to a 3 phase AC
current with according to a reference 3 phase voltage.

parameters
    R_on = {9.7e-3, 'Ohm'};         % MOSFET/IGBT on-state resitance
    P_sw = {20, 'W'};               % Switching power losses
end

inputs
    vU_ref = {0.0, 'V'};    %u*: left
    vV_ref = {0.0, 'V'};    %v*: left
    vW_ref = {0.0, 'V'};    %w*: left
end

nodes
    p = foundation.electrical.electrical;   %B+: left
    n = foundation.electrical.electrical;   %B-: left
    u = foundation.electrical.electrical;   %u: right
    v = foundation.electrical.electrical;   %v: right
    w = foundation.electrical.electrical;   %w: right
end

variables
    iU = {0, 'A'};                                  %U phase current
    vU = {0, 'V'};                                  %U phase voltage
    iV = {0, 'A'};                                  %V phase current
    vV = {0, 'V'};                                  %V phase voltage
    iW = {0, 'A'};                                  %W phase current
    vW = {0, 'V'};                                  %W phase voltage
    idc = {0, 'A'}                                  %DC side current
    P_sw_ = {0, 'W'};
end

function setup
    vcap = v0;
end

branches
    idc: p.i -> n.i;
    iU: n.i -> u.i;
    iV: n.i -> v.i;
    iW: n.i -> w.i;
end

equations
    vdc == p.v - n.v;

    vU == u.v - n.v;
    vU == vU_ref;
    vV == v.v - n.v;
    vV == vV_ref;
    vW == w.v - n.v;
    vW == vW_ref;

```

```
56          if idc > 0
57              P_sw_ == P_sw
58          elseif idc < 0
59              P_sw_ == -P_sw;
60          else
61              P_sw_ == 0
62          end
63
64          vdc*idc == (vU*iU + R_on*iU^2 + vV*iV + R_on*iV^2 + vW*iW +
            R_on*iW^2)+ vdc*icap + P_sw_;
65
        end
66      end
```

A.6 Auxiliary load

```
component Auxiliary_load
%Auxiliary load
%Models high voltage auxiliary loads and low voltage auxiliary loads
powered through a DC/DC buck converter

parameters
    P_HV = {100, 'W'};      %HV Auxiliary Power
    P_LV = {100, 'W'};      %LV Auxiliary Power
    N_conv = {92, '1'};     %DC/DC converter efficiency %
end

nodes
    p = foundation.electrical.electrical;   %B+: right
    n = foundation.electrical.electrical;   %B-: right
end

variables
    i_aux = {0, 'A'};
    vdc = {0, 'V'};
end

branches
    i_aux: p.i -> n.i;
end

equations
    vdc == p.v - n.v;

    if value(time, 's')>1.0
        i_aux == (P_LV/vdc)/(N_conv/100) + (P_HV/vdc);
    else
        i_aux == 0;
    end
end
end
```

A.7 Torque limiter

```
component Torque_limiter
%Negative torque limiter
%Limits negative motor torque when vehicle speed drops below zero and
when SOC is above its limit.

parameters
    SOC_lim = {0.9, '1'};       %Maximum SOC at which regen is possible
end

inputs
    vx = {0, 'm/s'};             %vx: right
    Tm_ref_r = {0, 'N*m'};       %Tm_r: right
    SOC = {0, '1'};              %SOC: left
end

outputs
    Tm_ref = {0, 'N*m'};         %Tm*:left
    Tb = {0, 'N*m'};             %Tb:left
end

equations
    if Tm_ref_r > 0
        Tb == 0;
        Tm_ref == Tm_ref_r;
    elseif Tm_ref_r < 0 && vx >= 0 && SOC < SOC_lim
        Tb == 0;
        Tm_ref == Tm_ref_r;
    elseif Tm_ref_r < 0 && vx >= 0 && SOC > SOC_lim
         Tb == Tm_ref_r;
         Tm_ref == 0;
    else
        Tb == 0;
        Tm_ref == 0;
    end
end
end
```

A.8 Parameter initialisation

```
% PARAMETER INITIALISATION

%Linear Dynamics
m = 657;                          %Vehicle mass [kg]
f = 1.2563;                       %Distance from COM to front axle [m]
r = 1.0937;                       %Distance from COM to rear axle [m]
h = 0.3809;                       %Height of COM above ground plane [m]
P = 2.5;                          %Tyre inflation pressure [bar]
a = 1.11e-1;                      %J1269 coefficient - a
b = 2.53e-4;                      %J1269 coefficient - b
c = 8.67e-7;                      %J1269 coefficient - c
alpha = -0.388;                   %J1269 coefficient - alpha
beta = 9.40e-1;                   %J1269 coefficient - beta
rho = 1.25;                       %Air density [kg/m^3]
Cd = 0.33725;                     %Drag coefficient
Af = 1.55;                        %Frontal area [m^2]

%Rotational Dynamics
Jas = 6.15e-4;                   %Axle shaft rotational inertia [kg*m^2]
Jwh = 1.06;                       %Wheel rotational inertia [kg*m^2]
Jdf = 0;                         %Differntial rotational inertia [kg*m^2]
Jgb = 0;                          %Gearbox rotational inertia [kg*m^2]
Gdf = 1;                          %Differntial ratio
Ggb = 1;                          %Gearbox ratio
Ndf = 1;                          %Differntial efficiency
Ngb = 1;                          %Gearbox efficiency
Ncl = 1;                          %Clutch efficiency
Nas = 0.995;                      %Axle shaft efficiency
th0 = 0;                          %Initial rotor position [rad]
R_wh = 0.3172;                    %Wheel radius [m]

% Drive Cycle
time = xlsread('WLTP Full.xlsx', 'Time');
speed = xlsread('WLTP Full.xlsx', 'Speed');

%Driver
Kp = 200;                         %Speed PID control - Proprtional gain
Ki = 100;                         %Speed PID control - Integral gain
Kd = 25;                          %Speed PID control - Derivative gain
Tm_max = 400;                     %Maximum motor torque [Nm]
Tg_max = 400;                     %Maximum regeneration torque [Nm]
SOC_regen = 0.96;                 %SOC regen limit

%MTPA Torque Controller
kp = 80;                          %PI control - Proprtional gain
ki = 1000;                        %PI control - Integral gain

%Inverter
Ron = 9.7e-3;                     %MOSFET/IGBT on-state resistance [Ohm]
Psw = 40;                         %Switching power loss [W]

%Motor
N = 12;                           %Number of pairs of rotor poles
lamda_f = 0.11367;                %Permanent magnet flux linkage [Wb]
L = 0.0875e-3;                    %Inductance [H]
Rs = 0.0544;                      %Stator phase resistance [Ohm]
Bm = 0.005;                      %Viscous friction coefficient [Nm/rad/s]
```

```
Jm = 368479.77e-6;              %Rotor rotational inertia [kg*m^2]

%Battery
R_series = 0.019;                %Equivalent series resistance [Ohm]
R_trans_short = 0.012;           %Transient resistance (short) [Ohm]
R_trans_long = 0.012;            %Transient resistance (long) [Ohm]
C_trans_short = 700;             %Transient capacitance (short) [Ohm]
C_trans_long = 4500;             %Transient capacitance (long) [Ohm]
a0 = 3.278;                      %OCV versus SOC curve coefficient - a
a1 = 0.2279;                     %OCV versus SOC curve coefficient - b
a2 = -0.7642;                    %OCV versus SOC curve coefficient - c
a3 = -49;                        %OCV versus SOC curve coefficient - d
C_nom = 2.9;                     %Nominal cell capacity [Ah]
Ns = 42;                         %Number of cells in series
Np = 48;                         %Number of cells in parallel
V_min = 2.55;                    %End of discharge cell voltage [V]

%Auxiliary load
P_hv = 100;                      %HV Auxiliary Power [W]
P_lv = 0;                        %LV Auxiliary Power [W]
N_conv = 92;                     %DC/DC converter efficiency [%]

%Cable losses
L_batt = 8;                    %Total battery cable length [m]
CSA_batt = 95e-6;              %Battery cable cross sectional area [m^2]
L_motor = 0.8;                 %Motor cable length (total per phase) [m]
CSA_motor = 16e-6;             %Motor cable cross sectional area [m^2]
Rho_cu = 1.68e-8;               %Copper resistivity [Ohm*m]
```

APPENDIX B: MODELLING EQUATIONS

Rotational dynamics:

$$T_{gb} = \left(T_{cl} - J_{gb}\frac{\dot{\omega}_m}{G_{gb}}\right) \cdot \eta_{gb} G_{gb} \quad \text{Equation 2.5}$$

$$\omega_{gb} = \frac{\omega_m}{G_{gb}} \quad \text{Equation 2.6}$$

$$T_{wh} = G_{total}\,\eta_{total} T_m - J_{total}\,\dot{\omega}_m + T_b \quad \text{Equation 2.7}$$

$$J_{total} = J_{gb} G_{total}\,\eta_{gb}\,\eta_{df} + J_{df}\,\eta_{df} + \frac{J_{as} + J_{wh}}{G_{total}} \quad \text{Equation 2.8}$$

$$\eta_{total} = \eta_{cl}\,\eta_{gb}\,\eta_{df}\,\eta_{as} \quad \text{Equation 2.9}$$

$$G_{total} = G_{gb} G_{df} \quad \text{Equation 2.10}$$

Longitudinal dynamics

$$F_d = \frac{T_{wh}}{R_{wh}} \quad \text{Equation 2.11}$$

$$m\dot{v_x} = F_d - F_{te} \quad \text{Equation 2.12}$$

$$F_{hc} = mg \cdot sin(\epsilon) \quad \text{Equation 2.14}$$

$$F_{zf} = \frac{mg}{f+r}\left(r \cdot cos(\in) - h \cdot sin(\in)\right) - \frac{ma \cdot h}{f+r} \quad \text{Equation 2.15}$$

$$F_{zr} = \frac{mg}{f+r}\left(f \cdot cos(\in) + h \cdot sin(\in)\right) + \frac{ma \cdot h}{f+r} \quad \text{Equation 2.16}$$

Rolling resistance

$$F_{rr} = C_{RR} \cdot F_Z \quad \text{Equation 2.20}$$

$$F_{rr} = P^{\alpha} {F_Z}^{\beta}(a + b v_x + c {v_x}^2) \quad \text{Equation 2.21}$$

Aerodynamics

$$F_{ad} = \frac{\rho_{air} C_d A_f}{2} \cdot (v_x \pm v_{wind})^2 \quad \text{Equation 2.23}$$

Motor

$$P_{Core} = k_{eddy}{f_m}^2 B^2 + k_{hyst} f_m B^2 + k_{ex}{f_m}^{1.5} B^{1.5}$$ Equation 2.24

$$u_q(t) = R_s i_q(t) + \frac{d\lambda_{qs}}{dt} + \omega_r \lambda_{ds}$$ Equation 2.26

$$u_d(t) = R_s i_d(t) + \frac{d\lambda_{ds}}{dt} - \omega_r \lambda_{qs}$$ Equation 2.27

$$\lambda_{ds} = L_d i_d + \lambda_f, \lambda_{qs} = L_q i_q$$ Equation 2.28

$$T_{em} = \frac{3N}{2}\left[\lambda_f i_q + (L_d - L_q) i_d i_q\right]$$ Equation 2.29

$$L_d = L_q = \frac{L_{line(uvw)}}{2}$$ Equation 2.30

MTPA Controller

$$T_{em} = \frac{3N}{2}\left[\lambda_f i_q + (L_d - L_q) i_d i_q\right]$$ Equation 2.29

$$V_{phase,max} = \frac{V_{Batt}}{\sqrt{3}}$$ Equation 2.33

Inverter

$$P_{con} = \frac{1}{T_p}\int_0^{t_{con}} \left(R_{on} \cdot i_{drain}^2(t)\right) dt$$ Equation 2.34

$$P_{sw} = \frac{E_{sw,r}}{T_p} \cdot \frac{V}{V_r} \cdot \frac{I}{I_r}$$ Equation 2.36

Battery

$$C_{Capacity} = 3600 \times C_N \times f_1(cycle) \times f_2(temp)$$ Equation 2.38

$$V_{OC}(SOC) = a0 + a1 \times SOC + a2xSOC^2 \ldots$$ Equation 2.44

APPENDIX C: SIMSCAPE™ IMAGES

C.1 Battery

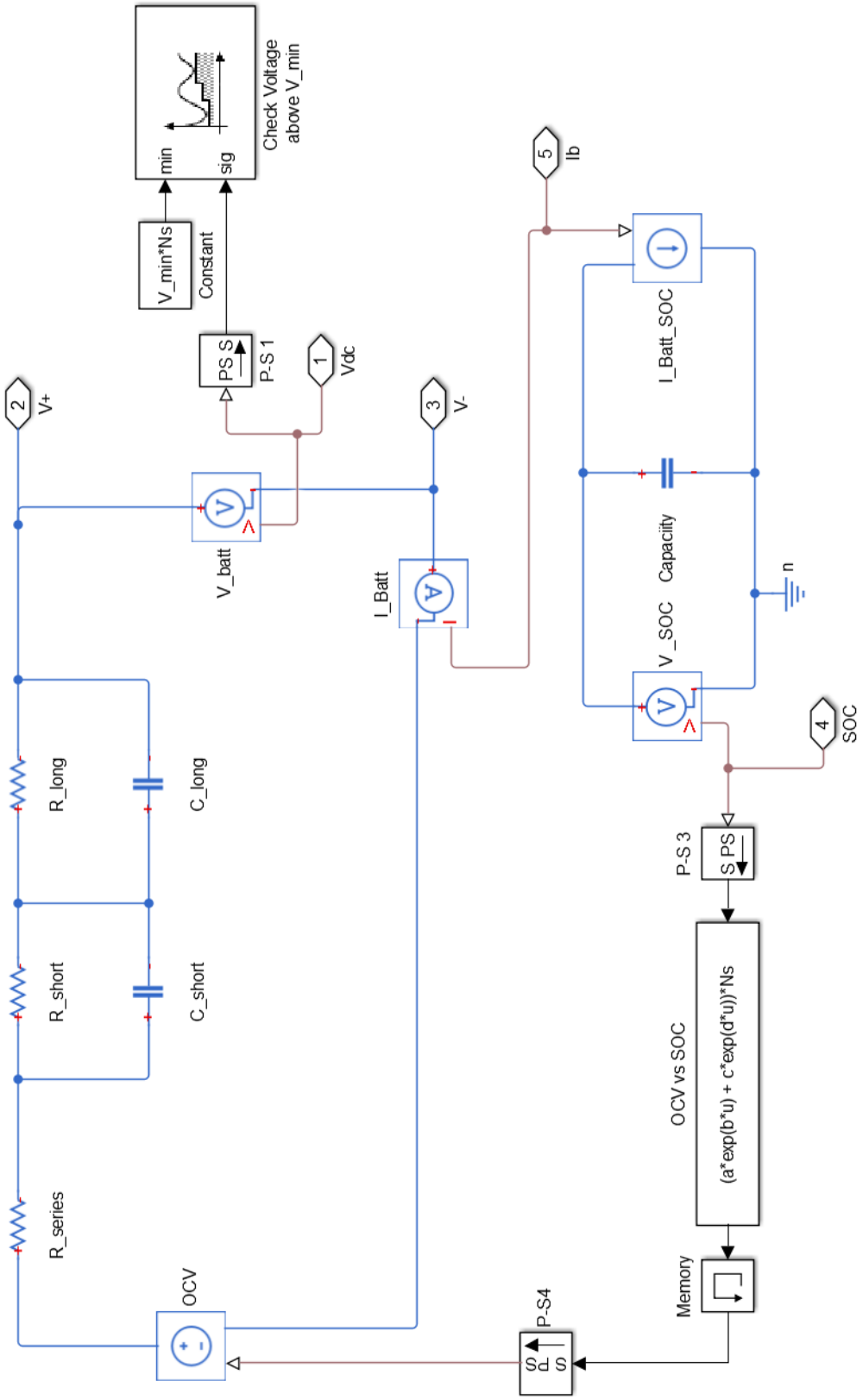

C.2 Driver model and drive cycle

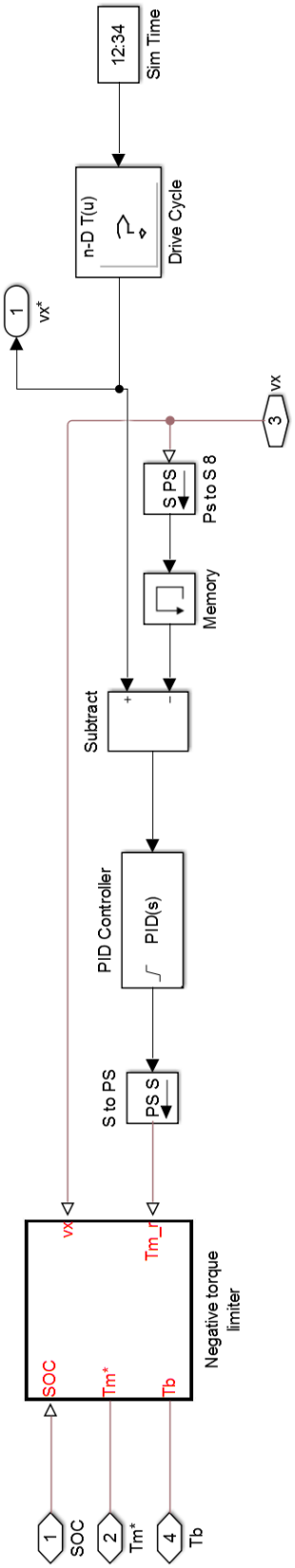

C.3 Mamba EV model

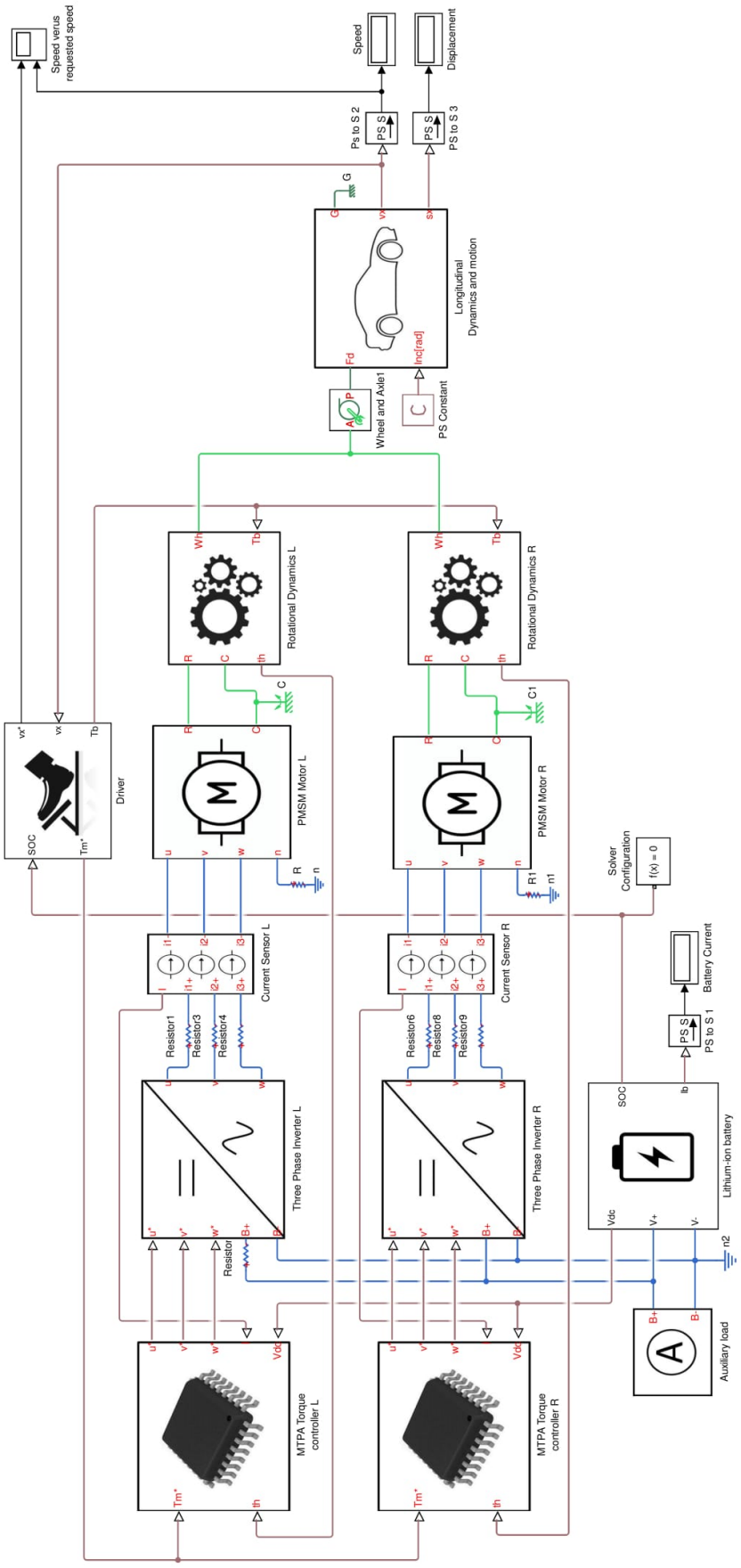

APPENDIX D: OCV CURVE FITTING

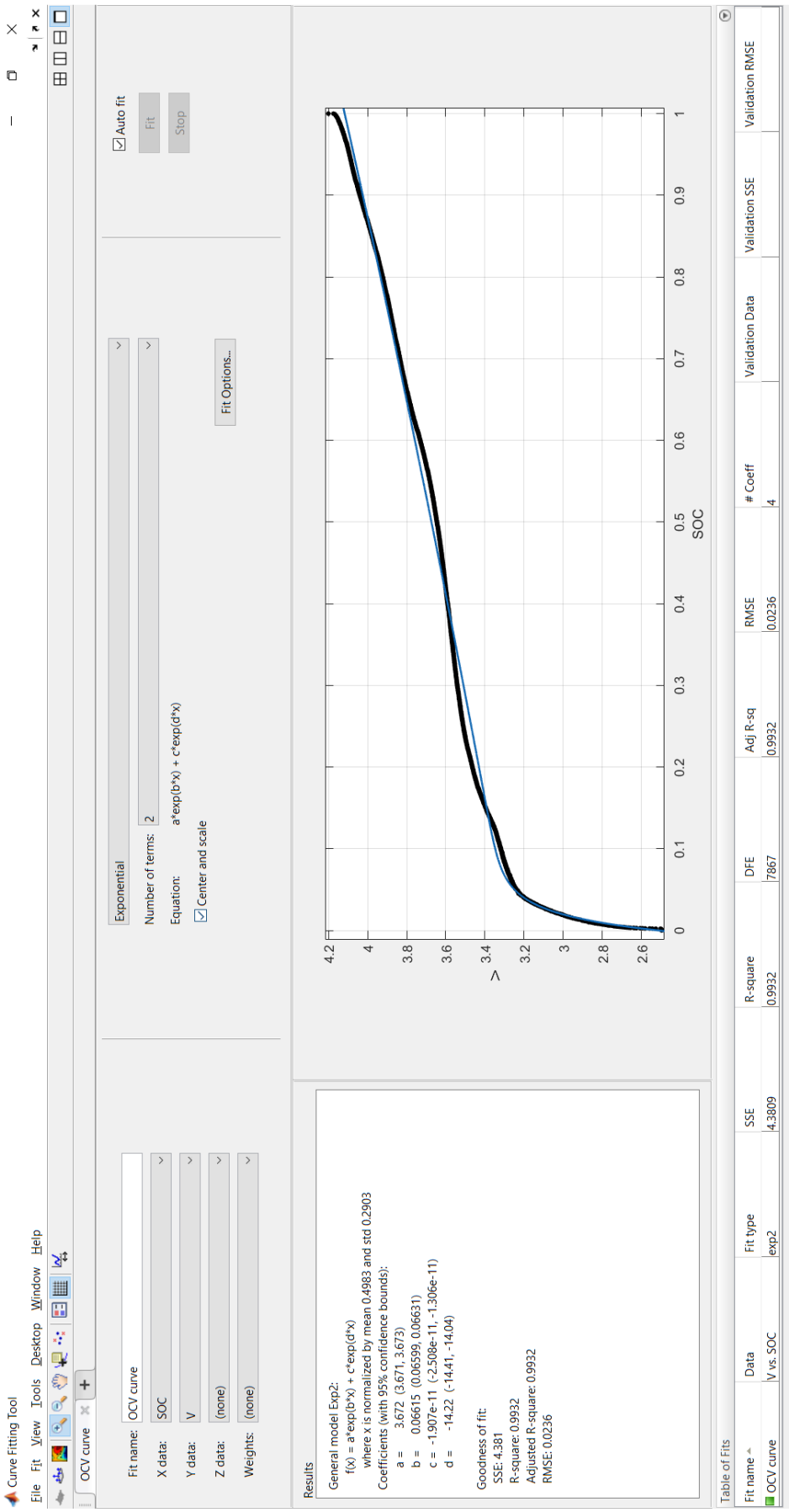

REFERENCES

Allen, M. (2014). Real-world range ramifications: Heating and air conditioning. Retrieved from http://www.fleetcarma.com/electric-vehicle-heating-chevrolet-volt-nissan-leaf/

Altinisik, A., Yemenici, O., & Umur, H. (2015). Aerodynamic analysis of a passenger car at yaw angle and two-vehicle platoon. *Journal of Fluids Engineering, 137*(12), 121107 - 121107/121110. doi: http://dx.doi.org/10.1115/1.4030869

Amjad, S., Rudramoorthy, R., Neelakrishnan, S., Sri Raja Varman, K., & Arjunan, T. V. (2011). Evaluation of energy requirements for all-electric range of plug-in hybrid electric two-wheeler. *Energy, 36*(3), 1623-1629. doi: http://dx.doi.org/10.1016/j.energy.2010.12.069

Automotive Forums. (2017). Rim inertia. Retrieved from http://www.automotiveforums.com/t13944-rim_inertia.html

Avison, J. (1989). *The world of physics* (2nd ed.). United Kingdom: Thomas Nelson and Sons Ltd.

Barlow, T. J., Latham, S., McCrae, I. S., & Boutler, P. G. (2009). *A reference book of driving cycles for use in the measurement of road vehicle emmisions* (Vol. 3). Berkshire: Transport Research Laboratory Limited.

Barreras, J. V., Schaltz, E., Andreasen, S. J., & Minko, T. (2012, 9-12 Oct.). *Datasheet-based modeling of Li-Ion batteries.* Paper presented at the 2012 IEEE Vehicle Power and Propulsion Conference.

Battery University. (2017). BU-402: What Is C-rate? , Retrieved from http://batteryuniversity.com/index.php/learn/article/what_is_the_c_rate

Brady, J., & O'Mahony, M. (2016). Development of a driving cycle to evaluate the energy economy of electric vehicles in urban areas. *Applied Energy, 177*, 165-178. doi: https://doi.org/10.1016/j.apenergy.2016.05.094

Clark, S. K., & Dodge, R. N. (1979). *A Handbook for the rolling resistance of pneumatic tires*. Ann Arbor, Michigan: University of Michigan.

Climateactiontracker.org. (2016). The road ahead: How do we move to cleaner car fleets. Retrieved from

http://climateactiontracker.org/assets/publications/briefing_papers/CAT_Decarb_Transport.pdf

Cunningham, E. (2017). Concerns new emissions test will push up road tax costs. Retrieved from http://www.independent.ie/life/motoring/car-news/concerns-new-emissions-test-will-push-up-road-tax-costs-35673959.html

Dajaku, G., & Gerling, D. (2007, 3-5 May). *The correct analytical expression for the phase inductance of salient pole machines.* Paper presented at the 2007 IEEE International Electric Machines & Drives Conference.

Davis, M. E. (1984). *Numerical methods and modeling for chemical engineers*. New York: John Wiley & Sons.

Day, A. (2014). Chapter 12 - Case Studies in the Braking of Road Vehicles *Braking of Road Vehicles* (pp. 429-451). Oxford: Butterworth-Heinemann.

Donateo, T., Licci, F., D'Elia, A., Colangelo, G., Laforgia, D., & Ciancarelli, F. (2015). Evaluation of emissions of CO2 and air pollutants from electric vehicles in Italian cities. *Applied Energy, 157*, 675-687. doi: http://dx.doi.org/10.1016/j.apenergy.2014.12.089

Dorrell, D. G., Knight, A. M., Popescu, M., Evans, L., & Staton, D. A. (2010, 12-16 Sept.). *Comparison of different motor design drives for hybrid electric vehicles.* Paper presented at the 2010 IEEE Energy Conversion Congress and Exposition.

Elcon. (n.d.). Elcon DC/DC Converter [Manual].

Enertrac Corp. (n.d.). We're wheel motor driven [Datasheet].

Erdinc, O., Vural, B., & Uzunoglu, M. (2009, 9-11 June). *A dynamic lithium-ion battery model considering the effects of temperature and capacity fading.* Paper presented at the 2009 International Conference on Clean Electrical Power.

Eriksson, L., & Nielson, L. (2014). *Modeling and control of engines and drivelines*. United Kingdom: John Wiley and Sons Ltd.

Errol's Tyres. (n.d.). Tyre overall rolling diameter. Retrieved from https://www.errolstyres.co.za/content/tyre-overall-rolling-diameter

Evans, L. R., MacIsaac, J. D., Harris, J. R., Yates, K., Dudek, W., Holmes, J., . . . Salaani, M. K. (2009). *Tire fuel efficiency consumer information program development: Phase 2 – effects of tire rolling resistance levels on traction, treadwear, and vehicle fuel economy (DOT HS 811 154)*. Washington, DC: National Highway Traffic Safety Administration.

Fiori, C., Ahn, K., & Rakha, H. A. (2016). Power-based electric vehicle energy consumption model: Model development and validation. *Applied Energy, 168*, 257-268. doi: http://dx.doi.org/10.1016/j.apenergy.2016.01.097

Fujii, K., & Fujimoto, H. (2007, 2-5 April). *Traction Control based on slip ratio estimation without detecting vehicle speed for electric vehicles.* Paper presented at the 2007 Power Conversion Conference - Nagoya.

Fujio, T. (2013). Next-generation high efficiency fixed type constant velocity joint "CFJ" [Technical review]. Retrieved from http://www.ntnglobal.com/en/products/review/pdf/NTN_TR81_en_064_067p.pdf

Gao, D. W., Mi, C., & Emadi, A. (2007). Modeling and simulation of electric and hybrid vehicles. *Proceedings of the IEEE, 95*(4), 729-745. doi: http://dx.doi.org/10.1109/JPROC.2006.890127

Genikomsakis, K. N., & Mitrentsis, G. (2017). A computationally efficient simulation model for estimating energy consumption of electric vehicles in the context of route planning applications. *Transportation Research Part D: Transport and Environment, 50*, 98-118. doi: http://dx.doi.org/10.1016/j.trd.2016.10.014

Goss, J., Mellor, P. H., Wrobel, R., Staton, D. A., & Popescu, M. (2012, 27-29 March). *The design of AC permanent magnet motors for electric vehicles: A computationally efficient model of the operational envelope.* Paper presented at the 6th IET International Conference on Power Electronics, Machines and Drives (PEMD 2012).

Goss, J., Popescu, M., Staton, D., Wrobel, R., Yon, J., & Mellor, P. (2014, 14-18 Sept.). *A comparison between maximum torque/ampere and maximum efficiency control strategies in IPM synchronous machines.* Paper presented at the 2014 IEEE Energy Conversion Congress and Exposition (ECCE).

Graovac, D., Marco Pürschel , & Kiep, A. (2006). MOSFET power losses calculation using the datasheet parameters [Application Note].

Groschopp. (2015). Understanding electric motor efficiency losses. Retrieved from http://www.groschopp.com/blog/efficiency-and-losses-in-electric-motors/

Grover, P. S. (1998). *Modeling of rolling resistance test data*. Paper presented at the International Congress and Exposition, Detroit, Michigan. http://dx.doi.org/10.4271/980251

Guzzella, L., & Sciarretta, A. (2013). *Vehicle propulsion systems: Introduction to modeling and optimization* (3rd ed.). Berlin: Springer-Verlag

Hall, D. E., & Moreland, J. C. (2001). Fundamentals of rolling resistance. *Rubber Chemistry and Technology, 74*(3), 525-539. doi: http://dx.doi.org/10.5254/1.3547650

Hanlei, Z., & Mo-Yuen, C. (2010, 25-29 July). *Comprehensive dynamic battery modeling for PHEV applications.* Paper presented at the IEEE PES General Meeting.

Hassan, W. J. (2011). *Efficiency optimisation of PMSM based drive system.* (Masters), Michigan State University.

Hildebrandt, W., Horst, J., & Rickell, R. A. (2006). New constant velocity fixed joints for front-wheel drivecars. *ATZ worldwide, 108*(5), 2-4. doi: http://dx.doi.org/10.1007/bf03224822

Houcque, D. (n.d.). *Applications of MATLAB™: Ordinary differential equations (ODE)* [Course notes]. Retrieved from https://www.mccormick.northwestern.edu/docs/efirst/ode.pdf

International Council on Clean Transportation. (2013). *World-harmonized light-duty vehicles test procedure (WLTP)* [Policy update]: International Council on Clean Transportation. Retrieved from http://www.theicct.org/sites/default/files/publications/ICCT_PolicyUpdate_WLTP_Nov2013.pdf

Iqbal, A., Lamine, A., Ashraf, I., & Mohibullah. (2006, 6-8 Sept.). *Matlab™/Simulink™ model of space vector PWM for three-phase voltage source inverter.* Paper presented at the Proceedings of the 41st International Universities Power Engineering Conference.

Janssen, M. L., & Hall, G. L. (1980). *Effect of ambient temperature on radial tire rolling resistance*. Paper presented at the Automotive Congress and Exposition, Detroit. http://dx.doi.org/10.4271/800090

Jazar, R. N. (2014). *Vehicle dynamics: Theory and application*. New York: Springer.

Juul, N., & Meibom, P. (2012). Road transport and power system scenarios for Northern Europe in 2030. *Applied Energy, 92*, 573-582. doi: http://dx.doi.org/10.1016/j.apenergy.2011.11.074

Karim, Z. A. A., & Yusoff, A. H. M. (2014). Cooling system for electric motor of an electric vehicle propulsion. *Advanced Materials Research, 903*, 209-214. doi: http://dx.doi.org/10.4028/www.scientific.net/AMR.903.209

Keeping, S. (2013). Selecting the right voltage converter is not just about peak efficiency. Retrieved from https://www.digikey.com/en/articles/techzone/2013/jul/selecting-the-right-voltage-converter-is-not-just-about-peak-efficiency

Kelly Controls. (2015). Kelly KLS8080I/IPS motor controller user's manual [Manual].

Kroeze, R. C., & Krein, P. T. (2008, 15-19 June). *Electrical battery model for use in dynamic electric vehicle simulations.* Paper presented at the 2008 IEEE Power Electronics Specialists Conference.

Kulkarni, S. S., & Thosar, A. G. (2013). Mathematical modeling and simulation of permanent magnet synchronous machine. *International Journal of Electronics and Electrical Engineering, 1*(2), 66-71. doi: http://dx.doi.org/10.12720/ijeee.1.2.66-71

Larminie, J., & Lowry, J. (2013). *Electric vehicle technology explained*. Hoboken, N.J.: Wiley.

Lei, Z., & Hongzhou, J. (2012). *Variable step euler method for real-time simulation*. Paper presented at the 2nd International Conference on Computer Science and Network Technology SP.

Maamoun, A., Alsayed, Y. M., & Shaltout, A. (2010). Space-Vector PWM inverter feeding a permanent-magnet synchronous motor. *International Journal of Electrical, Computer, Energetic, Electronic and Communication Engineering, 41*(5).

MathWorks™. (2014). Simscape [User's Guide].

MathWorks™. (2017a). Basic principles of modeling physical networks. Retrieved from https://www.mathworks.com/help/physmod/simscape/ug/basic-principles-of-modeling-physical-networks.html

MathWorks™. (2017b). Choose a solver. Retrieved from https://www.mathworks.com/help/simulink/ug/types-of-solvers.html

MathWorks™. (2017c). Choose an ODE Solver. Retrieved from https://www.mathworks.com/help/matlab/math/choose-an-ode-solver.html

MathWorks™. (2017d). Permanent Magnet Synchronous Machine. Retrieved from https://www.mathworks.com/help/physmod/sps/powersys/ref/permanentmagnetsynchronousmachine.html

MathWorks™. (2017e). *Simscape Language Guide*. Natick, MA: The MathWorks, Inc.

Mazgaj, W., Rozegnal, B., & Szular, Z. (2015). Switching losses in three-phase voltage source inverters. *Technical transactions: Electrical Engineering, 112*(2-E), 47-60. doi: 10.4467/2353737XCT.15.087.3919

Meier, S. (2001). *Theoretical design of surface-mounted permanent magnet motors with fieldweakening capability.* (Masters), Royal Institute of Technology Stockholm.

Mellor, P. H., Wrobel, R., & Holliday, D. (2009, 3-6 May). *A computationally efficient iron loss model for brushless AC machines that caters for rated flux and field weakened operation.* Paper presented at the 2009 IEEE International Electric Machines and Drives Conference.

Michelin. (2003). *The tyre: Rolling resitance and fuel savings*. Clermont-Ferrand: Société de Technologie Michelin.

Miller, S. L., Youngberg, B., Millie, A., Schweizer, P., & Gerdes, J. C. (2001, 25-27 June). *Calculating longitudinal wheel slip and tire parameters using GPS velocity.* Paper presented at the Proceedings of the 2001 American Control Conference.

Min, C., & Rincon-Mora, G. A. (2006). An accurate electrical battery model capable of predicting runtime and I-V performance. *IEEE Transactions on Energy Conversion, 21*(2), 504-511. doi: http://dx.doi.org/10.1109/TEC.2006.874229

Moler, C. (2011). *Experiments with MATLAB™*. Natick, Massachusetts: Mathworks.

Muenzela, V., Hollenkampb, A. F., Bhattb, A. I., Hoogc, J. d., Brazila, M., Thomasd, D. A., & Mareelsa, I. (2015). A comparative testing study of commercial 18650-format lithium-ion battery cells. *Journal of The Electrochemical Society, 162*(8). doi: 10.1149/2.0721508jes

Nanda, G., & Kar, N. C. (2006, 7-10 May). *A survey and comparison of characteristics of motor drives used in electric vehicles.* Paper presented at the 2006 Canadian Conference on Electrical and Computer Engineering.

Narkhede, Y. (2016). *Simscape modelling of motor-generator unit components for hybrid electric vehicle.* (Masters), Georgia.

National Research Council Transportation Research Board. (2006). *Tires and passenger vehicle fuel economy: Informing consumers, improving performance*. Washington, D.C: Author.

Nelson, P., Bloom, I., Amine, K., & Henriksen, G. (2002). Design modeling of lithium-ion battery performance. *Journal of Power Sources, 110*(2), 437-444. doi: http://dx.doi.org/10.1016/S0378-7753(02)00209-4

Nguyen, A.-T., Reiter, S., & Rigo, P. (2014). A review on simulation-based optimization methods applied to building performance analysis. *Applied Energy, 113*, 1043-1058. doi: http://dx.doi.org/10.1016/j.apenergy.2013.08.061

Ngwangwa, H. M., Heyns, P. S., Breytenbach, H. G. A., & Els, P. S. (2014). Reconstruction of road defects and road roughness classification using Artificial Neural Networks simulation and vehicle dynamic responses: Application to experimental data. *Journal of Terramechanics, 53*, 1-18. doi: http://dx.doi.org/10.1016/j.jterra.2014.03.002

Panasonic. (2013). Introduction of NCR18650PF [Presentation].

Park, G., Lee, S., Jin, S., & Kwak, S. (2014). Integrated modeling and analysis of dynamics for electric vehicle powertrains. *Expert Systems with Applications, 41*(5), 2595-2607. doi: http://dx.doi.org/10.1016/j.eswa.2013.10.007

Petricca, M., Shin, D., Bocca, A., Macii, A., Macii, E., & Poncino, M. (2013, 4-6 Sept.). *An automated framework for generating variable-accuracy battery models from datasheet information.* Paper presented at the International Symposium on Low Power Electronics and Design (ISLPED).

Petro, J. (2011). Achieving high electric motor efficiency. Retrieved from http://www.novatorque.com/aboutus/white-papers/060_John_Petro_final_paper.pdf

Qi, G., Chen, J. T., Zhu, Z. Q., Howe, D., Zhou, L. B., & Gu, C. L. (2008, 17-20 Oct.). *Influence of skew and cross-coupling on d- and q-axis inductances and flux-weakening*

performance of PM brushless AC machines. Paper presented at the 2008 International Conference on Electrical Machines and Systems.

Rabiei, A., Thiringer, T., & Lindberg, J. (2012). *Maximizing the energy efficiency of a PMSM for vehicular applications using an iron loss accounting optimization based on nonlinear programming*. Paper presented at the XXth International Conference on Electrical Machines, Marseille.

Randall, B. (2006). Blowing hot and cold. Retrieved from https://www.tesla.com/blog/blowing-hot-and-cold

Reif, K. (2014). *Fundamentals of automotive and engine technology standard drives, hybrid drives, brakes, safety systems*. Wiesbaden: Springer Vieweg.

Sandberg, U. (2011). *Rolling resistance – basic information and state-of-the-art on measurement methods*. Denmark: Models for rolling resistance In Road Infrastructure Asset Management systems (MIRIAM).

Schuring, D. J., & Futamura, S. (1990). Rolling loss of pneumatic highway tires in the eighties. *Rubber Chemistry and Technology, 63*(3), 315-367. doi: http://dx.doi.org/doi:10.5254/1.3538261

Seaman, A., Dao, T. S., & McPhee, J. (2014). A survey of mathematics-based equivalent-circuit and electrochemical battery models for hybrid and electric vehicle simulation. *Journal of Power Sources, 256*, 410-423. doi: http://dx.doi.org/10.1016/j.jpowsour.2014.01.057

Sim, B., Woods, D., Mons, S., & Chetty, S. (2016). *Electric vehicle design and research project: Second semester report*. Durban: University of KwaZulu-Natal.

Stipetic, S., & Goss, J. (2016, 4-7 Sept.). *Calculation of efficiency maps using scalable saturated flux-linkage and loss model of a synchronous motor.* Paper presented at the 2016 XXII International Conference on Electrical Machines (ICEM).

Tie, S. F., & Tan, C. W. (2013). A review of energy sources and energy management system in electric vehicles. *Renewable and Sustainable Energy Reviews, 20*, 82-102. doi: https://doi.org/10.1016/j.rser.2012.11.077.

Torres, D. (2009). Comparing motor-control techniques. Retrieved from https://www.ecnmag.com/article/2009/10/comparing-motor-control-techniques

Tzirakis, E., Pitsas, K., Zannikos, F., & Stournas, S. (2006). Vehicle emissions and driving cycles: Comparison of the Athens driving cycle (ADC) with ECE-15 and European driving cycle (EDC). *Global NEST, 8*(3), 282-290.

UN Framework Convention on Climate Change. (2016). Landmark climate change agreement to enter into force. Retrieved from http://newsroom.unfccc.int/unfccc-newsroom/landmark-climate-change-agreement-to-enter-into-force/

United Nations. (2015). *Proposal for amendments to global technical regulation No. 15 on Worldwide Harmonized Light vehicles Test Procedure (WLTP)*. Geneva: Author.

United States Environmental Protection Agency. (2014). Global greenhouse gas emissions data. Retrieved from https://www.epa.gov/ghgemissions/global-greenhouse-gas-emissions-data

Vodovozov, V., Raud, Z., Lehtla, T., Rassolkin, A., & Lillo, N. (2014, 25-27 March). *Comparative analysis of electric drives met for vehicle propulsion.* Paper presented at the 2014 Ninth International Conference on Ecological Vehicles and Renewable Energies (EVER).

Vražić, M., Barić, O., & Virtic, P. (2014). Auxiliary systems consumption in electric vehicle. *Przegląd Elektrotechniczny, 12*. doi: http://dx.doi.org/10.12915/pe.2014.12.42

Wei, C., & Taghavifar, H. (2017). A novel approach to energy harvesting from vehicle suspension system: Half-vehicle model. *Energy*, *134*, 279-288. doi: http://dx.doi.org/10.1016/j.energy.2017.06.034

Weng, C., Sun, J., & Peng, H. (2014). A unified open-circuit-voltage model of lithium-ion batteries for state-of-charge estimation and state-of-health monitoring. *Journal of Power Sources, 258*(Supplement C), 228-237. doi: https://doi.org/10.1016/j.jpowsour.2014.02.026

Wieringen, C. v., Gyasi-Agyei, P., & Reddy, A. I. (2017). *Electric vehicle design and research project: Second semester report*. Durban: University of KwaZulu-Natal.

Yeo, H., Kim, D., Hwang, S., & Kim, H. (2004). *Regenerative Braking Algorithm for a HEV with CVT Ratio Control During Deceleration*.

Yildirim, M., Polat, M., & Kürüm, H. (2014, 21-24 Sept.). *A survey on comparison of electric motor types and drives used for electric vehicles.* Paper presented at the 2014 16th International Power Electronics and Motion Control Conference and Exposition.

Young, H. D., & Freedman, R. A. (2012). *University physics* (13th ed.). Essex: Pearson.

Zhang, Y., Guo, K., Wang, D., Chen, C., & Li, X. (2017). Energy conversion mechanism and regenerative potential of vehicle suspensions. *Energy, 119,* 961-970. doi: http://dx.doi.org/10.1016/j.energy.2016.11.045

Ziegler, J. G., & Nichols, N. B. (1993). Optimum settings for automatic controllers. *Journal of Dynamic Systems, Measurement, and Control, 115*(2B), 220-222. doi: http://dx.doi.org/10.1115/1.2899060